# Rectification and Magnetism in Single Molecule Junctions


Memoria presentada por

**SIYA SHERIF**

para optar al grado de Doctor en Ciencias Físicas por la

Universidad Autónoma de Madrid




Dirigida por

**PROF. NICOLÁS AGRAÏT DE LA PUENTE**

Departamento de Física de la Materia Condensada


October 2015

# Rectification and Magnetism in Single Molecule Junctions

A Thesis submitted in partial fulfilment
of the requirements for the degree of
Doctor of Philosophy in Physics
by

**SIYA SHERIF**

FACULTAD DE
CIENCIAS
UNIVERSIDAD AUTÓNOMA DE MADRID

Thesis supervisor
**PROF. NICOLÁS AGRAÏT DE LA PUENTE**

Departamento de Física de la Materia Condensada
Universidad Autónoma de Madrid
October 2015

**Thesis committee**

Prof. José Gabriel Rodrigo Rodríguez (Universidad Autónoma de Madrid)
Prof. Juan Carlos Cuevas Rodríguez (Universidad Autónoma de Madrid)
Prof. Carlos Untiedt Lecuona (Universidad de Alicante)
Prof. Ismael Díez Pérez (Universitat de Barcelona)
Dr. Andres Castellanos-Gomez (IMDEA-Nanociencia)

This work has been supported by the European Union (FP7) through the program ELFOS.

There are the rushing waves, mountains of molecules
Each stupidly minding its own business
Trillions apart, yet forming white surf in unison

Richard P. Feynman

# *Acknowledgements*

The work presented in the thesis is carried out with the help and collaboration of many people. It is a pleasure to thank who made this thesis possible.

First and foremost, I would like to thank my thesis supervisor, Prof. Nicolas Agrait, for giving me the opportunity to work on this project. I would like to express my gratitude to him for his wise advice, patient guidance and support throughout my stay in the lab. I am greatly indebted to him for his mentorship, and I have learned a lot of things from him.

I thank Dr Teresa Gonzalez and Dr Edmund Leary for guiding me all through. They helped me immensely in understanding the technical aspects of the single molecule experiments, sample preparation and data analysis. I thank Prof. Sebastian Viera for his help regarding low-temperature experiments, especially in solving the problems with the leaks in the cryostat. I also thank Prof. José Gabriel Rodrigo, for his assistance in upgrading low-temperature STM and necessary electronics.

I would like to thank Prof. Eugenio Coronado for introducing to polyoxometalate chemistry and providing the molecules for the measurements. My sincere thanks to Prof. Carlos Cuevas for his guidance and help in theoretical work. Also, I thank Prof Sergey Kubatkin and Dr. Andrey Danilov for their assistance in developing sample handling procedure for low-temperature experiments. I also thank Prof Dr. Roberto Otero and Luigi Terreciano for XPS measurements.

I wish to express my sincere thanks to Andrés Buendía for his help in setting up experimental setup and his assistance in troubleshooting while running experiments. I thank the technicians in Condensed Matter Department Santiago Marquez, Rosa Díez, Juan Benayas and Jesus for all their technical support in experimental work. I also extend my thanks to the SEGAINVEX team for the uninterrupted supply of Liquid Helium during my experiments.

Thanks to Prof. Hermann Prof. Miguel Ángel Ramos and Prof. Gabino Rubio-Bollinger, for their support. I thank Dr V Ganesan and Prof R Srinivasan for their encouragement.

I take this opportunity to express gratitude to my lab members: Dr. Charalambos for great companionship in the lab (cafes, overnight experiments, conferences, ) and outside (barbecues, Indian trip, Fontana de Oro, Einstein bar). I thank Aday and Jorge for their help and support during my stay in Lab. I thank Laura for her help in sample preparation and, also for the Spanish translation. I also express my gratitude towards Dr Carlos and Dr Andres for helping and guiding me during my thesis. I am grateful to all my colleagues at low-temperature lab - Ana, Tomas, Guillermo, Adrian, Merzak, Anton, Edwin, Auguso, Juanpe, Anton, Isabel, Manuel, Prasanna, and Jan, for providing wonderful working atmosphere in the lab and helping me at various juncture of my experiments. I also thank Shinto for his support and coffee break discussions.

Special mentions for *K-gang* from the University of Mysore- Rohin, Azhar, Thomas and Kaushik for their assistance, support and encouragement to overcome difficult times and stay focused. I also thank Prashanth, Radahakrisha, Deepa and Akshatha. I am also grateful to *QC group* - Nicole, Niel, Mike, Isabel (and Chara) for the great moments in Madrid. Vishal and Hanna deserves a special thanks for their help and support, especially in the last few months.

I thank European Union for providing financial support through FP7 ELFOS Project. I thank IMDEA-Nanoscience and Universidad Autonoma de Madrid for supporting and providing me with sufficient infrastructure to carry out this project work. I would also like to show our gratitude to Elsa Sánchez & Luisa Carpallo ( Department of Condensed Matter Physics), María Jesús & Isabel Rodríguez (IMDEA Nanoscience) and Maki, Elsa & Isabel Sánchez (Centro de Acogida Internacional) for their help in official paperwork.

My Parents deserve a special mention for their support throughout. Lastly, I offer my regards to all of those who supported me in any respect during the completion of the thesis.

# *Abstract*

The electronics industry has been consistently in demand to develop miniaturized devices by scaling down the size of the electronic components. Gordon E. Moore observed this trend in size reduction and proposed his famous Moore's Law [1]. The present top-bottom approaches used in the production line are reaching the theoretical limit. One way to overcome this limit is to use functionalized molecules that can perform as electronic components [2]. Aviram and Ratner first proposed this concept in 1974 [3]. They suggested that a molecule could act as a rectifier, a primary electronic component that allows the flow of current only in one direction. Ever since researchers have been trying to develop molecule based devices that could replace various electronic components. Molecules are small and must be considered as quantum mechanical systems, which opens the possibility of devices based on quantum properties such as quantum computers, quantum interference devices, etc. To develop such devices, it is necessary to understand the properties of the molecules at the individual level. Measuring electronic transport across the molecule is one of the methods to probe these quantum properties. This is a challenging task that requires contacting the molecule with external electrodes. A scanning tunnelling microscopy (STM) is an ideal tool for studying electronics and magnetic properties of single molecules deposited on surfaces. The main motivation of this thesis is to investigate rectification and magnetism in single molecule STM junctions at both room and cryogenic temperatures.

One of the prerequisites for single molecule experiments using STM is to have a "good" sample, i.e., well- separated individual molecules spread on a flat conducting substrate. The first part of the thesis deals with a technique for depositing the molecules on a suitable substrate. We have successfully deposited $K_{12}(DyP_5W_{30}O_{110}).nH_2O$ molecules on an Au(111) substrate. This was not an easy task due to the size of the molecule. In the second part we investigate the rectification observed in the molecule. The rectification ratio attained for this molecule is quite high, more than ten times larger than previously reported

results in molecular junctions. We could also explain unambitiously that the rectification in this molecular system is arising from the asymmetric coupling of the electrodes and molecule. The third part of the thesis deals with the magnetism in the same molecule. This molecule is single-ion molecular magnet that exhibit magnetic properties at low temperature in bulk samples. We addressed the following question: Does the molecule preserve its magnetic behaviour when deposited on a metallic substrate? Inelastic spin flip tunnelling spectroscopy probing the magnetism in the individual molecules showed that the molecules did preserve their magnetic properties on the surface. The last part of the thesis, focuses on fabricating a superconducting Graphene substrate that could eventually be used in single-molecule experiments. We show that Graphene on lead becomes superconducting by proximity effect.

# *Resumen*

La industria de la electrónica ha demandado consistentemente desarrollar dispositivos miniaturizados mediante la reducción del tamaño de los componentes electrónicos. Gordon E. Moore observó esta tendencia en la reducción del tamaño y propuso su famosa Ley de Moore [1]. Las aproximaciones 'top-bottom' actuales (de arriba-abajo o de lo macro a lo nano) utilizadas en la línea de producción están alcalzando el límite teórico. Una forma de superar este límite consiste en utilizar moléculas funcionalizadas que puedan actuar como componentes electrónicos [2]. Aviram y Ratner propusieron este concepto por primera vez en 1974 [3]. Sugirieron que una molécula puede actuar como un rectificador, un componente electrónico primario que permite el flujo de corriente sólo en una dirección. Se ha intentado desde entonces desarrollar dispositivos basados en moléculas que pudieran reemplazar diversos componentes electrónicos. Las moléculas son pequeñas y deben considerarse como sistemas mecanocuánticos, lo que ofrece la posibilidad de desarrollar dispositivos basados en propiedades cuánticas como ordenadores cuánticos, dispositivos de interferencia cuántica, etc. Para desarrollar dichos dispositivos, es necesario entender las propiedades de las moléculas a nivel individual. La medida de transporte electrónico a través de una molécula es uno de los métodos para explorar estas propiedades cuénticas. Éste es un reto importante que requiere contactar la molécula con electrodos externos. Un microscopio de efecto túnel (STM) es una herramienta ideal para estudiar las propiedades electrónicas y magnéticas de moléculas individuales depositadas sobre superficies. La principal motivación de esta tesis es investigar rectificación y magnetismo en uniones moleculares individuales formadas con un STM a temperaturas ambiente y criogénicas.

Uno de los requisitos para realizar experimentos en una única molécula utilizando un STM es tener una "buena" muestra, lo que significa tener moléculas bien separadas unas de otras distribuidas sobre un sustrato conductor plano. La primera parte de la tesis trata sobre la técnica para la deposición de moléculas en un sustrato adecuado. Hemos depositado satisfactoriamente

molécuals de $K_{12}(DyP_5W_{30}O_{110}).nH_2O$ sobre un sustrato de Au(111), aunque no fue una tarea sencilla debido al tamaño de la molécula. En la segunda parte investigamos la rectificación observada en dicha molécula. La ratio de rectification que alcanza es bastante elevada, más de diez veces mayor que los resultados de uniones moleculares publicados previamente. También hemos podido explicar inequívocamente que la rectificación en este sistema molecular surge del acoplamiento asimétrico de los electrodos y la molécula. La tercera parte de la tesis trata sobre el magnetismo de esta misma molécula, la cual es un imán molecular con un único ión que presenta propiedades magnéticas a baja temperatura en muestras macroscópicas. Por este motivo nos planteamos la siguiente pregunta: ¿ conserva la molécula su comportamiento magnético cuando se deposita sobre un sustrato metálico? Espectroscopía ineslástica de espín (inelastic spin tunneling spectroscopy) para explorar el magnetismo de moléculas individuales mostró que las moléculas sí conservaban sus propiedades magnéticas en la superficie. La última parte de la tesis se centra en la fabricación de un sustrato de grafeno superconductor que podría utilizarse en experimentos de moléculas individuales. Mostramos que el grafeno sobre plomo se vuelve superconductor por efecto de proximidad.

# Contents

# List of Figures

# List of Tables

*Dedicated to my Teachers*

# Outline

In Chapter 1, I will discuss the experimental techniques used in this thesis. A brief introduction to Scanning Tunnelling Microscopy and spectroscopy is given in this chapter. Also, experimental work involved in the construction of Low-temperature STM and working off $^3$He Cryostat is also mentioned in this chapter.

The rest of the thesis is divided into four parts. The first Part I, contains Chapter 2. In the first section of this chapter, I will give a brief introduction to the various deposition methods used for depositing molecules on the surface for STM studies. The second section deals deposition methods used for depositing the molecule $[Dy(H_2O)P_5W_{30}O_{110}]^{12-}$, DyW30 and characterization of the molecule deposited on the surface using STM and XPS. This chapter also deals with a procedure optimized for obtaining a clean sample for low-temperature measurements.

The Part II is divided into two Chapters, Chapter 3 and Chapter 4. The Chapter 3 is a historical review of the rectification process in electronics and evolution molecular rectifiers. This chapter also deals with the theoretical model used to describe the molecular device. The Chapter 4 describes the experimental measurements on DyW30 and rectification observed. We also explain the theoretical model evoked to analyse the rectification in the molecule.The results show that the rectification arise from the asymmetric coupling the electrodes linking the molecule. The model was further verified by conducting

measurements on $C_{60}$. The comparison between rectification ratio observed in these two molecules are also given in this chapter.

The Part III deals with the magnetism in Single Molecule Magnet (SMM). This part has two chapters. The Chapter 5 gives a review on SMM, focusing on single ion single molecule magnets. This chapter also reviews about the experimental used to probe magnetism in SMM electrically. The Chapter 6 describes the electronic transport measurements on DyW30 molecule for the first time. The Spin-flip inelastic tunnelling spectroscopy was to detect the spin-flip transitions in this molecule. Also, Kondo effect was observed on the molecule. The magnetism in this molecule was modelled by using SIMPRE software [10]. The proximity-induced superconductivity in Graphene is described in Part IV. The Chapter 7 is a review about superconductivity, Graphene and experimental methods to measure spatially resolved superconducting proximity effect. The Chapter 8 shows the experimental results showing proximity effect on Graphene.

The general conclusion of this thesis is presented in Part V.

# Chapter 1

# Experimental Techniques

Experimental techniques involved in this thesis are described in this chapter. The first section describes compact STM designed for operating at milliKelvin temperature. The second section of the chapter deals with the cryogenic and low temperature techniques involved.

## 1.1 Scanning Tunnelling Microscope

Scanning Tunnelling microscope (STM) was invented by G. Binning, H. Rohrer, Ch. Gerber and E. Weibel at IBM Research Laboratory in Rschlikon, Switzerland [11]. In 1981 G.Binning *et. al.* demonstrated tunnelling of electrons thorough a controllable vacuum gap [12]. Later they combined this controllable vacuum tunnelling with scanning capabilities of piezoelectric materials to develop a surface probing device called STM [13]. Invention of STM opened a novel method to probe the surface of materials with unparalleled precision. In 1986 G.Binning and H.Rohrer were awarded Nobel prize for this invention.

### 1.1.1 Tunnel Effect

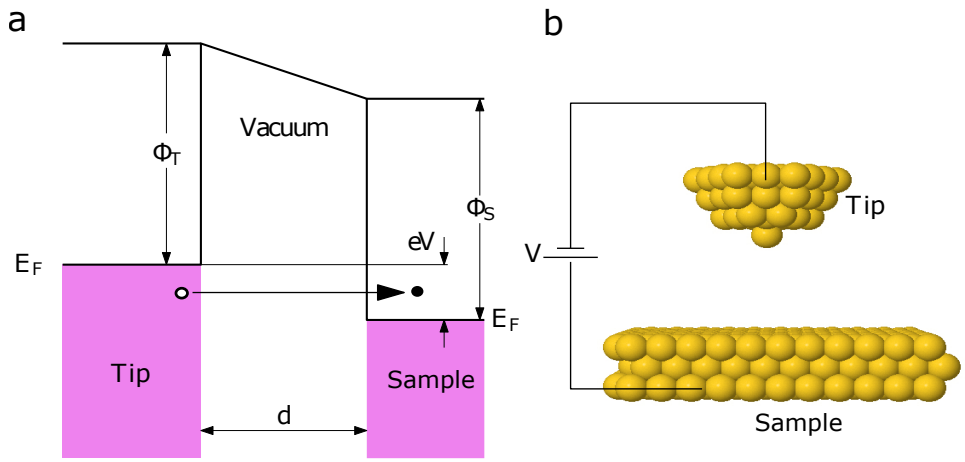


FIGURE 1.1: (a)Tunnelling between the tip and sample across a vacuum barrier of width, d. (b) Schematic of STM

The working principle of STM is based on quantum tunnelling of electrons between two conducting electrodes (tip and sample) separated by an insulating barrier. This can be visualized in as one dimensional tunnel barrier as shown in Figure 1.1 a. A voltage, usually termed as Bias Voltage - $V_b$, is applied to one of the electrodes (usually sample). When $V_b = 0$, Fermi level of the tip and sample get aliened in the same energy level. $\Phi_S$ and $\Phi_T$ are the work function of sample and tip. When a voltage, $V_b = \mathrm{V}$ applied between the tip and sample shifts the $(E_f)$ by eV. This results in the formation of a trapezoidal barrier. Classically, an electron with energy less than the vacuum tunnel barrier cannot cross this junction. Quantum mechanically, the electron can tunnel through this if the barrier is thin. The tunnelling Current,$I_t$, between the electrodes depends exponentially on the distance, $d$ between the electrodes. Quantum Mechanical treatment of a one dimensional tunnel barrier system gives an expression for Tunnelling Current

$$I_t(d) \propto e^{-2kd}, \quad where \quad k = \frac{\sqrt{m_0(\Phi_S + \Phi_T - eV)}}{\hbar} \tag{1.1}$$

where $m_0$ is the rest mass of electron and $\hbar$ is reduced Planck constant. Work functions of typically used materials are around $4 - 5$eV [14]. Substituting this value in Equation 1.1 gives a $k$ value of 10 nm$^{-1}$. This corresponds to a variation of one order of magnitude in tunnelling current for every angstrom increase in the electrode spacing. This exponential dependence of the tip-sample distance provides STM high vertical resolution.

### 1.1.2 Imaging using STM

In imaging mode, one of the electrodes (usually the tip) is brought closer to the sample until a measurable funnelling current appears. In the tunnelling regime, the tip is moved laterally in raster scan pattern using piezo transducers. Changes in the current with respect to lateral displacements is recorded and combined together to make a 3 D topographic image of surface. Scheme of working of STM is shown in Figure 1.2.

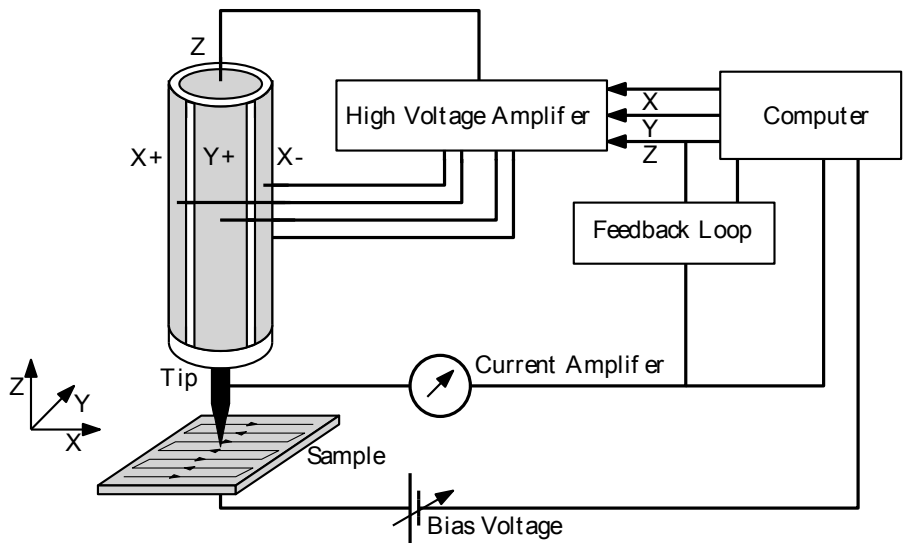


FIGURE 1.2: Scheme showing working of a STM.

There are two imaging modes for STM. In *Constant Current mode*, the tunnelling current ($I_t$) between the tip and sample is kept constant by adjusting the tip - sample distance ($Z$) with the help of a feedback loop. The recorded displacement of $Z$ is combined with the $X, Y$ displacement of the tip to generate a topography of scanned area. Cartoon showing constant current imaging is shown in Figure 1.3a. In *Constant Height mode*, Tip - Sample distance ($Z$) is kept constant. The changes in the current are recorded as function of $X, Y$ movements of tip. The Constant Height Mode helps in faster acquisition when compared with the Constant Current Mode, since the imaging speed in Constant Current Mode is limited by the response time of feedback loop. Constant Height is suitable only for scanning flat area with small corrugation. Since there is no feedback, scanning with constant height near step edges might result in tip crash. This is shown in cartoon Figure 1.3b. For this reason Constant Current mode is usually employed for scanning [15]. Tunnelling current strongly depends on the Density of States (DoS) of the sample. Local variations in density of states result in the variation of tunnelling current. Due to this reason the height measured by STM need not be the actual height.

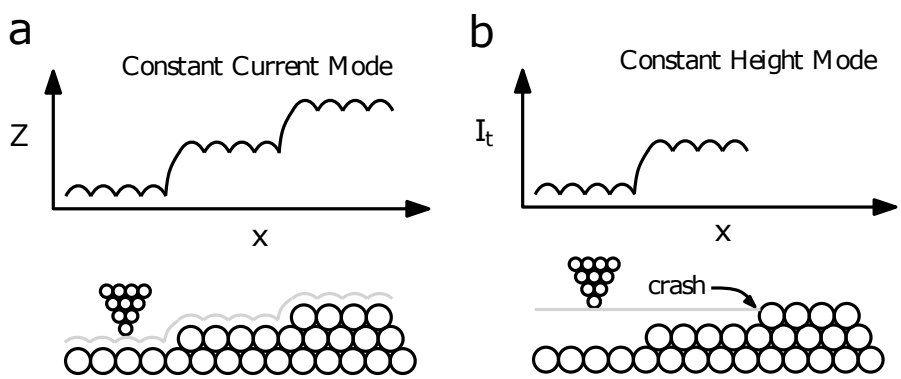


FIGURE 1.3: (a) Constant Current Mode, Tunnelling Current is kept constant using feed back control. Gray line shows Tip displacement. Inset shows Z displacement recorded vs x displacement. (b) Constant Height Mode, Tip - sample distance is kept constant (grey line). Tip crash at step edge is also shown. Inset show change in tunnelling current vs x displacement

### 1.1.3 Scanning Tunneling Spectroscopy

STM is not only an imaging probe but it can also give information of the Local Density of States (LDOS). Ability of the STM to do Spectroscopy of of a material with high lateral resolution makes it an inevitable tool to investigate the electronic properties of materials. In Scanning Tunnelling Spectroscopy (STS), the tunnelling current $I_t(V)$ as function of varying the bias voltage is measured while keeping the tip - sample distance constant. Theory for tunnelling current across a planar junction was formulated by Bardeen [16] and later it was modified by Tersoff and Hamann for STM [17, 18]. In Tersoff-Hamann formalism, net current flowing in the junction is the difference between the current passing from tip to sample and sample to tip. Expression for the net current is given by

$$I = \frac{4\pi e}{\hbar} \int_{-\infty}^{+\infty} \mid M \mid^2 \rho_s(E_F - eV + \varepsilon)\rho_t(E_F + \varepsilon)[f(\varepsilon) - f(\varepsilon + eV)]d\varepsilon \quad (1.2)$$

where $\mid M \mid$ is matrix element for tunnelling, $\rho_s$ and $\rho_t$ are the density of states of the sample and the tip respectively. $f(E)$ is the Fermi distribution given by

$$f(E) = \frac{1}{1 + e^{E/k_B T}} \quad (1.3)$$

The tunnelling matrix element $M$ is given by the formula

$$M = \frac{\hbar^2}{2m} \int_{\Sigma} (\Psi_s^* \nabla \Psi_t - \Psi_t^* \nabla \Psi_s)\, dS \quad (1.4)$$

where $\Psi_s$, $\Psi_t$ are respectively the wave functions of the sample and tip electrons. Surface integral $\Sigma$ takes into account all the tunnelling region. At zero temperature, Fermi function is a step function. Hence derivative of this term results in a delta function. For small bias voltages Equation 1.2 reduces to

$$I(V) \propto \int_0^{eV} \rho_s(E_F - eV + \varepsilon)\rho_t(E_F + \varepsilon)\varepsilon \tag{1.5}$$

Assuming that the density of states of the tip is constant. Then differential conductance, G determines the density of states and is given by

$$G(V) = \frac{dI(V)}{dV} \propto \rho_s(E_F - eV) \tag{1.6}$$

Two methods are usually employed to obtain STS. The *Numerical method*, in which dI/dV is obtained by taking numerical derivative of the I-V curve. The *Lock-in method*, uses lock-in amplifier to obtain dI/dV spectra. In this method, a small ac-voltage modulation is added to the bias voltage. Then the current is expressed by

$$I(V) = I(V_b + V_{ac}cos(\omega t)) \tag{1.7}$$

where $V_{ac}$ is the amplitude of the modulation and $\omega$ is the frequency of modulation. For a small modulation, $V_{ac}$, expression for the tunnelling current in Equation 1.7 can be expressed into a Taylor series.

$$I = I(V_b) + \left(\frac{dI}{dV}\right)_{V_b} V_{ac}cos(\omega t)) + O(V_{ac}^2) \tag{1.8}$$

This expression clearly shows that the dI/dV can be obtained by measuring the component of the current at the frequency $\omega$..

### 1.1.4 Inelastic Electron Tunneling Spectroscopy

In the previous section, discussions were about the elastic process. If there is any resonant energy level in the tunnel barrier region, inelastic processes can occur. Tunnelling Spectroscopy can be used to investigate inelastic process

occurring in the tunnel barrier junction. Consider an energy level lying in the a tunnel barrier region as indicated in Figure 1.4.

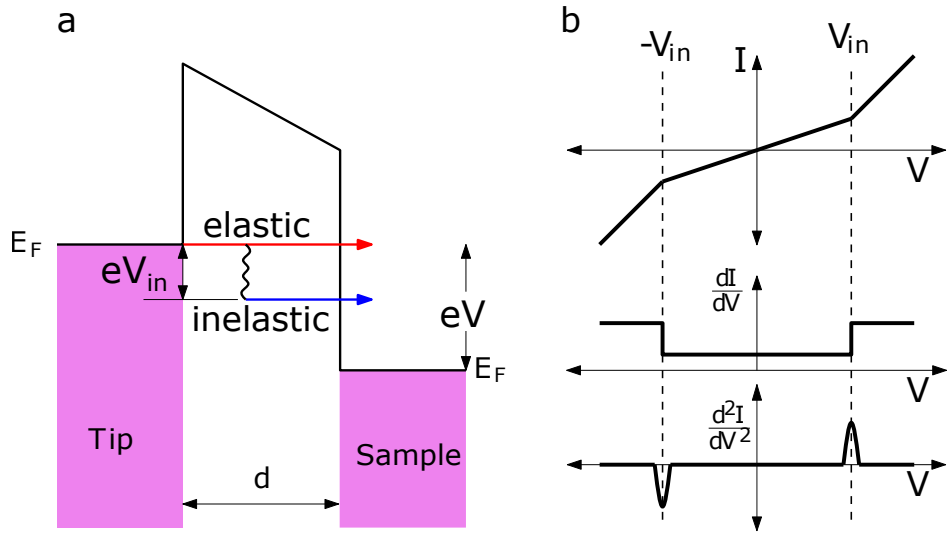


FIGURE 1.4: (a) Schematic of IETS, electrons with energy $> V_{in}$ can lose energy by inelastic process (b) $I-V$ curves of an inelastic tunnelling process, opening of new inelastic channel results in change in the current for voltages above $V_{in}$ and corresponding changes in the $dI/dV$and $d^2I/dV^2$

At voltages ($V < V_{in}$) tunnelling is elastic. When the energy of the incoming electron is greater than $V_{in}$, the electrons can access this resonant level and some electrons interacts inelastically. This inelastic interaction opens up a new channel for the electron and results in a change in current. This is observed as step in the $dI/dV$ and "peaks and dips" in $d^2I/dV^2$. This process was first observed by Jaklevic and Lambe in metal oxide tunnel junctions [19]. Inelastic Electron Tunnelling Spectroscopy (IETS) techniques were combined with STM to study the vibrational modes in atomic chains and molecules in metal - molecule - metal junctions [20, 21]. The intrinsic width of the spectral peak ($W_{int}$) (see Figure 1.4.b) obtained by IETS is broadened by two factors, (a) thermal broadening due to breadth of Fermi level and (b) broadening due ot the modulation applied to measure [22]. The measured width, $W_{measured}$ -full width at half maxima, of the peak can be expressed as

$$W_{measured} = \sqrt{\underbrace{(\Delta E)^2}_{W_{intrinsic}} + \underbrace{(1.7V_{rms})^2}_{W_{modulation}} + \underbrace{\left(5.4\frac{K_B T}{e}\right)^2}_{W_{Thermal}}} \tag{1.9}$$

where $\Delta E$ is intrinsic width of the peak. $W_{modulation}$ is the broadening due to the modulation applied to bias voltage. $V_{rms}$, is the root mean square value of the modulation voltage. $W_{Thermal}$ is the thermal broadening appearing in the peak.

## 1.2 Low Temperature STM

Most of the work presented in this thesis has been carried out using the custom built STM designed for operating at milli-Kelvin temperatures. The design of the Low Temperature STM (LT-STM) is based on the design by S.H. Pan [23]. Body of the STM is made out titanium. This STM has the 3 parts, slider for holding piezo-tube and tip, slider for the sample holder, STM body holding piezo stacks for horizontal and vertical movements. The sliders are triangular prisms made out of titanium. This is clamped to four piezo stacks using a spring. The piezo stack for the vertical movement were constructed by Carlos Arroyo as a part of his doctoral studies [24].

### 1.2.1 Piezotube

Piezoelectric effect is the property of certain materials to generate electric charge in response to mechanical stress applied on it. This effect was first observed by Jacques Curie and Pierre Curie[25]. Conversely, these materials show inverse piezo electric effect, *i.e.* change in the mechanical stress with respect to applied electric voltage. High voltages applied correspond only to a tiny mechanical deformation of material. This enables Piezo Electric Transducers (PZT) in precise movements.

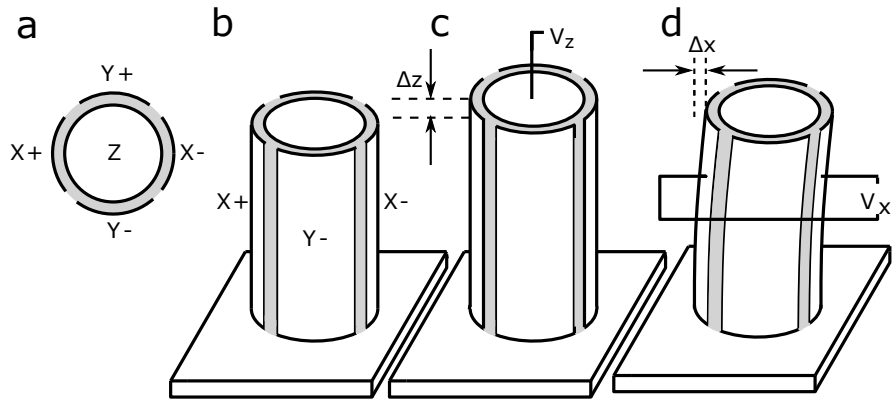


FIGURE 1.5: (a) Shows the cross section of a piezo tube.(b) schematic of piezo tube attached to the base. (c) Shows the vertical displacement, ΔZ of piezo tube when a voltage is applied in inner electrode(d) Shows the lateral displacement, Δ X of piezo tube when a voltage is applied across the opposite electrodes (in this case X+ and X-).

The piezo tube is a radially polarized piezo actuator. Figure 1.5 a shows schematics of a piezo tube. One end of the tube is glued to the base. As indicated in the Figure 1.5.a Z electrode is connected in the inner ring of the tube. Voltage applied in the inner part results in expansion and compression of the tube. Schematic of movement is shown in Figure 1.5 c. The outer part the tube is connected to four electrodes (±X and ±Y). Voltage applied across opposite electrodes causes lateral deformation in the piezotube. Schematics of deformation of the tube in x direction is shown in Figure 1.5 STM tip is placed on the free end of the tube. Fine movement of the tip is achieved by movement of tube in x,y,z direction.

### 1.2.2 Coarse positioning using piezostacks

Precise positioning of the STM tip close to the surface (tunnelling regime) is essential for the operation of the STM, especially at low temperature. The piezo-tube described in the previous section is attached to a slider, a V shaped titanium prism. The slider is placed on piezostacks in the V Shaped groove on the STM body. An adjustable copper spring holds the slider firmly to the

piezostacks. A scheme of the STM is shown in Figure 1.6. A Vertically moving Slider hold the piezo tube and STM tip. Horizontally moving slider hold the sample. The use of horizontally moving slider allows long range movement of sample in one direction.

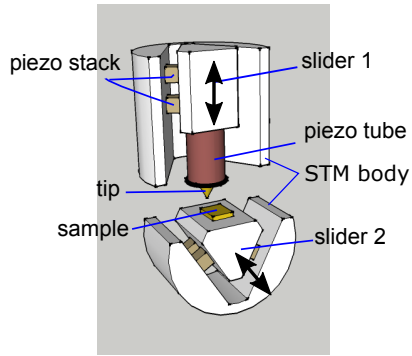


FIGURE 1.6: Simplified scheme of STM. The arrows indicates the direction of the Slider movement. This moving slider follows the design of Prof. J.G. Rodrigo

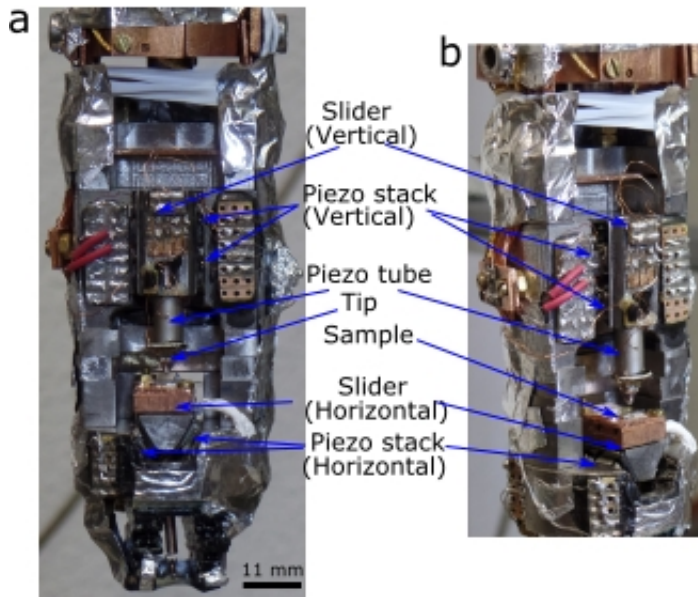


FIGURE 1.7: Low temperature STM used for experiments (a) front view (b) side view

Shear piezos are PZT actuators, that shows a shear deformation when voltage is applied across it. Combination of four shear piezo are used to achieve coarse motion of slider. Coarse movements can be done in two modes, *inertial mode* and *delayed ramp mode*.

*Inertial mode* operation is done by utilizing slip stick motion of the four shear piezo stacks. A scheme of operation is showed in Figure 1.8. A saw tooth signal is applied across all the four piezo stacks simultaneously. As indicated in Figure 1.8 b and c, in the initial step, stacks moves the slider in the direction of piezo deformation. When the Voltage drops suddenly in saw tooth step, piezo stack makes a slip. Direction of the movement can controlled by changing the polarity of the voltage signal.

*Delayed ramp mode*: In this method, resistors added in series with piezo stacks. The value of the resistor is selected in such a way that there a is delay in voltage signal arriving at each piezo stack. When one piezo deforms, the other three piezos holds the slider. Once all the four piezo stack are deformed, they all are moved simultaneously in opposite direction to move the slider. Scheme of operation is shown in Figure 1.9

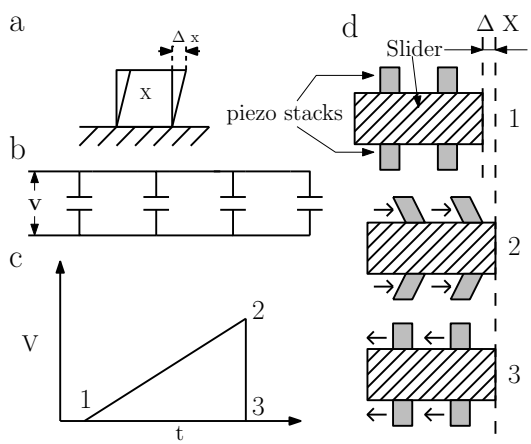


FIGURE 1.8: (a) Scheme of working of a shear piezo (b) Equivalent circuit diagram of a piezo electric walker in inertial operation. Piezos are represented by capacitors. (c) Voltage signal applied across the piezo Stack (d) Slip - Stick motion of the slider in response to the applied signal. piezo stacks are indicated by grey color and slider by black stripes.

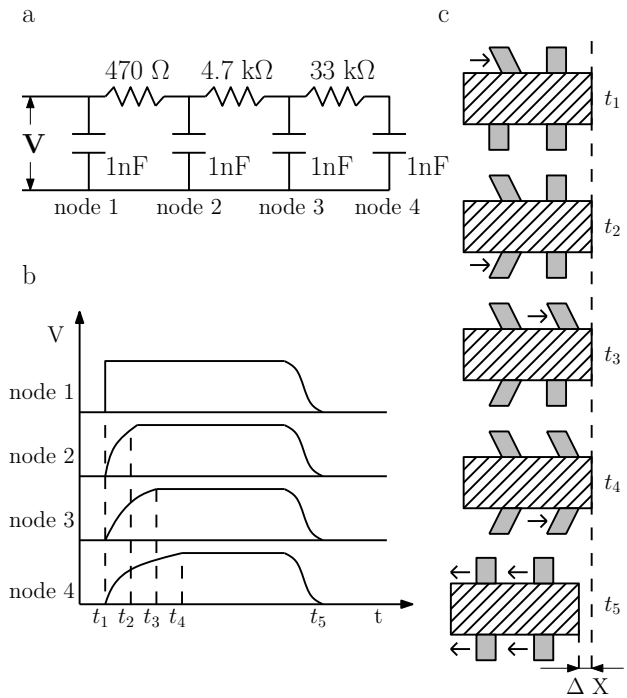


FIGURE 1.9: Scheme of delayed ramp mode operation of a slider. (a) shows equivalent circuits of piezo walker in delayed ramp mode. (b) sequence of voltage applied to each piezo stack and (c) corresponding motion of piezos and slider.

### 1.2.3 STM Control Unit

The electronic components fo the STM such as high voltage amplifiers for piezo electronic, current to voltage converter, etc. were designed and built in the workshop of the Universidad Autónoma de Madrid (SEGAINVEX). STM was controlled by a computer through a National instrument multi-functional card, NI PCI-7833R. The software for the STM control was also developed in the Laboratorio de Bajas Temperaturas, Universidad Autónoma de Madrid (LBT-UAM).

## 1.3 Low temperature Measurements

Low temperature measurements were carried out using Heliox $2^{AST\ VL}$ - $^3$He cryostat supplied by Oxford Instruments.

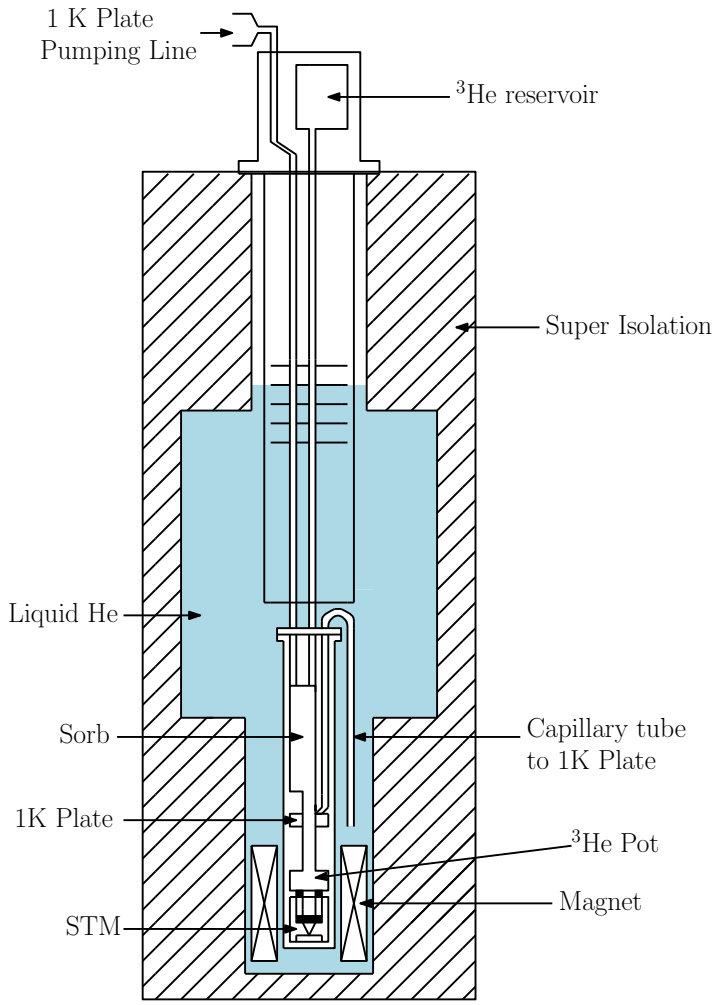


FIGURE 1.10: Schematic of the $^3$He cryostat and dewar

Figure 1.10 illustrates the cryostat and dewar. Unlike most Helium dewars, this dewar does not have an outer liquid nitrogen jacket because the boiling of the liquid-nitrogen causes mechanical vibrations which critically affect STM measurements. Hence, the nitrogen jacket free dewar helps in reducing the

noise level of measurements. The inner part of the dewar is thermally shielded from the outer world by an outer vacuum chamber (OVC). The outer vacuum chamber also contain super-insulting materials which further reduces the heat losses to surroundings. The OVC was pumped using a diffusion pump for 3-4 days to achieve a good vacuum inside it. This OVC vacuum pumping process is repeated annually to ensure better thermal isolation. Inner Helium reservoir also holds a 9 Tesla superconducting magnet coil. The reservoir has a capacity of 56 L and hold time is approximately 50 hours (when no magnet field applied).

### 1.3.1 Working of $^3$He Cryostat

The main parts of the insert are 1) 1-K plate, 2) the sorption pump and 3) the helium-3 reservoir. The 1-K plate is connected to the Helium-4 reservoir through a capillary tube. The flow of Helium-4 through the capillary is controlled by a needle valve that is operated externally. When the valve is open Helium-4 from reservoir flows into the 1K plate. The exit tube of the 1K-plate connected to an external pumping line. The Helium-4 entering 1K-plate can be pumped through this external line. This pumping reduces the pressure inside the 1-K plate and causes the boiling of Helium-4 entering 1 K Plate. The heat of vaporization in this process cools 1K plate. The flow of the Helium-4 should be optimized to achieve proper cooling of 1 K plate. Typically the lowest temperature achieved at the 1K-plate is around 1.5 K. The sorption pump absorbs the He gas when cooled below 30 K. The sorption pump is cooled by a heat exchanger connected to pumping line of 1K pot. Temperature of the sorb can be controlled by a heater fitted on it. After lowering the temperature of the 1 K pot, the heater in the sorb is turned ON. Temperature of the sorb is set above 30 K. At this temperature, Helium-3 begins to desorb from the sorption pump. Helium-3 gas flowing down will be condensed at the 1 K and liquid Helium-3 is collected at the Helium-3 pot (see Figure 1.11). The sorb is maintained at this temperature until all the Helium-3 condenses on the pot. Once all the Helium-3 is condensed, the heater in the sorb is turned OFF. As

the temperature in the sorb drops it begins to adsorb $^3$He. This reduces the vapor pressure in Helium-3 pot and heat of vaporization of $^3$He cools the pot. A temperature as low as 0.350 K can be achieved at pot by this process.

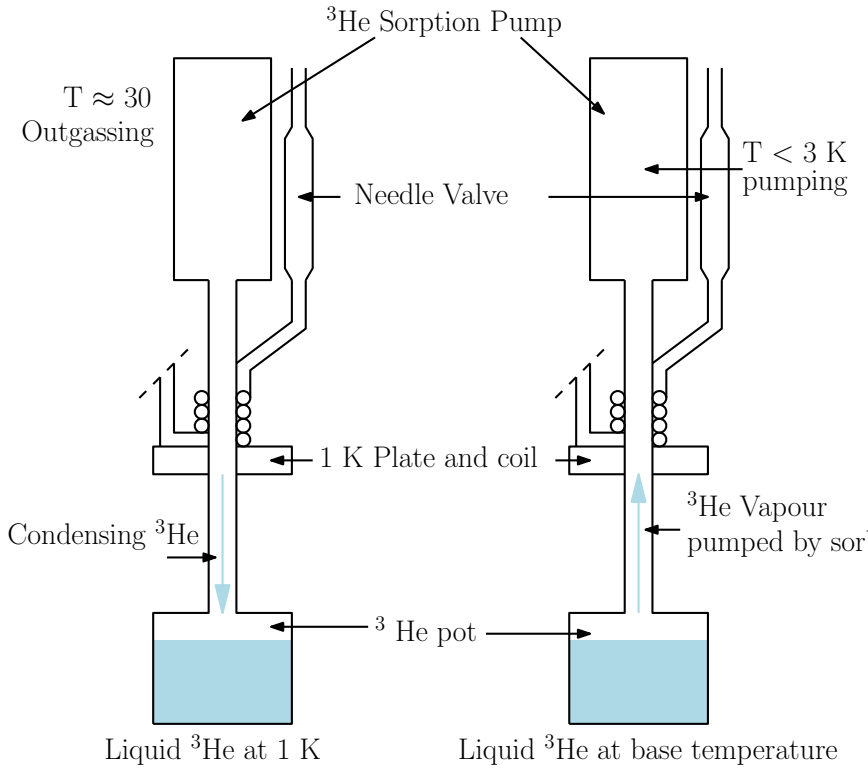


FIGURE 1.11: Working of $^3$He cryostat

### 1.3.2 Mechanical and Electrical noise reduction

Vibration isolation is an essential part of an STM measurement. A change of 0.1 nm in vertical displacement results in one order of magnitude change in the tunnelling current (see Eqn 1.1 ). For this reason STM should be isolated from all sorts of mechanical noise. In-order to isolate the system from mechanical vibrations of the building, Dewar was suspended using elastic ropes. Initially, four independent cables were used to suspend the dewar. Even though this hanging reduced the mechanical noise, it was difficult to work with this system.

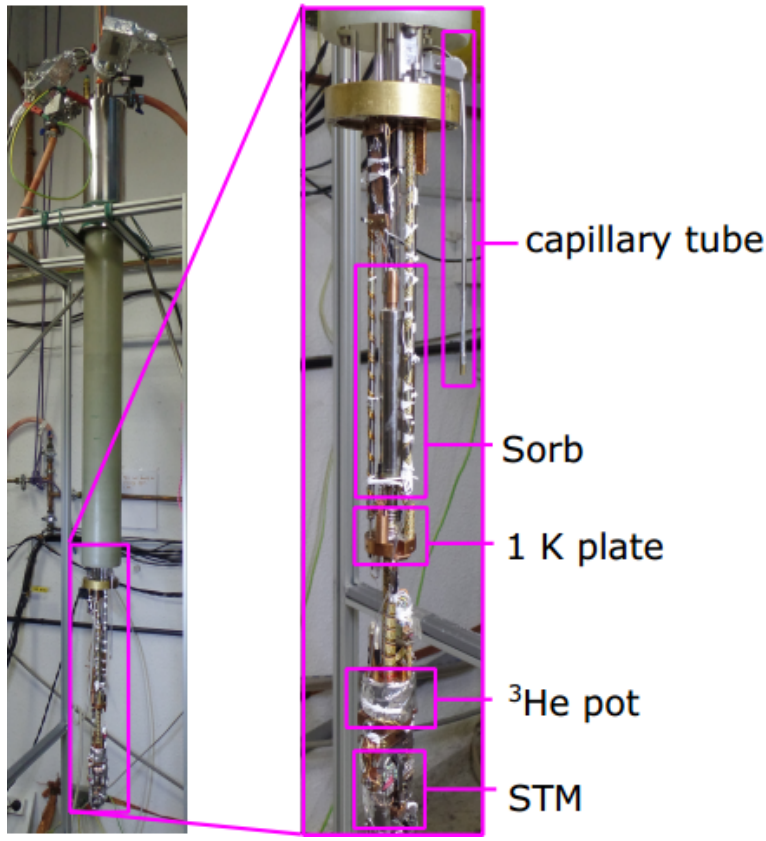


FIGURE 1.12: Picture of Insert and $^3$He system

From time to time the dewar has to be lowered to ground level to refill the Helium in the reservoir. Also, the weight was not perfectly balanced between the four cables. To avoid such disadvantages, we replaced it with rope and pulley system. In the figure 1.13, one can notice that the ropes attached to the top part of the dewar. Single elastic rope interconnected through a set of eight pulleys. Four of these pulleys are attached to the pillars of the lab and four to the dewar. The dewar is hanged with the helped of these pulleys during the measurement. In this case, the weight of the system is equally distributed among the ropes. Also, this arrangement assists in the smooth movement of the dewar during the helium refill.

Another source of the mechanical noise is from the Helium recovery tube lines connected to the dewar and $^3$He-insert. We used rubber based tube for connecting pumping line and helium recovery line to reduce this noise. All the tubes and cables arriving in the cryostat were anchored rigidly to the Dewar. The Pump used for 1K pot is kept outside building to reduce noise. The STM was rigidly fixed to the $^3$He pot using custom-made copper block.

An additional source of noise is the electrical noise from the various electronic instruments used in the lab. The experimental wiring of the system was carefully done in order to avoid any such noise. All the high voltages cables were passed through RF filters. For current and Bias voltage, we used steel coaxial cables. Shield of the coaxial cables and body of the cryostat were connected to common ground. A separate ground, that is separated from the rest of the ground used in the lab, was used for the experimental set-up. A power line filter was used to avoid the electromagnetic interference between the power supply line and the equipments.

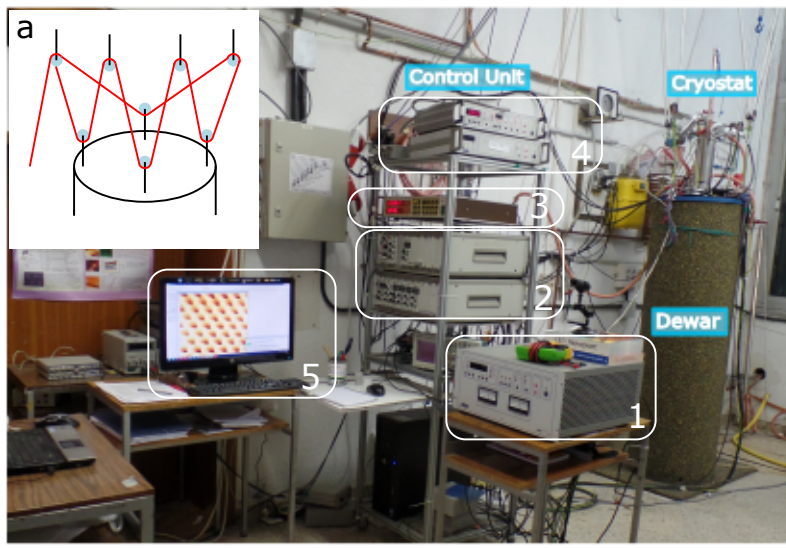


FIGURE 1.13: Photograph of the experimental set-up. Inset shows the schematics of the pulley and rope system to hang the dewar. 1) Controller for Magnet. 2) Electronics for STM (Bias voltage card, I-V converter and high voltage amplifier, 3) Capacitance Bridge, 4) Temperature Controller and Helium level meter 5) Computer)

# Part I

# Deposition of Single Molecules on Au(111)

# Chapter 2

# Spray Deposition of molecules on Gold

Controlled deposition of isolated molecules on atomically flat substrates is an essential step to perform single molecule scanning probe experiments. In this Chapter, we have developed a spray deposition method to deposit individual polyoxometalate (POM) molecules on Au(111). The first part of the chapter deals with the deposition of polyoxometalate single-molecule magnet $[Dy(H_2O)P_5W_{30}O_{110}]^{12-}$. The second part of the chapter deals with a procedure to avoid surface contaminations while cooling samples to low temperature.

## 2.1 Motivation

Molecular Electronics aims to integrate rationally designed molecules in an electronic circuit to develop novel electronic gadgets that utilize quantum properties of these molecules[26, 27]. The advantage of these devices is that the charge transport characteristics of these devices can be controlled while designing the molecule using chemical methods (sometimes referred "synthetic

tailarobility"). The possible functionalities that could be achieved by these molecules are conductors, insulators, switches, Memories, amplifiers, diodes, etc [2]. One of the additional functionality molecular electronics aim to incorporate in these molecular devices is magnetism. One way to achieve this is by the use of Single Molecule Magnets (SMM), which are magnetic molecules exhibiting a slow relaxation of the magnetization at low temperatures [28]. These molecules possess large and anisotropic magnetic moments. Many molecules were reported to show SMM behaviour [29]. One of the primary goals in molecular spintronics is to detect and manipulate the spin of the SMM by applying electrical field. Electrical probing is usually done by measuring the electron transport across a magnetic molecule anchored between conducting electrodes. Single molecule transport experiments are typically carried out in electro-migrated junctions, mechanically controlled break junctions or scanning tunnelling microscope (STM) [30–33]. Apart from transport measurements, STM can image molecules with atomic resolution in real space which makes it an ideal technique to investigate SMMs. To probe the molecules using STM, it has to be deposited in a controlled manner on a suitable conducting substrate.

Polyoxometalates (POMs) are an abundant class of metal oxide molecular clusters. These molecules are used in a lot of applications such as catalysis, materials science, medicine and, more recently, magnetism [34, 35]. One of the POM based SMM is potassium salt of the anion $[Dy(H_2O)P_5W_{30}O_{110}]^{12-}$ (henceforth referred as DyW30), which is a lanthanoid-based POM with a 5-fold symmetry. Heat capacity and dynamic magnetic hysteresis measurements of a powdered sample have shown that this mono-nuclear lanthanoid molecule behaves as an SMM at low-temperature [4]. Since these molecules are non-volatile, non-thermal methods must be used to deposit this molecule. In this chapter a simple ex-situ wet deposition method, using a nebulizer was employed, to deposit these magnetic POMs on a metallic substrate.

## 2.2 Review of deposition methods

The studies of the single molecules deposited on a surface are important for both fundamental science and practical applications. Also reducing the size to nano-scale dimensions leads to the appearance of new phenomenologies different from bulk materials. In these systems, inter-molecular interactions and surface interactions play a significant role in determining the physical and chemical properties. These interactions may completely alter the properties of molecules, especially in the case of SMMs. In this section, I a brief review of various deposition methods used to deposit SMMs on various surfaces is given.

For most of the STM studies, molecular deposition is done in an Ultra High Vacuum (UHV) environment. Usually at UHV conditions, thermal evaporation techniques, in which molecules are evaporated on to the surface, are used to deposit molecules in-order to avoid contamination due to the solvents [36]. However, the thermal deposition method is limited to those molecules that have low vapour pressure [37]. A large species of the SMMs are large coordination compounds, and they decompose upon heating, and hence cannot be deposited by using thermal procedure [32]. To overcome such decomposition Kahle *et al.* developed an in-situ electrospray deposition technique compatible with ultra-high vacuum condition[33]. The scheme of Electrospray ion beam deposition (ES-IBD) of Mn12[1] molecular magnets is shown in figure 2.1. They also utilized a mass spectrometer to isolate the intact molecule from fragmented molecule. They showed that fragile Mn12 SMMs can be successfully deposited on metallic and thin-insulating surfaces, and magnetic properties probed using STM.

[1] $Mn_{12}O_{12}(CH_3COO)_{16}(H_2O)_4$ - a single molecule magnet

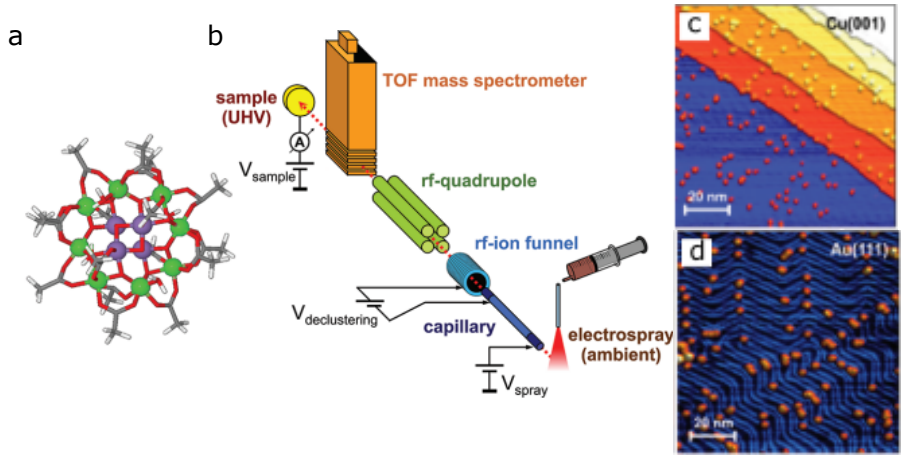


FIGURE 2.1: (a) Structure of the Mn12 SMM (b)Scheme of Electro-spray ion beam deposition technique. (c) and (d) STM topographic images of Mn12 molecules deposited on Cu(001) and Au(111) using electro-spray. Images are from ref [33]

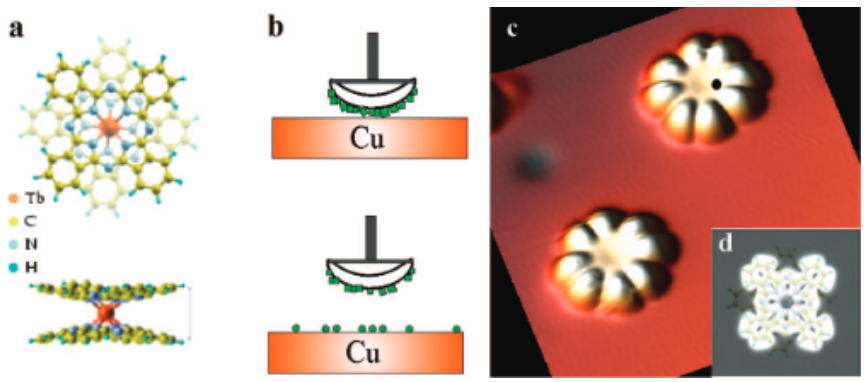


FIGURE 2.2: (a)Structure of the TbPc2 molecule. (b) Scheme of the dry-imprinting technique (c) Constant current topograph of two isolated TbPc2 molecules supported by the Cu(111) surface (d) Simulated STM image of an isolated TbPc2 molecule. Images are from ref [38]

Another deposition method, called dry imprint technique, which is compatible with the ultrahigh vacuum (UHV) conditions was developed by Vitali *et al.* [38]. In this method, fine powder of the molecules is transferred to a fibre glass bundle. Then the fibreglass bundle is brought into soft contact with the surface. This process leads to direct transfer of molecule and clusters on to

the required surface. This method was used to deposit bis (phthalocyanine) terbium (III) on a copper surface (see Figure 2.2). The advantage of this method is that it is free from contamination due to solvent.

However, UHV compatible in-situ deposition techniques are not available in all experimental systems, and in such cases one has to resort to alternative methods to deposit these heavy molecules. Wet chemistry methods are employed to deposit SMM on such situations [39–41]. The simplest wet method to deposit molecules on a surface is drop casting, in which a solution droplet is deposited on the surface. Upon the solvent evaporation, molecules are physisorbed on the surface due to interactions such as hydrogen bonds, van der Waals forces, ionic interactions and hydrophobic interactions [42]. An alternative method for drop casting is dip casting, in which the sample surface is immersed in the solution for particular time and dried afterwards to obtain physisorbed molecules.This method was used to deposit Mn12 [43, 44], bis (phthalocyanine) terbium (III) [39]. The figure 2.3 shows an example of sample prepared by dip casting.

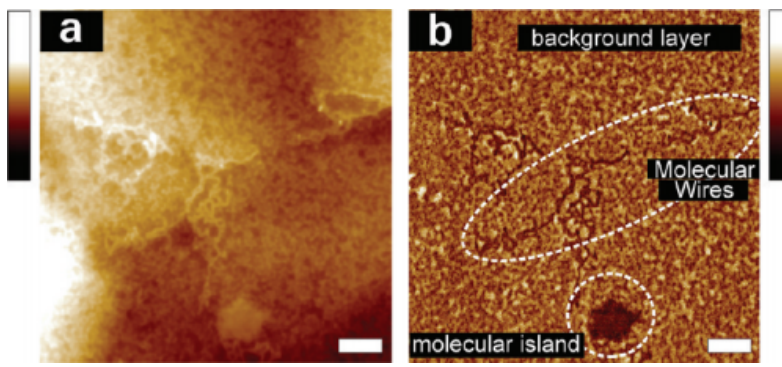


FIGURE 2.3: (a) shows AFM topography ($815 \times 815$ nm$^2$) of a Mn12 sample prepared by dipping substrate in a $10^{-4}$ Molar solution for 1 hour (b) phase shift image of the same area. The phase image clearly shows the surface features such as background layer, molecular wires, and molecular islands. Image from ref [43]

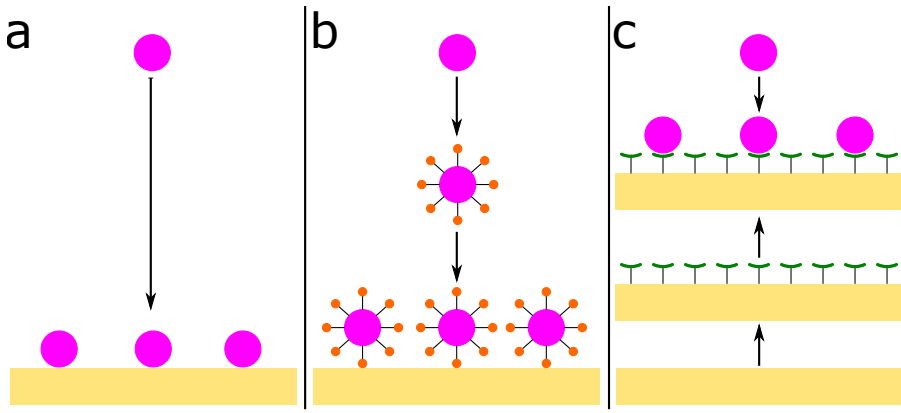


FIGURE 2.4: (a) Scheme shows the direct deposition of SMM on a surface. In this case, weak non-covalent interactions links the SMMs and substrates (b) Scheme shows deposition of functionalized SMMs on a bare surface. Here, Violet colour represents the SMM and orange colour represents the linker groups. (c) In this scheme, substrate is pre- functionalized with specific a linker group. The SMMs are deposited on this substrate.

The absorption of the SMMs on the surface can improved by functionalizing the molecule, the surface or the both. The scheme involved in the functionalisation are shown in figure 2.4. When the molecule is deposited on a bare surface it is immobilized mainly by the weak non- covalent interactions. This interaction can be improved by adding linker groups. The linker group makes covalent bonds with the substrate and helps the SMM to attain better absorption and stability. Alternatively the surface can be pre-functionalized before deposing the molecule. This is shown in 2.4 c. Coronado **et al.** used this pre-functionalisation technique to immobilize Mn12-SMM on a gold surface [45]. They successfully managed to adsorb polycationic SMM onto self-assembled monolayers on a gold surface. They showed that this method is better for the stability of the molecule when compared with those deposited directly on bare gold. The scheme of this method is shown in figure 2.5. This method also helps in controlling the orientation of the molecule which in turn helps in fixing the direction of the magnetic axis of the molecule.

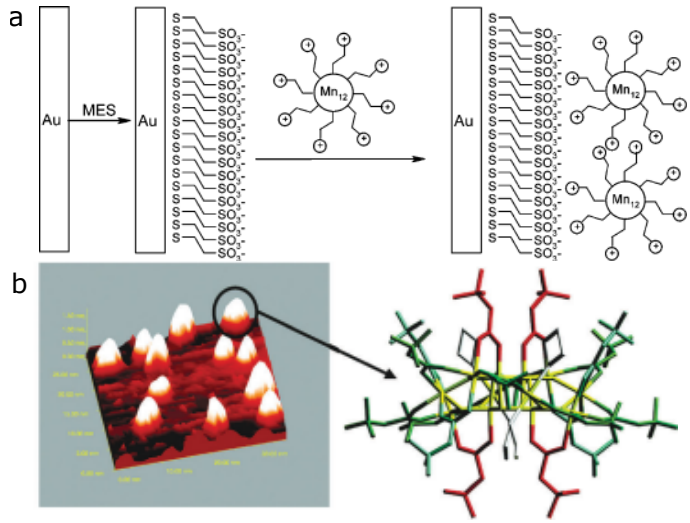


FIGURE 2.5: (a) Scheme shows immobilization of SMM through electrostatic interactions of polycationic Mn12 molecule on a Au surface prefunctionalized with anionic self-assembled monolayers (b) constant current STM of the SMMs once grafted on the surface. Images from ref [42, 45]

These are some commonly employed deposition techniques used for depositing SMMs on surfaces for the scanning probe technique based investigation. There are other deposition method such as stamp-assisted soft lithographic techniques, electronic lithography techniques, etc. for making arrays of SMMs [42]. However, the review is restricted to the main methods used to attain isolated SMMs for scanning probe measurements.

## 2.3 Sample Preparation and Characterization

In the previous section, various approaches to deposit molecules on surfaces were discussed. DyW30 is a molecule belonging to polyoxometalate family that shows interesting physical properties [4]. To explore the properties using STM, this molecule has to be deposited on a conducting surface. Gold is an ideal candidate deposit molecule since it is very stable under ambient conditions

and less reactant to commonly used solvents. In this section, various strategies employed to deposit the molecule on gold surface are described..

We used Gold deposited on Quartz purchased from Arrandee as the substrate. The substrates were flame annealed with a butane flame prior to deposition. Flame annealing promotes the formation of large atomically flat terraces of Au(111). Details of synthesis and characterization of DyW30 are described elsewhere [46]. The chemical structure of DyW30 is shown in Figure 2.6. The lanthanide ion, Dy3+, is encapsulated by an oxometalate capsule. The molecule has a diameter of 1.84 nm and a height of 1.34 nm.

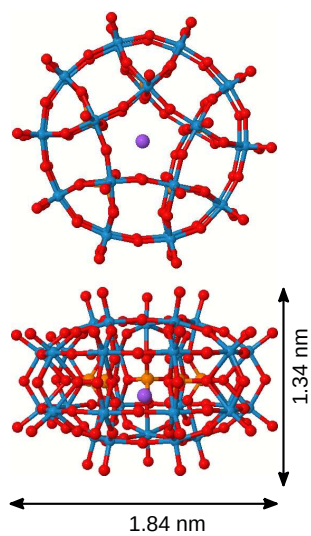


FIGURE 2.6: $[DyP_5W_{30}O_{110}]^{12-}$ polyoxometalate molecule (red: oxygen; blue: tungsten; orange: phosphor; violet: dysprosium).

We used water as the solvent. Powdered samples of DyW30 were dissolved in milliQ water to prepare molecular solutions of various concentrations, ranging from $10^{-5}$ Molar to $10^{-9}$ Molar.

### 2.3.1 Drop casting

At first, the molecules were deposited using the drop casting method, which involves transferring a drop of molecular solution over a substrate ( in this case Au(111) ) and keeping it in the presence of an inert gas until the solvent totally evaporated. The diameter of the deposited drop varied from 3-5 mm. These large drops of water solution take 4 - 6 hours to dry completely. This slow evaporation of the solvent eventually leads to supersaturation and favours the formation of crystals. The formation of the crystals is independent of the concentration of the solution. An optical image of crystals formed on the gold surface is shown in Figure 2.7a. Thick crystals are found along the boundary of the droplet while the inner part shows dendrites with fractal patterns (top part of Figure 2.7a.). Figure 2.7b shows a dark field optical image of inner dendrites. The Atomic Force Microscope (AFM) image, figure 2.7c, show micron-sized crystals, 40-300 nm height, on the surface. It was also observed that the drops form large contact angles to the substrate, indicating that the solution was not in fact wetting the substrate.

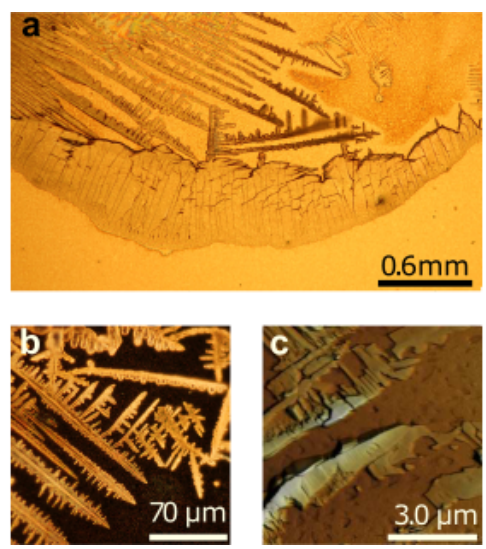


FIGURE 2.7: (a) Optical image of DyW30 crystals deposited over a gold substrate using the drop casting technique. (b) Dark field optical image of the same sample. (c) AFM image of the DyW30 crystals.

### 2.3.2 Spray deposition

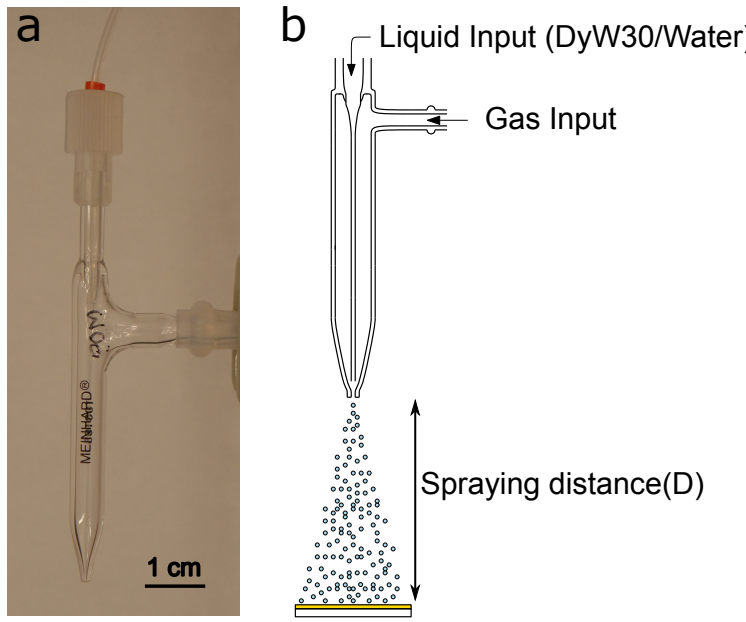


FIGURE 2.8: (a) Photo of Meinhard Nebulizer (b) Schematic of Spraying

The formation of the crystals in the drop casting method is due to the slow evaporation time. A disperse molecular coverage is attained if a faster drop evaporation technique is employed. It is observed that the spray deposition using a nebulizer (Meinhard TR-30-K1) yields droplets of reduced size [47]. The nebulizer utilize pressurized gas to break down solutions into tiny droplets. This method was employed by Červenka *et al.* to obtain a monolayer of $C_{60}$ molecule. They sprayed $C_{60}$ molecule dissolved in various solvents with different evaporation time and sprayed them under ambient conditions. They could produce monolayer thick $C_{60}$ films on graphite and gold surfaces depending on certain spraying parameters. They anticipated that this spraying method could be used of thermally unstable molecules. The deposition process mediated by an ultra-thin solution film on a sample surface. These tiny droplets sprayed by nebulizer have a large surface to volume ratio that results in faster

evaporation, thus preventing crystallization. The aspiration rate of the nebulizer was set at 0.33 mL/min. Helium gas at 1.3 bar was used as the carrier gas. A schematics and a photograph of the nebulizer is shown in Figure 2.8. Spraying was carried out in a fume hood and at ambient temperature. The air flow of the fume hood was temporarily stopped during the spraying.

The parameters controlling the deposition of the molecule on surface are (a) concentration of the solution, (b) evaporation rate of the solvent, (c) the spraying distance, D, and (d) the spraying time [47]. Spraying distance, (D) and evaporation rate of the solvent determines the droplet size. A large D and faster evaporation rate will result in smaller droplets. However, increasing the D would lead to a total evaporation of the solvent before reaching the surface resulting in the formation of large clusters of the molecules. We tried spraying at different distance and found the optimum distance to avoid cluster formation. In order to control the surface coverage, we fixed the spraying distance (D = 30 cm) and spraying time (ts = 5 min) and varied the concentration ($10^{-5} - 10^{-8}$ M).

### 2.3.3 STM and XPS Measurements

We analyzed the resulting samples using a home built Scanning Tunnelling Microscope (STM) designed for room temperature operation. Mechanically cut gold or platinum-iridium wires were used as STM tip. Images were taken at $V_b = +1.3V$ (with respect to the substrate) and low tunneling current $I_t = 0.1nA$..

The STM images (Figure 3 2.9b-e) show samples sprayed with $10^{-5}$, $10^{-6}$, $10^{-7}$ and $10^{-8}$ Molar solutions. We observe that a $10^{-5}$M solution results in full coverage of the substrate (see Figure 2.9b). Samples sprayed with the $10^{-7}$M solution lead to a lower submonolayer coverage with randomly distributed isolated molecules. The images show that the molecules are mostly attached to step edges of gold terraces. Spraying of $10^{-8}$ M solutions yields well separated isolated molecules on the surface. Figure 2.9f shows the line

profile of an isolated molecule. The apparent height of the molecule measured using STM was found to be 0.65 nm. The measured height is lower than the actual height (1.34 nm) of the molecule. This height difference is due to the different apparent barrier height on top of the molecule compared to that of gold.

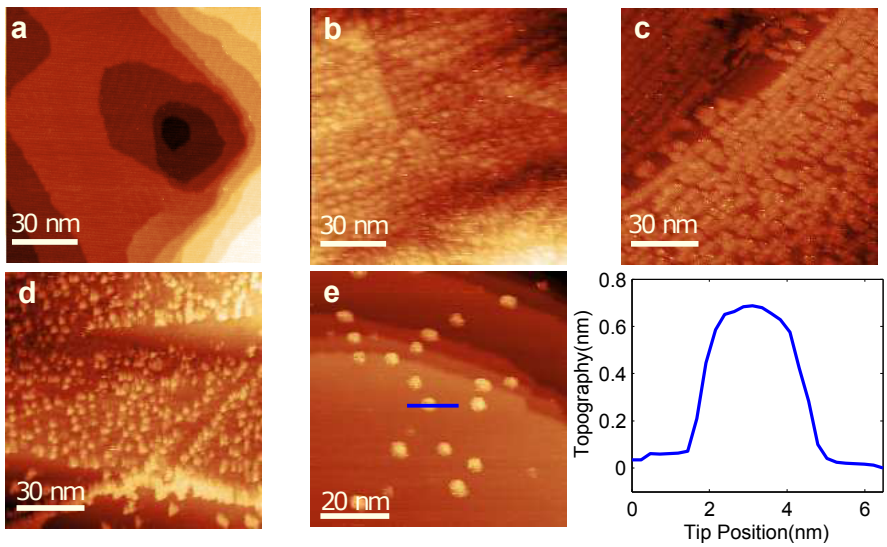


FIGURE 2.9: (a) STM image of Au(111) before deposition (b-e) STM image of surface after sprayed with solution of different concentration. (b) $10^{-5}$ M, (c) $10^{-6}$ M, (d) $10^{-7}$ M and (e) $10^{-8}$ M (Bias voltage,$V_b = +1.3V$, is applied to substrate,$I_t = 0.1nA$,), (f) Line profile along molecule, blue colour refers to the line on image(e). All the images are taken at ambient condition.

We were able to conduct scanning tunnelling spectroscopy (STS) on an isolated molecule by positioning the STM tip on top of one and ramping the voltage while holding the feedback control off (see Figure 2.10). The resulting I-V curve are highly asymmetric. It is important to note here that the molecular conductance is very small for voltages below +0.9 V. Therefore, it is crucial to set bias voltage, $V_b$, above this threshold when imaging samples using the STM in the constant-current mode. For $V_b < +0.9V$, when the tip approaches the molecule the current decreases (see Figure 2.10), producing a vertical approach of the tip to keep the current constant. Consequently,

the tip-substrate distance decreases and becomes too low, resulting in the tip mechanically displace the molecules in the scan direction.

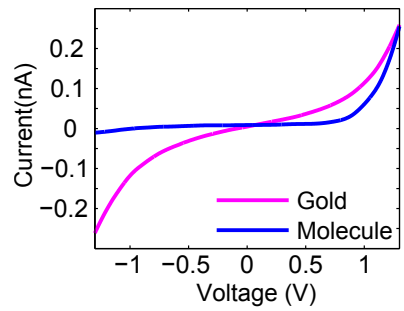


FIGURE 2.10: IV curve taken on clean gold surface (rose) and molecule (blue)

For further verification of the integrity of the molecule on the metal substrate, we have performed X-ray photo-electron spectroscopy (XPS) measurements. This work was done in collaboration with Prof. Roberto Otero Martín at IMDEA Nanociencia, Madrid. XPS experiments were carried out in a UHV chamber, equipped with a hemispherical energy analyser (Phoibos 150 from SPECS) and a monochromatized AlK$\alpha$ X-ray source (1486.74 eV) as incident photon radiation. The samples prepared by spray-deposition method were mounted on the sample holder placed in a pre-vacuum chamber overnight and then subsequently transferred to the XPS vacuum chamber. The residual pressure in the vacuum chamber during data collection was below $5 \times 10^{-9}$ Torr. The binding energies were calibrated to XPS spectra of the bulk line of Au 4f7/2 core level at 84 eV.

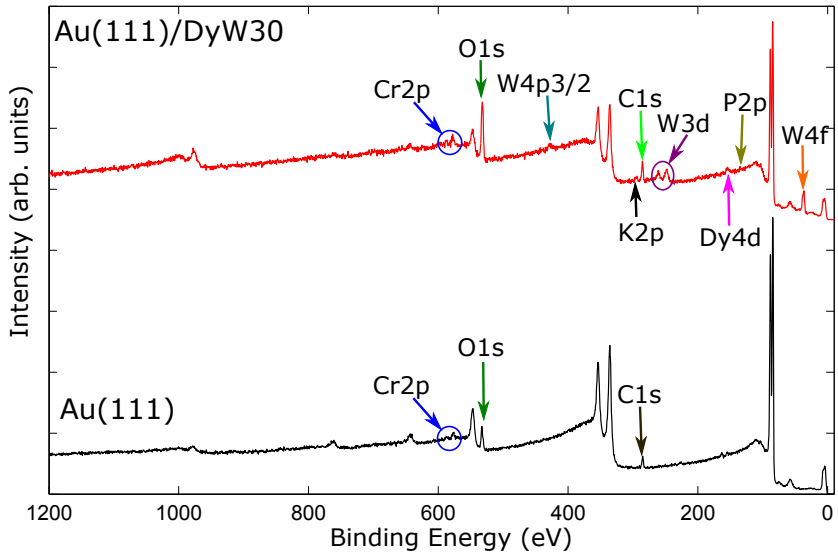


FIGURE 2.11: XPS over a broad range of energies for the sample before (black) and after spray deposition of DyW30 (red)

The figure 2.11 shows XPS survey of bare Au(111) surface (in black) and after the deposition of DyW30 molecules (in red). The bare Au(111) surface can be considered almost clean, however, a relatively small presence of Oxygen and Carbon, due to ex-situ preparation in ambient condition, and Sulfur, due to the contamination of gold, is detected by the XPS. On the other hand, the red wide-scan XP spectrum confirms the simultaneous presence on surface of all the elements (Dy,P,K,W,O) belonging to the molecule under investigation, which revels the efficiency of the deposition method on Au(111) surface. In both the samples there is presence of chromium. This signal is from the underlying chromium, which is used as an adhesive layer for gold.

Figure 2.12 detailed study of XPSpectra. The results shows that all the elements composing the POM under investigation are present on the surface after spray deposition. The intensity ratio between the outermost elements in the polyoxometalate cage, W4f and K2p, corrected with the photo-emission cross-sections yields $2.3 \pm 0.1$, in perfect agreement with the expected value of 2.4 based on the chemical composition of the molecule. For the inner elements,

P and Dy, however, the peaks are significantly attenuated, most likely because they are placed farther away from the sample surface. Also, the binding energy of W4f is in a good agreement with the values found in the literature for other POMs [48]. These results support the idea that the spray method leads to sub-monolayer deposition of intact POM molecules.

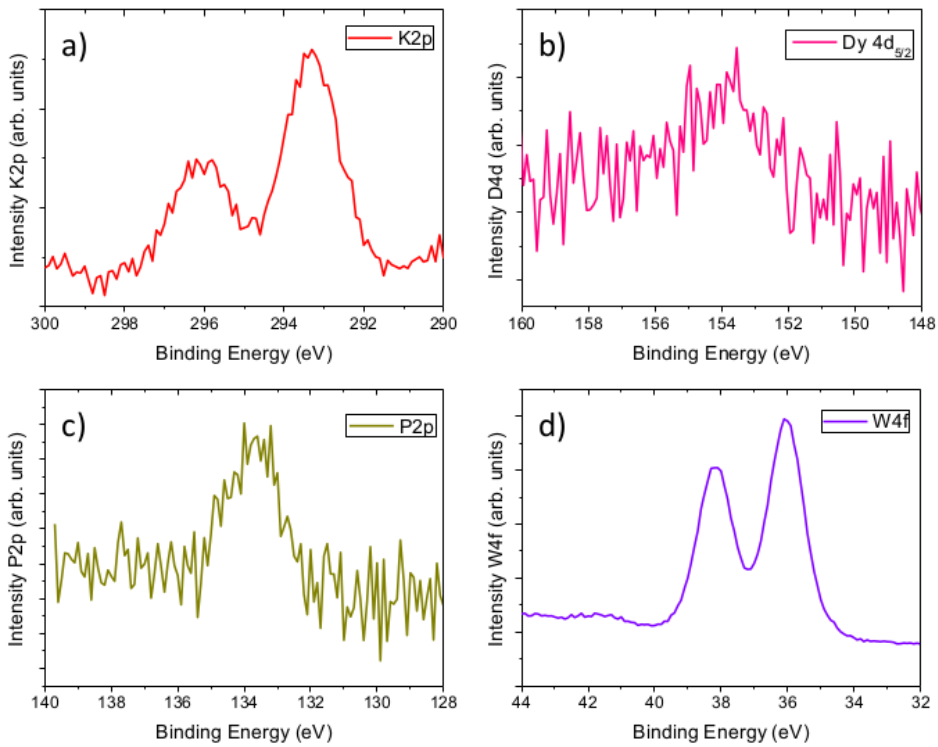


FIGURE 2.12: XPSpectra ($h\nu = 1486.74eV$ ) of the sprayed POM film on Au, showing the main elements in the POM structure: a) K2p, b) Dy4d, c)P2p and e) W4f

## 2.4 Procedure for clean cooling

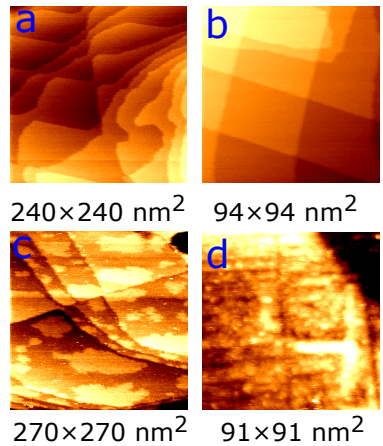


FIGURE 2.13: (a) & (b) shows the STM image of clean gold samples imaged at ambient condition. (c) & (d) shows the STM image of same sample after cooling down to 77 K

One of the biggest challenges in the wet sample preparation method is the surface contamination. To carry out the sensitive measurements sample has to be cooled to cryogenic temperature. The Figure 2.13 a & b shows the STM images of a gold sample taken at ambient conditions. The image shows that the surface is clean and void of contaminants. After cooling down to Liquid Nitrogen temperature, we investigated the sample again. The Figure 2.13c & d shows the STM images taken at 77 K. The surface is contaminated with impurities. This could be due to the pumping system employed. There is a possibility that a very small volume of oil used in diffusion pump may escape to the IVC and contaminate the surface.

In addition to that, at low-temperature, the residual solvents used in the sample preparation may also freeze on the surface and hence contaminate the surface. The use of volatile organic solvents such as Acetonitrile, Dichloromethane (DCM), etc. which evaporates faster without leaving marks on the surface helps to get rid of such contamination to some extent. However, the solvents are unique to the molecules. In this particular case, the water turned out to be

the sole solvent compatible with DyW30. Most of the contamination occurs while cooling the sample to low temperature.

One way to get rid of such contamination is to cleave the sample after cooling down to low temperature. This produces a fresh surface which is devoid of contamination. This method is ideal when one is interested in investigating the surface. Cleaving the surface after depositing the molecule is not possible since the cleaving will remove the top layer which contains the molecule. This is also one reason for depositing molecules at UHV conditions. To investigate the molecules, deposited using wet deposition techniques, we developed a clean cooling procedure that keeps the surface clean during cooling down. This procedure was developed with the help of Prof. Sergey Kubatkin, and Prof. Andrey Danilov from the Chalmers University, Sweden.

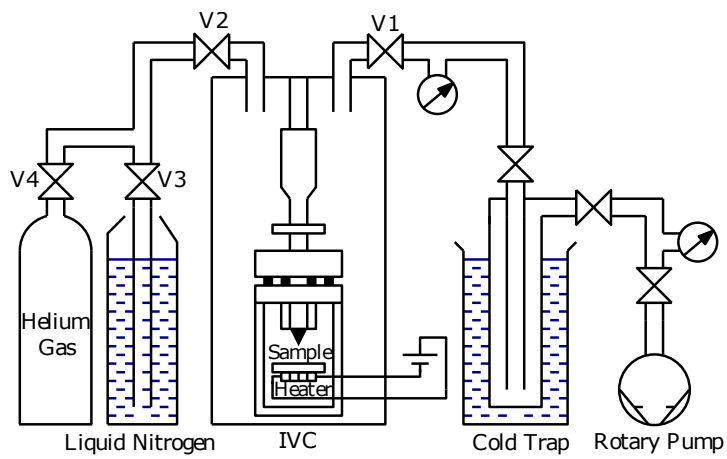


FIGURE 2.14: Schematic for clean pumping procedure

Figure 2.14 shows the schematic of the experimental set-up. The inner Vacuum chamber (IVC) is equipped with a $^3$He cryostat. The STM is attached to the base of the $^3$He cryostat. The sample for measurement was transferred to STM immediately after deposition of molecules. After moving the sample to STM sample holder, IVC was sealed using indium O-ring. The IVC was pumped to vacuum using a rotary vane pump. Sometimes, turbo-pump was also used. The pumping line was connected to a liquid nitrogen cooled cold

trap to ensure clean pumping (see figure 2.14). The Cryotrapping, based on condensation of gases on a cold surface, is an efficient way of vacuum pumping at cryogenic temperatures. Most of the contaminants such as water, hydrocarbons, oil from pumping system, etc. condense about 100 K [49] and inert gases, hydrogen, etc. at helium temperature [50]. This ensures that the diffusion oil or any other contaminants are not passing to the vacuum chamber. The sample holder was kept at $40^0$C during pumping with the help of resistors attached to the sample holder. When the pressure of the chamber reaches below $10^{-3}$ millibar, pumping line is closed momentarily by closing valve V1. Then the chamber was flashed with Nitrogen gas, which is directly evaporated from the Liquid Nitrogen by opening V2 and V3 momentarily. After Nitrogen flashing, valve V1 is opened, and the chamber is pumped with the rotary pump until the pressure drops to $10^{-3}$ millibar. This process was repeated twice. This process helps to remove residual gases present in the chamber. Finally, IVC is filled with the exchange gas, Helium. The IVC is then transferred to the dewar and cooled to helium temperature. Temperature of the sample holder is maintained at $40^0$ C while cooling down the IVC. The walls of the IVC are in contact liquid Helium. Liquid Helium cooled IVC walls act as cryotrap.The pressure can be as low as $10^{-14}$ mbar at helium cooled systems[51]. An activated carbon sorption pump is also present at the IVC. When the temperature drops to cryogenic temperature activated charcoal adsorbs Helium gas and remaining residual gases. At this low pressure along with the high temperature, $40^0$ C maintained at the sample removes most of the residual solvents and gases adsorbed on the sample. The heater is kept in ON state till all other parts are cooled to a lower temperature. This heat gradient also helps to remove the solvents from the surface. The system is kept in this state for some time (approx 2 hours), and then the heater is turned OFF. This time cooling will be slower since there is no exchange gas inside the system. All these process helps to attain a clean surface while cooling down. However, the top part of the IVC is at room temperature, and there is a possibility that the desorbed gasses from these parts might move towards a cold region of IVC. This contamination possibility is prevented by

placing helium cooled metallic plates at some distance from the opening of tubes entering IVC.

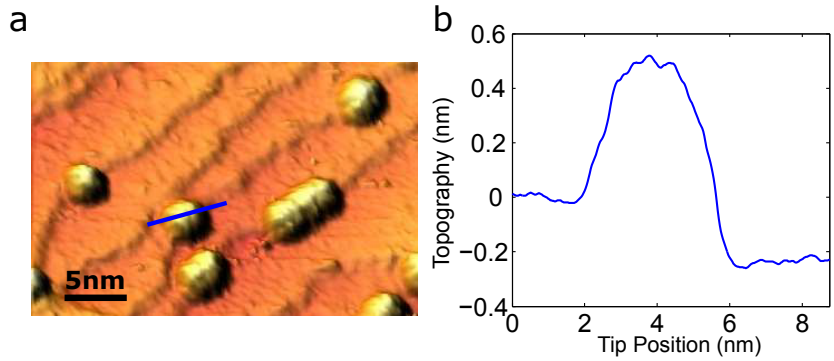


FIGURE 2.15: (a) STM Image of DyW30 on gold taken at 350mK. (b) Line profile of molecule adsorbed on step edge

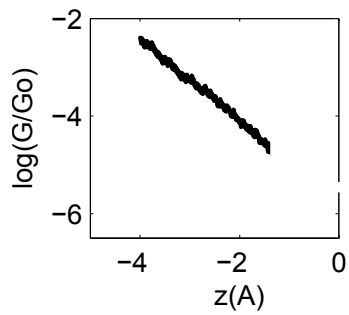


FIGURE 2.16: Conductance- distance curve taken on clean area (average of 10 curves) at 350 mK

Figure 2.16.a shows the STM image of the surface measured at 77K. This image clearly demonstrates that the surface is clean, and molecules can be stably imaged. Work function on clean areas was measured by taking Conductance-displacement $(G - z)$. The ork function calculated from the $log(G) - z$ plot is 3.7 eV. This value is lesser than the observed work function ( 5.1 eV) for gold prepared in Ultra High Vacuum (UHV) conditions. However, this is expectable in the case of sample prepared by the wet sample preparation methods. Some areas were contaminated during this procedure as well. But most of the areas are clean, and molecules can be clearly distinguished.

## 2.5 Conclusions

The results show that SMMs can be controllably deposited using the wet spray coating technique. STM results demonstrate that molecules stay intact on the surface. This method allows us to obtain sub-monolayer coverage that is an essential requirement to probe and address individual molecules. This method can be readily adapted to deposit any molecules that cannot be deposited by conventional methods. XPS confirms that the molecule stays intact upon deposition over the gold surface. A clean cooling down procedure compatible with wet sample preparation method was developed. The results show that the procedure helps to maintain the surface clean at low temperature.

# Part II

# Molecular Rectifiers

# Chapter 3

# Molecular Rectifiers

Molecular rectifiers are molecule-based electronic devices that function as a rectifier of electric current. In this chapter, the main advancements in the field of molecular electronics are reviewed with a focus on the molecular rectifiers. Rectifiers are the electrical devices that convert alternating electrical current to direct current. The first part deals with the historical development of the macroscopic rectifiers and the demands that led to the miniaturisation of these devices. The second part deals with the various mechanisms involved in the rectification process in molecular devices.

## 3.1 Review of Rectifiers

### 3.1.1 Vacuum-tube Diodes

Non-linear electronic elements play a vital role in the electronics industry as these elements form the vital part in logical devices. The predecessor of most of the current controlling devices used nowadays are Fleming diode valves invented by John Ambrose Fleming [52]. This device consists of two electrodes (hence the name diode) placed in a vacuum tube. The working principle of this diode is based on the thermionic emission. Schematic of the thermionic diode

device is shown in the Figure 3.1. One of the electrodes, cathode, is a filament that is heated to emit thermionic electrons. These hot electrons are collected by the other electrode, anode, which is kept at normal temperature. When a positive potential is applied to the anode, hot electrons from the cathode move toward anode producing a direct current flow in the circuit. Conversely, when the negative voltage is applied to the anode, there will not be any flow of current as the 'cold' electrons from the anode cannot flow to the hot cathode. When an AC signal is applied across this device, then it will only allow the positive cycles to pass through it. A rectifier is defined as a two-terminal device that allows the current to flow for a given polarity of the applied voltage in terminals but blocked when the polarity is reversed. Thus, Fleming valve became the first practical rectifier. Figure 3.1b shows one of the first diodes made by Fleming. Shortly after the invention of Fleming diode, Lee De Forest developed a better current controlling device by adding a third electrode between anode and cathode [53]. These discoveries commenced development of a lot of electronic elements such as diodes, amplifiers, oscillators, switches based on vacuum tubes. These vacuum-tube based devices dominated the first four decades of the 20th century. The disadvantages of tubes were that they were bulky and had high power consumption.

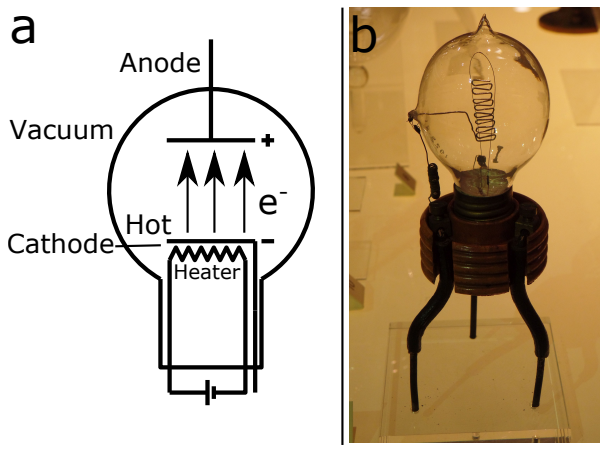


FIGURE 3.1: (a) Schematic of a thermionic diode (b) One of the first thermionic diode valve used by Fleming. Science Museum, London.

Rectification in metal sulfides (Karl. F. Braun, 1874) and Point-contact (J. C. Bose, 1904) were known before the use of vacuum tube based devices [54–56]. Even though these devices were used for particular applications, it could not replace vacuum tubes. A boost in the field occurred with the development of advanced metallurgical processes which resulted in the production of highly pure semiconducting materials and hence led to the discovery of p-n junction semiconducting diode [57]. Another breakthrough in semi-conducting devices came in 1948 with the invention of transistors using point contact junction made on germanium by John Bardeen and Walter Brattain[58, 59]. Following this William Shockley devolved a theory for diodes and bipolar junction transistors [60]. Because of small size, electronic circuits with more transistors could be integrated in one single device. However interconnects used to link transistors caused sufficient delays [61]. In 1958, Jack Kilby overcame this problem by fabricating several devices on a single silicon substrate and connecting it using wire bonding, resulting in the first integrated circuits. Field-effect transistors later replaced bipolar junction transistors. This was followed by a competition to integrate more and more devices on a single silicon chip to increase computational power. Gordon Moore noticed that the number of transistors in integrated circuits grew exponentially with time [1]. The observation he made is now known as "Moore's law". Figure 3.2 shows the number of transistors in Intel processors is plotted as a function of time. This increased number of components in integrated circuits increased the speed of computing. Semiconductor industry uses new techniques for reducing the size of the devices. Various lithographic techniques are used to make mass production of silicon based semiconducting devices. At present, these techniques have succeeded in developing 22 nm devices [62]. Fabrication of further small devices using current techniques are technically challenging and are not economically viable [63]. An alternative way to overcome this limit is to fabricate the nano-scale device using "bottom up" strategy. In the bottom-up approach, chemical or physical methods are used to construct large structures from smaller basic structures such as molecules, nanowires, etc. [64].

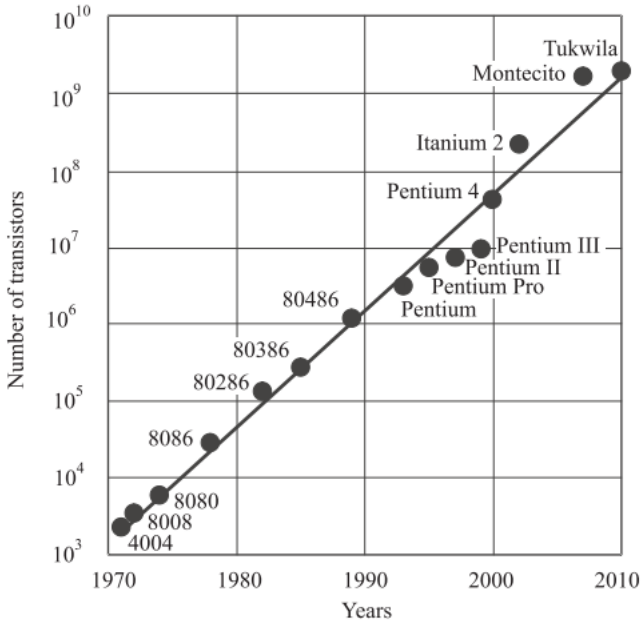


FIGURE 3.2: Number of transistors in successive Intel processors as a function of time. figure from [65]

### 3.1.2 p-n Junction Diodes

It is necessary to describe the working of semiconductor diodes before discussing molecular diodes. Semiconductors are those materials whose electrical resistivity is between conductors and insulators. Unlike conductors, semiconducting materials show a decrease in resistivity with an increase in temperature. These properties of semiconductors are due to the small band gap in these materials compared to an insulating material. Silicon and Germanium are the most extensively used semiconductors. Semiconductors in their pure form show very low conductivity and are called intrinsic semiconductors. These intrinsic semiconductors are doped with trivalent or pentavalent materials to improve their conductivity and are called extrinsic semiconductors. Depending on the type of majority charge carriers, these extrinsic semiconductors are classified into two - p -type (holes) and n-type (electrons). p-n junction device is a semiconductor in which a part of it is made out of p-type

material and another part by n-type materials. Schematic of a p-n junction is shown in Figure 3.3b. When a p-n junction is formed, the majority carriers - electrons in the n region and holes in the p region, diffuses across the boundary. After a while, an equilibrium is established in the junction due to the hole-electron recombination( shown in Figure 3.3 b). A contact potential is developed in the region close to the junction, and this potential prevents the further migration of holes and electrons across the junction. The region formed at the interface is devoid of mobile charge carriers and is termed as depletion region.

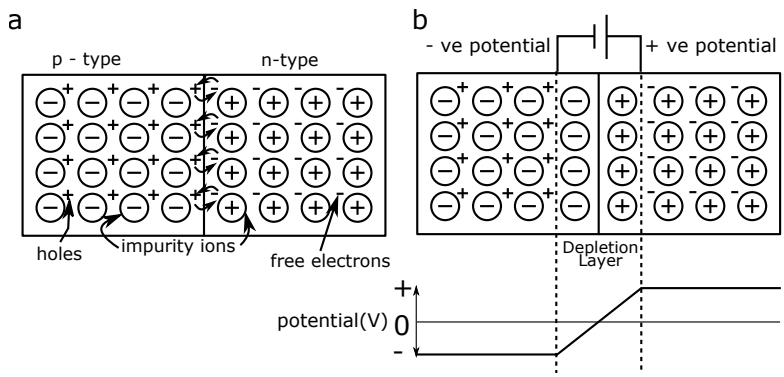


FIGURE 3.3: (a) Schematic showing a p-n junction. (b) p-n junction at zero bias condition.

When a bias voltage is applied across the p-n junction device, then the equilibrium is altered. In the forwards bias condition, a positive voltage is applied to the p region and negative to the n region. The applied potential is in the opposite direction of the contact potential and hence reduces the width of the depletion layer. The electron and holes can easily cross this modified junction and results in an increase in the current through the junction (see figure 3.4a). The forward bias I-V characteristics of Si and Ge are shown in figure 3.4b. The voltage at which the current shows rapid rise is called knee point. The knee point value for Si is around 0.6V, and Ge is around 0.2 V.

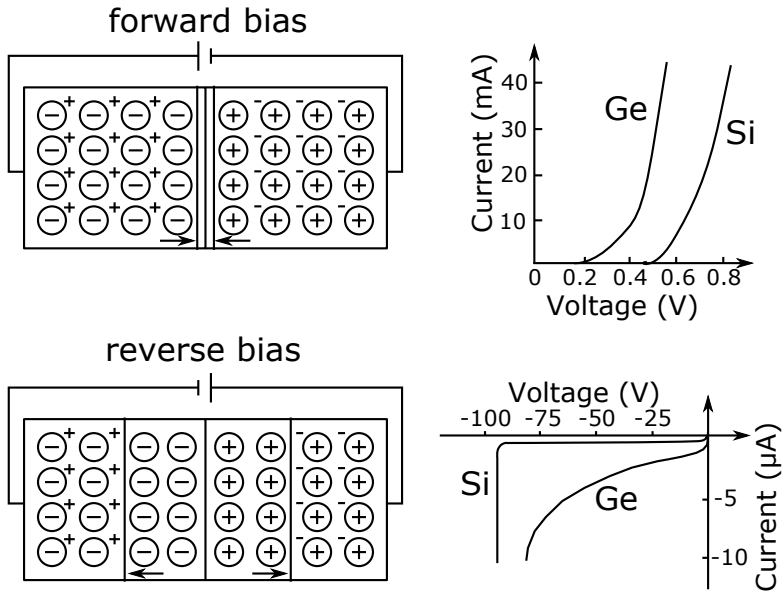


FIGURE 3.4: (a) p-n junction in forward bias condition (b) forward bias IV characteristics (c) p-n junction in reverse bias condition (b) reverse bias IV characteristics

In the reverse bias condition, the p-type region is connected to the negative potential and n-type to the positive potential. The external voltage is in the same direction of the contact potential. This potential drifts the electron in the n region and the holes in the p region always from the junction. This results in the increase in the width of the depletion layer and ideally no current flows through the junction. However, due to thermal excitations, some electrons and holes are generated in the p region and n region respectively. These thermally generated electrons and holes are called minority carriers. These minority carriers are attracted towards the applied voltage and causes a small current across the junction. Reverse bias IV characteristic is shown in figure 3.4c.However, increasing the negative bias voltage above a certain value, breakdown voltage, results in a rapid flow of current through the junction. Thus, a p-n junction offers a low resistance path to current on forward bias condition and high resistance to current on reverse bias condition. Hence, it can perform as a rectifier. In the case of an ideal diode, IV characteristics

are given by the Shockley diode equation [66]

$$I = I_S \left( e^{V/(nV_T)} - 1 \right) \tag{3.1}$$

Where, $I$ is the voltage dependent current passing through the diode, $I_S$ is the reverse bias saturation current, $V$ is the voltage applied across p-n junction, $V_T$ is the thermal voltage and n is the quality factor. The thermal voltage, $V_T$ for a given temperature (T) is given by $V_T = \frac{\kappa T}{q}$ where, $\kappa$ is the Boltzmann's constant and $q$ is the charge on the electron. Figure 3.5 shows the effect of temperature on forward bias characteristics of a p-n junction. The knee voltage reduces with the increase in the temperature. The reverse bias breakdown voltage is also a temperature dependent mechanism. For a silicon diode, the reverse leakage current almost doubles for about every 10 K change.

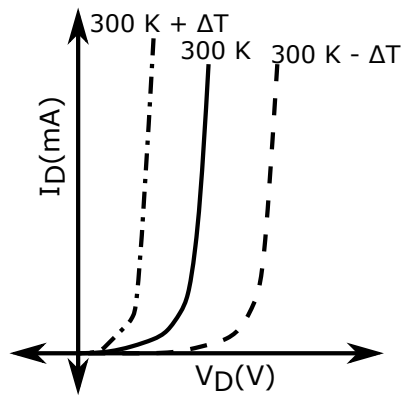


FIGURE 3.5: Effect of temperature on forward bias characteristics of pn junction

One of the main characteristics that determine the size of the p-n junction diode is the space charge region or depletion region. The width $W_{dw}$ of this region is given by [66].

$$W_{dw} \approx \sqrt{\frac{2\epsilon_r \epsilon_0}{q} \left( \frac{N_A + N_D}{N_A N_D} \right) (\Phi_{bi} - V)} \tag{3.2}$$

where $\epsilon_r$ is the relative dielectric permittivity of the semiconductor, $N_D$ ( $N_A$) represents the number of ionized donors (acceptors), $\Phi_{bi}$ is the built-in voltage, and $V$ is the applied bias. This shows that width of the diode depends on the impurity concentration and applied voltage. Typically this width varies from 0.5 microns to few microns in the case of practical diodes [66].

### 3.1.3 Rectification in Molecular Devices

Molecular electronics is defined as the branch of physics which studies the electronics components made out of molecules. This concept was first proposed by Richard Feynman in 1959 [67]. Feynman was much ahead of his time when he proposed this concept. These devices aim to utilize single molecules or group of single molecules to perform various electronic functions. Based on the number of molecules used, these devices are classified into (i) *bulk molecular devices* and (ii) *single molecule devices*. In the bulk molecular devices, a collection of molecules performs the desired action. These devices are analogues to inorganic device such as Si or Ge devices, but the made out molecules (mostly organic ). e.g. organic light-emitting diode, organic solar cell, etc. Meanwhile, single molecule devices are devices based on the functionality of 'just one' Molecule. e.g. Single molecule diode, Single-Molecule Magnets, etc. In this thesis, we concentrate on single molecule devices. Even though the theoretical concept for single-molecule devices were predicted in the 1960s, there was no experimental technique available to address a single molecule at that time. The ability to probe and manipulate individual atoms and molecule came much later after the invention of Scanning Probe Microscopes. These single molecule based systems could lead to an alternative strategy for developing smaller devices. One needs well defined identical molecules for fabricating nano-devices that can be synthesized by chemical processes. Chemistry also allows to incorporate various functionalities in molecular devices. These functional molecules are expected to perform the role of different electronic components. Rectification is one such functionality. As mentioned in the previous section, rectification is commonly achieved using p-n junction

or Schottky diodes. The size of these devices are orders of magnitude higher than the size of the molecule. If a functional molecule can replace these devices then it will help in fulfilling the dream of achieving the ultimate miniaturized devices.

## 3.2 Rectification in Molecular Junction

As described in the Section 3.1.1 rectifiers are devices that allow selective passage of current depending on the polarity of applied voltage. Rectifiers are the simplest of logic circuits. Rectifiers based on molecules were first proposed by Aviram and Ratner in 1974 [3].

### 3.2.1 Aviram - Ratner Model

Aviram Ratner rectifier model for molecular diode is based on a donor-acceptor molecule.[3]. Structure of the molecule is shown in Figure 3.6 (a). Tetracyanoquinodimethane (TCNQ) act as acceptor and tetrathiolfulvalene (TTF) act as donor. A triple methylene bridge separates donor and acceptor. Here, donor means an electron rich unit that can easily donate electrons and acceptor means an electron deficient unit that can readily accept electrons. Methylene bridge connecting the donor and acceptor is an insulating unit that act as a tunnelling barrier. The acceptor region is electro-statically negatively charged, and the donor is positively charged. This results in an electric dipole moment in the direction of transport from acceptor to the donor. This favors transport in one direction. Figure 3.6 (b) shows the energy level diagram of the metal-molecule-metal junction when no bias voltage is applied across the junction. The levels of the donor and acceptor are positioned asymmetrically with respect to Fermi level. During forward bias, the right electrode is in lower potential compared to left, electrons tunnel from the left electrode to right through the molecular level as shown in 3.6 (c). At first, an electron from the left electrode jump to Lowest Unoccupied Molecular Orbital (LUMO) of

the acceptor. From there it jumps to the Highest Occupied Molecular Orbital (HOMO) of the donor through the internal tunnel barrier. And finally it jumps to the metal electrode in the right. In the reverse bias, tunnelling of electrons from the right to left requires more energy to cross the barrier. This asymmetry in the threshold voltage in forward and reverse polarity results in rectification.

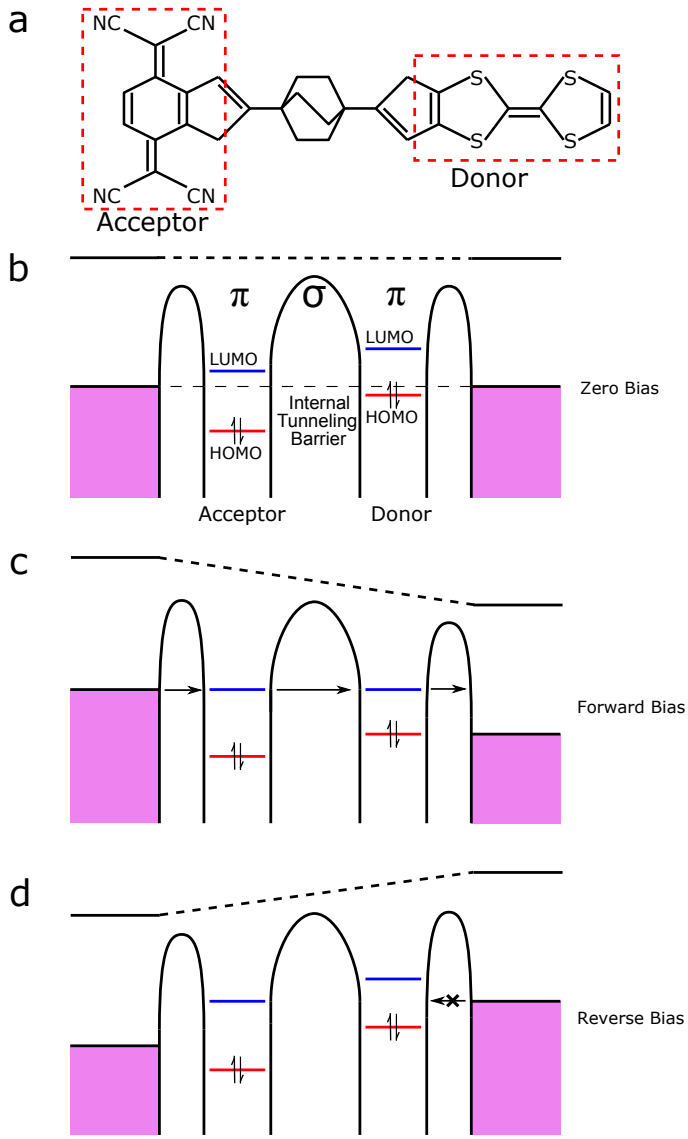


FIGURE 3.6: (a) Structure of the molecule Tetracyanoquinodimethane (TCNQ) (acceptor), tetrathiolfulvalene (TTF) ( donor) and triple methylene (bridge). (b) Energy-level diagrams of the system when the molecule is connected between two metal electrodes,(c) forward bias condition (d) reverse bias condition. Taken from [3, 61]

Scheme for charge transfer in the case of Ratner model in the molecule is shown in Figure 3.7. The Ratner molecule $D - \sigma - A$ is connected between two macroscopic metal electrodes $M_1$ and $M_2$ (In-order to follow the same scheme as in Figure 3.6 we denote it as $A - \sigma - D$).

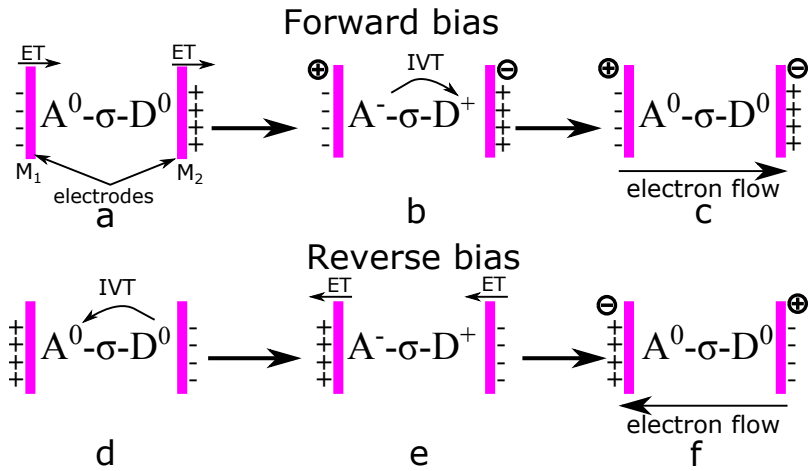


FIGURE 3.7: Scheme showing charge transfer in an Aviram Ratner Molecule (ET- elastic tunneling, IVT- intramolecular intervalence electron transfer) Figure adapted from [3, 68]

When the system is forward biased (Figure 3.7 a-b), electron transfer from $M_1$ and $M_2$ occur in two steps. Electron from $M_1$ tunnel to the Acceptor ($A^0-$) through the barrier, converting it to $A^- -$). Similarly, Donor easily gives an electron to $M_2$ to become $-D^+$). Thus, molecule is in excited state ($A^- - \sigma - D^+$). This makes $M_1$ positive and $M_2$ negative. This step is shown in Equation 3.3.

$$M_1 \mid A^0 - \sigma - D^0 \mid M_2 \xrightarrow{ET} M_1^+ \mid A^- - \sigma - D^+ \mid M_2^- \tag{3.3}$$

In the next step, the molecule returns to the ground state ($A^0 - \sigma - D^0$) by an intermolecular inter-valence transfer (IVT). This step is shown in Figure 3.7 b-c and Equation 3.4.

$$M_1^+ \mid A^- - \sigma - D^+ \mid M_2^- \xrightarrow{\text{IVT}} M_1^+ \mid A^0 - \sigma - D^0 \mid M_2^- \tag{3.4}$$

In the reverse bias, autoignition of the molecule occurs. i.e. an electron from the donor is internally transferred to the acceptor.

$$M_1 \mid A^0 - \sigma - D^0 \mid M_2 \xrightarrow{\text{IVT}} M_1^+ \mid A^- - \sigma - D^+ \mid M_2^- \tag{3.5}$$

Then the molecule relaxes to the ground state by transferring the electrons to electrodes by elastic tunneling as shown in Figure 3.7 d-f.

$$M_1^+ \mid A^- - \sigma - D^+ \mid M_2^- \xrightarrow{\text{ET}} M_1^+ \mid A^0 - \sigma - D^0 \mid M_2^- \tag{3.6}$$

Rectification occurs if step indicated by Eqn 3.3 is more likely than the one indicated by Eqn 3.5.

### 3.2.2 Rectification due to Asymmetric coupling

In Ratner model, rectification arises from the asymmetry in the molecule. Asymmetry in coupling to the electrode can also result in rectification. In 2002, an another model based on asymmetric coupling was proposed by Kornilovitch et.al. [69]. This model based on the spatial asymmetry of the molecule in the molecular junction and attains a high rectification ratio ($\sim$ 500). Unlike the Aviram-Ratner model, this theoretical model requires only a single molecular-level. Scheme of the proposed molecule is shown in Figure 3.8(a). This molecule posses a central phenyl group. Two saturated groups with different lengths separate phenyl group from electrodes. This asymmetric spacer results in an asymmetric voltage drop across the molecule. The larger voltage drop is across the longer spacer group and the smaller voltage drop is across small spacer group.

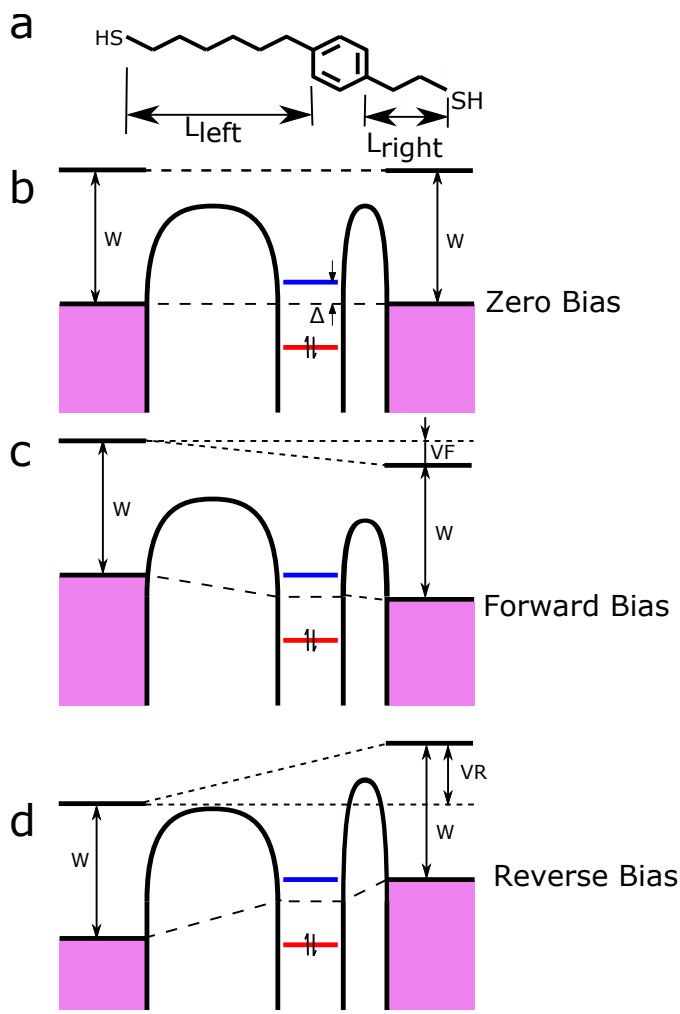


FIGURE 3.8: (a) Structure of the molecule of an asymmetric tunneling barrier molecular rectifier $HS-(CH_2)_m-C_6H_4-(CH_2)n-SH$. $L_{Left}$ and $L_{Right}$ indicate the insulating spacer group connecting molecule and thiol (SH) anchoring group. (b) Energy-level diagrams of the system when the molecule is connected between two metal electrodes,(c) forward bias condition (d) reverse bias condition. Plots adapted from from [69]

Energy level diagram of the molecule in the metal junction is shown in Figure 3.8(b). In the forward bias condition (see Figure 3.8(c)), the voltage applied on electrodes causes adjustment of LUMO of the molecule with Fermi level. This alignment of the LUMO with the Fermi level depends on the voltage

drops which in turn depends on the ratio of lengths of the spacers. When the Fermi level of the right electrode is aligned, with the LUMO, the current passes through the junction. In reverse bias, it requires more energy to move an electron from the left electrode to LUMO of the molecule. Asymmetry in voltage drop causes rectification. This can be explained using a single level model.

### 3.2.3 Single Molecule Diode Experiments

Molecule proposed by Ratner was a theoretical one, often mentioned as "Gedankenmolekäl" and was never synthesized. The first demonstration of a molecular diode was reported in 1997 [68]. They observed rectification in a Hexadecylquinolinium Tricyanoquinodimethanide films produced by Langmuir - Blodgett techniques. This was based on Donor-$\pi$-Acceptor system rather than Donor-$\sigma$-Acceptor system predicted by Ratner. The ground state of this Zwitterion[1] is $D^+ - \pi - A^-$ and excited state is $D^0 - \pi - A^0$.

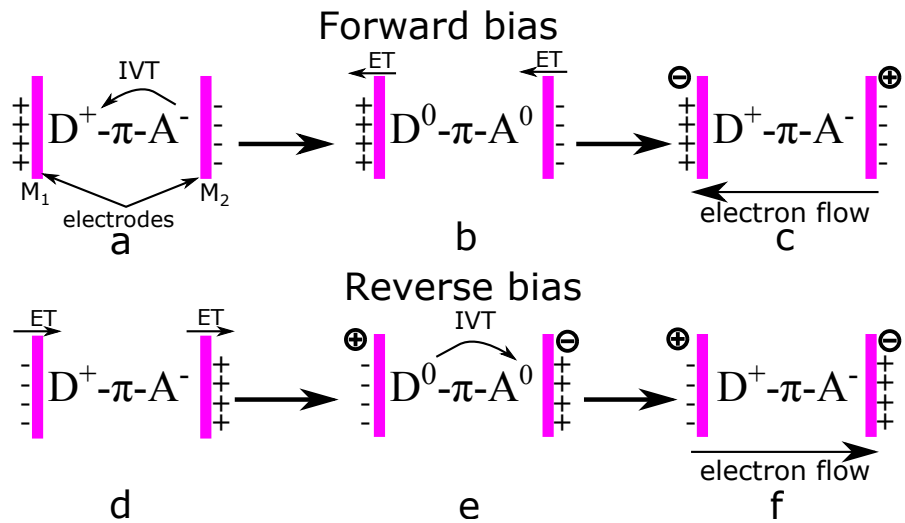


FIGURE 3.9: Scheme showing Rectification in Zwitterion Molecule. (ET- elastic tunneling, IVT- intramolecular intervalence electron transfer) Figure adapted from[68].

[1] Zwitterion is a neutral molecule with a positive and a negative electrical charge

When the system is forward biased, the process can be explained in two-step as shown below,

$$M_1 \mid D^+ - \pi - A^- \mid M_2 \xrightarrow{\text{IVT}} M_1 \mid D^0 - \pi - A^0 \mid M_2 \tag{3.7}$$

here $M_{1,2}$ represents the metal electrodes. In the first step, acceptor part transfers an electron to Donor through intra-molecular inter-valence electron transfer (IVT) process (Fig 3.9.a).

$$M_1 \mid D^0 - \pi - A^0 \mid M_2 \xrightarrow{\text{ET}} M_1^- \mid D^+ - \pi - A^- \mid M_2^+ \tag{3.8}$$

In the next step, these electrons are transferred to the metal electrodes, by elastic tunnelling, to attain the ground state, i.e. $D^+ - \pi - A^-$ (see 3.9.b,c).

In the reverse bias condition, electron from the metal electrode, $M_1$ is transferred to the donor and electron from acceptor to $M_2$. The molecule is in an excited state.

$$M_1 \mid D^+ - \pi - A^- \mid M_2 \xrightarrow{\text{ET}} M_1^+ \mid D^0 - \pi - A^0 \mid M_2^- \tag{3.9}$$

Then an electron from the acceptor is transferred to the donor through IVT to attain ground state. (see 3.9.e,f)

$$M_1^+ \mid D^0 - \pi - A^0 \mid M_2^- \xrightarrow{\text{IVT}} M_1^+ \mid D^+ - \pi - A^- \mid M_2^- \tag{3.10}$$

The system will rectify if the step involved in the forward bias (Equation 3.7)are readily available compared to those involved in reverse bias (Equation 3.9). Metzger demonstrated that zwitterionic hexadecylquinolinium tricyanoquinodimethanide satisfies this condition and shows rectification when

it is connected between gold electrodes. They also developed *cold gold evaporation* technique to deposit top-gold electrode for contacting molecules. Rectification - Ratio (RR) for this molecule varied from 2.4 to 26.4. Figure 3.10 shows the structure of the molecule and rectification observed on the molecule.

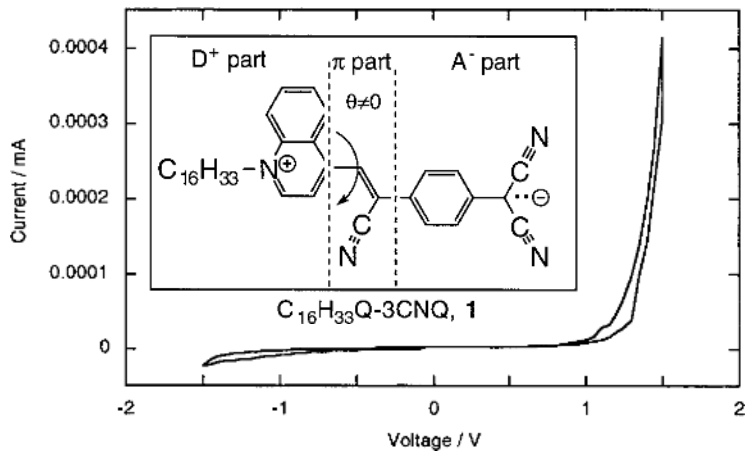


FIGURE 3.10: IV plot showing rectification in Hexadecylquinolinium Tricyanoquinodimethanide. Inset displays the structure of molecule [68].

Few years later, first Donor-$\sigma$-Acceptor Model diode was synthesized by mikayama et. al. [70]. This molecule is a long chain alkyl derivative with a dinitrobenzene moiety (acceptor) and a dihydrophenazine moiety (donor) which is bridged by a methylene group ($\sigma$ group). Langmuir - Blodgett films of this molecule is photosensitive and shows a rectification ratio of 3 in the absence of light and 7 in the presence of light.

In 2002 Ng. et. al. observed rectification in conjugated diblock co-oligomers [71]. STM studies of monolayer and isolated molecule inserted into preassembled monolayers of 1-decanethiol on Au/mica shows rectification ratio of 7 for this monothiol terminated molecule. Jiang et. al extended this work by synthesizing dithol terminated diblock co-oligomers so that the molecule can be incorporated between two gold electrodes. The rectification ratio, in this case, varied from 2-7 [72].

In the same year Kushmerick et.al examined the rectification in cross wire junctions. They observed strong rectification in oligo(phenylene ethynylene) when the connections to electrodes were asymmetric [73].

Elbing et. al. synthesized a molecular rod with a donor and an acceptor unit that was designed to act as a diode when contacted from two sides. This molecule can be viewed as two coupled $\pi$ system and measured by mechanically controlled break junction (MCBJ) technique yielding as rectification ratio of 5 [74]. Rectification and stability of diblock dipyrimidinyldiphenyl molecules with controlled orientation was studied by Diez et al. and reported a rectification ratio of 2.5 [75].

Until 2010, most of the reported rectification ratio values for the molecular system was less than 20. In 2009, Nijhuis et. al developed a technique to measure self-assemble monolayers (SAM) grown on ultra-flat surfaces [76]. Ultra flat surfaces of template-stripped silver supported SAM were measured using a eutectic alloy of gallium and indium (EGaIn), which is covered with a skin of gallium oxide as electrical top-contacts. In 2010 they reported a record RR of $1.3\times10^2$ for (SAM) based tunnel junctions [77]. They measured SAM of ferrocene termini (11-(ferrocenyl)-1-undecanethiol, $SC_{11}Fc$) using liquid-metal top-electrodes.

In 2013, Batra et. al. demonstrated that rectification on a symmetric molecule can be tuned by using asymmetric linker groups [78]. The system they measured consists of a stilbene molecular backbone with a single methylated linker at one and a covalent gold-carbon bond at the other end. The Gold - carbon link is formed in situ through the benzylic trimethyltin functionality. They were able to tune the coupling between the backbone and gold - sulfur bond through chemical modification. They could tune rectification up to 4 by chemical modification.

Recently rectification was observed on diamantane- $C_{60}$ conjugate molecule by Randel et. al. [79]. Self assembled monolayers of this hybrid molecules on gold shows a rectification ratio of 20. Meanwhile $C_{60}$ shows a rectification

ration of $\sim 2$. Figure 3.11 shows the IV curve and rectification of $C_{60}$ and diamantane- $C_{60}$.

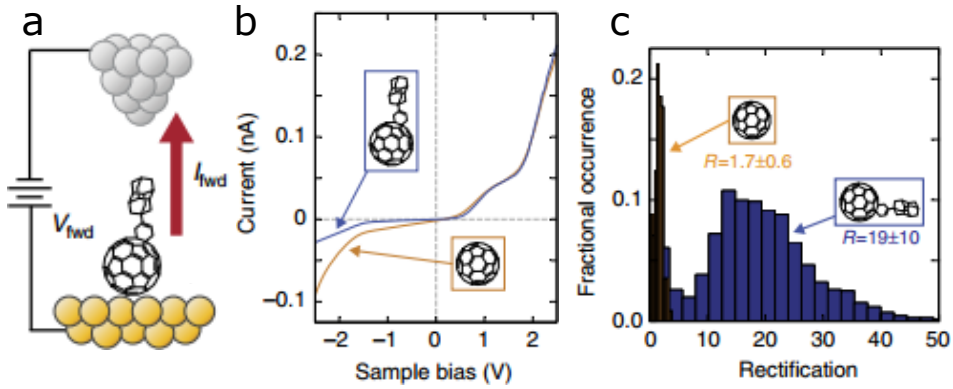


FIGURE 3.11: (a)Sketch shows the orientation of the diamondoid–$C_{60}$ on the gold surface and the direction of forward bias. (b) I-V measurements over diamondoid - $C_{60}$(blue) and $C_{60}$ (orange) molecules. (c) Distribution of the rectification factors determined at ±2.5 V for Dia–C60 (blue) and C60 (black). Images adapted from [79]

TABLE 3.1: Comparison of various molecular rectifiers.

| **Molecule** | **Type** | **Technique** | **RR** |
|---|---|---|---|
| Hexadecylquinolinium Tricyanoquinodimethanide | LB Film | Evaporated contacts, STM | 2-26 [68] |
| (5-(3,5-dinitrobenzyl)-10-octadecyl-5,10-dihydrophenazine) | LB Film | STM | 3 - 7 [70] |
| bithiophene- bithiazole (diblock copolymer) | SAM, isolated molecule | STM | 7 [71, 72] |
| phenyl–ethynyl–phenyl rod | Single or few Molecule | Mechanically controllable Break Junction | 5 [74] |
| oligo(phenylene ethynylene) | Monolayer | Cross Wire | 8 [73] |
| ferrocene termini (11-(ferrocenyl)-1-undecanethiol)$SC_{11}Fc$) | SAM | Liquid metal electrode | $1.3 \times 10^2$ [77] |
| methylated linker -stilbene- covalent gold-carbon linker | Single or few Molecule | STM -Break Junction | 4 [78] |
| diamantane- $C_{60}$ | Monolayer, isolated molecule | STM | 6.5 [79] |

### 3.2.4 Molecular Diode: Summary

Following the Aviram - Ratner model (1974) for molecular rectifier many molecules showing rectification were synthesized. The general characteristic of these systems are a molecule with Donor and Acceptor moieties connected by a bridge group (either $\sigma$ or $\pi$) or sometimes without bridging group ( D-A). Another model was put forward by Kornilovitch based on asymmetric coupling of molecule and electrode. Experiments based on asymmetrically coupled systems also showed rectification. Table 3.1 summarises the main experimental results on molecular rectifiers. In most cases, RR values obtained for molecular diodes are low compared to that od semiconductor diodes. Moreover, the RR in semiconductor diodes increases exponentially with voltage. In the case of molecular diodes, the maximum voltage that can be applied across the junction is less than 4 V. However, the molecular diodes pushed the size of the diode to the nanometre scale. The minimum depletion region that could be achieved for pn junction diode is around half a micron, whereas size of molecular diode are in the range of few nanometres. Even after 40 years, the quest for a molecular rectifier device is a hot topic of research. Both the models proposed for the rectification has been used to explain experimental results. Even though the exact principle of rectification in the molecules is still unsolved and is an ongoing debate.

# Chapter 4

# Rectification in POM and $C_{60}$

In this chapter, we report our results on single-molecule diode based on individual polyoxometalate molecule ($K_{12}(DyP_5W_{30}O_{110}).nH_2O$ ) and fullerene ($C_{60}$). We find that the polyoxometalate molecule gives very high current rectification. In this case, we demonstrate that the rectification arises from the asymmetric coupling of the molecule to the electrodes. We studied the role of electrode coupling in the rectification. The first section of this chapter deals with the experimental results and analysis of polyoxometalate based molecular diode. The second section deals with the rectification in $C_{60}$ molecule. To compare the mechanism, same rectification model was applied for $C_{60}$.

## 4.1 Rectification in POM

The molecule we investigate is $K_{12}(DyP_5W_{30}O_{110}).nH_2O$ is a polyoxometalate. Deposition method for the molecule is described in the previous section molecule. XPS and STM studies show that the molecules are stable on Gold Surface. They are preferably adsorbed on gold step edges.

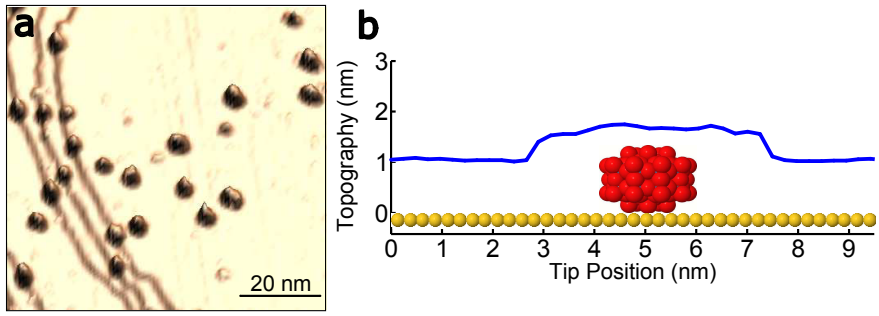


FIGURE 4.1: (a) STM image of molecule at room temperature. Images shows isolated molecules immobilized at step edges and on the gold terraces $V_b = 1.3V, I_t = 0.1nA$(b) topography a molecule taken on a an isloated molecule

After imaging the sample, STM tip was positioned on top of the molecule. I-V characteristics were acquired by ramping the bias voltage while the feedback was suspended. Typical IV curves consist of 1024 data points acquired in about 100 ms. Between -1.3 V and +1.3 V, these I-V curves shows a strongly rectifying behavior with a negligible current for negative voltages and an exponentially increasing current for positive voltages higher than one volt. Figure 4.2 show the IV curve taken on the molecule at ambient condition and low temperature. Rectification Ratio, RR is defined as the magnitude of the ratio of the current for positive and negative voltages, $RR(V) = -I(V)/I(-V)$. Rectification ratio taken at high voltages ($V_b > 1.2V$) give very high rectification ratio. Rectification ratio as a function of voltage is plotted on the inset of Figure 4.2 for both cases. RR is over 250 for the measurement done at ambient conditions. RR is over 600 in the case of low temperatures. Highest RR reported for a "single molecule" is for dipyrimidinyldiphenyl molecule[75]. Higher Rectification Ratio is obtained in the case of self-assembled monolayer (SAM) contacted with liquid metal electrodes ($RR \approx 150$) [77]. RR value obtained for the DyW30 is the highest obtained for a single molecule.

The I-V curves obtained for the molecules can be fitted with Ideal diode equation with an additional tunnelling contribution. In this phenomenological

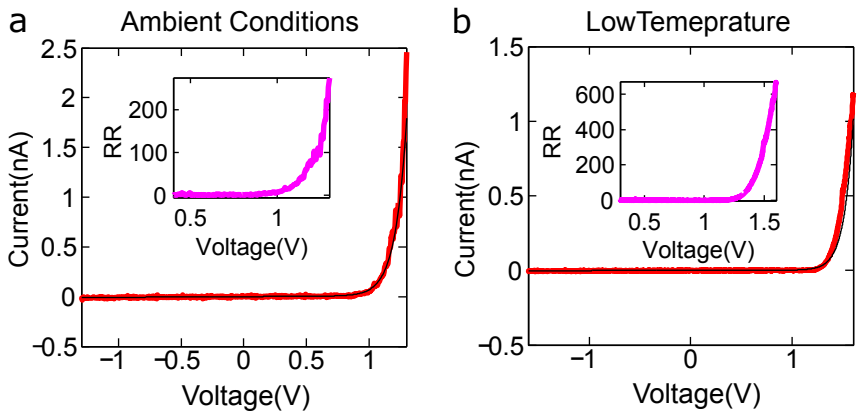


FIGURE 4.2: Tunneling I-V curve above the molecule at (a) ambient conditions and (b) at low temperatures (T = 350 mK). The thin black curve indicates the fit to equation 4.2. The corresponding insets show the rectification ratio as a function of voltage. These curves are an average of 20 individual curves.

model current as function of voltage can be expressed as

$$I = I_0(e^{\frac{V}{V_T}} - 1) + I_D(V) \tag{4.1}$$

The first term of Equation 4.1 corresponds to ideal diode. $I_0$ is the saturation current, and $V_T$ is the thermal voltage of an ideal diode. This is similar to the Equation 3.1, which is for semiconducting diodes. However, in the case of semiconducting diodes, $V_T$ is a temperature dependent function and varies. In our case, $V_T$ obtained for ambient, and liquid helium temperatures is same, $V_T = 0.11 \pm 0.02V$. This shows that the diode term does not show any temperature dependence. The second term $I_D$ in the Equation 4.2 corresponds to a direct tunnelling contribution between the two electrodes. The tunnelling contribution can be written as a cubic function of voltage, $I_D = AV + BV^3$, where A and B are constants. Fitting the IV curve using Equation 4.1 is shown in black color in Figure 4.2.

IVs taken on top of molecules shows an onset of current raising at the positive side (see Figure4.2). This indicates that the LUMO is the dominant level.

This is consistent with the electron acceptor character of the POM cluster [80]. To verify the coupling dependence of the I-V curves was recorded at different tip- molecule separation. This was done by approaching the tip to the molecule at 30 pm steps and acquiring I-V curves at each step. As the tip-molecule separation, $s$ decreases it was observed that for changes in separation in the range $-0.5\ nm < \Delta s < 0\ nm$ , the I-V curves are almost identical, scaling with a factor $e^{(}-\beta\Delta s)$, with $\beta \approx 11nm^{-1}$. This exponent $\beta$ is similar to that corresponding to tunneling on the bare gold substrate in ambient conditions (see Figure). Further reduction in tip-molecule separation results in the saturation of the maximal current leading to an exponential decrease in the rectification ratio RR (Figure 4.3 c and d). This change is related to tip-molecule contact formation and is consistent with the tip height estimated from the apparent height of the molecule on the gold substrate (see Figure 4.1b).

For a functional diode not only a high rectification ratio is needed but also a large enough current. Figure 4.3 c and d shows that currents higher than 100 nA are possible with rectification ratios higher than 100. These currents correspond to enormous current densities of up to $10^7$ A/cm$^2$, which are many orders of magnitude larger than those reported for planar molecular junctions [77], which range from $10^{-2}$ to 1 A/cm$^2$.

### 4.1.1 Results and discussion

A single molecule on an STM junction can be visualized as Figure 4.4a. Equivalent energy level diagram of the metal-molecule-metal junction in STM configuration is shown in Figure 4.4b. The Fermi energy of the metallic leads is between the HOMO (Highest Occupied Molecular Orbit)-LUMO (lowest unoccupied molecular orbital) gap of the molecule. Interaction of the metal electrodes with molecule can lead to rearrangement of Molecular Orbital(MO) and level broadening of the molecule. As shown in Figure 4.4b, many MOs

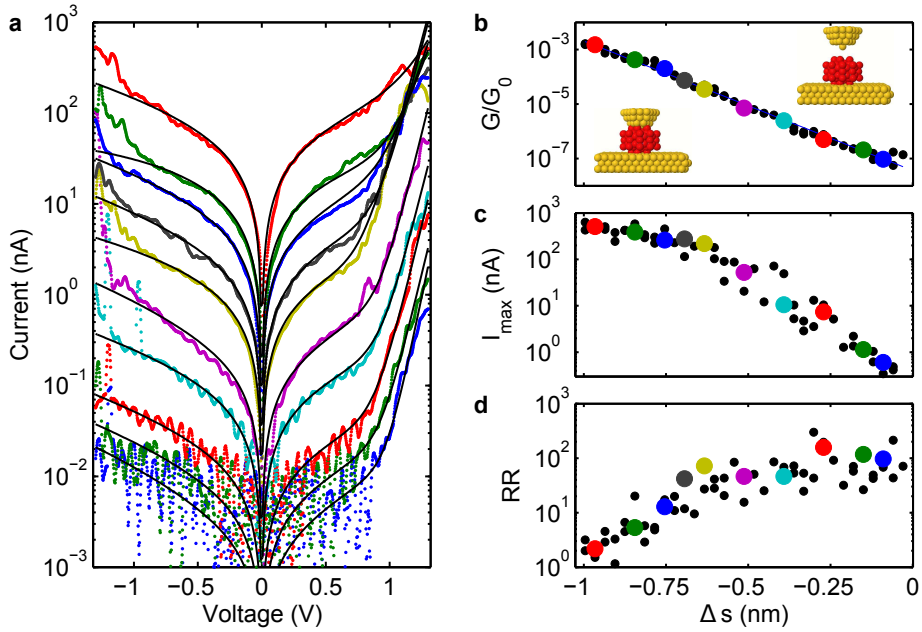


FIGURE 4.3: Tip-molecule separation dependence of rectification in a single molecule junction. (a) A selection of the I-V characteristics acquired as tip-molecule separations is reduced (linear-log scale). The thin black lines are a fit to the diode model described by equation 4.1. Each curve has been acquired in about 100 ms. (b) Low bias conductance (in log scale) as the tip-molecule separation decreases. (d) Maximal current $I_{max}$ at V = +1.3 V. (d) rectification ratio, RR. The black points in b, c, d correspond to the positions where I-V curves have been acquired, the colored points correspond to the I-V curves in a.

are present in the junction, but not all of them participate in the charge transport. In the simplest case, just one level close to Fermi level of the electrodes. The *Single Level Model* is used to describe this situation, where the charge transport through the molecule is dominated by a single level coupled to the electrodes. This model is shown in Figure 4.4c. As in the figure, $\varepsilon_0$ is the position of the level with respect to Fermi-level. $\Gamma_L$ and $\Gamma_R$ are the scattering rates at left and right electrodes respectively. $\Gamma_{S,T}$ determine the coupling of the molecule of the respective electrodes.

I-V characteristics of single level model deduced using Landauer formalism[2]. Evoking this formalism, Voltage dependence of Current can be expressed by

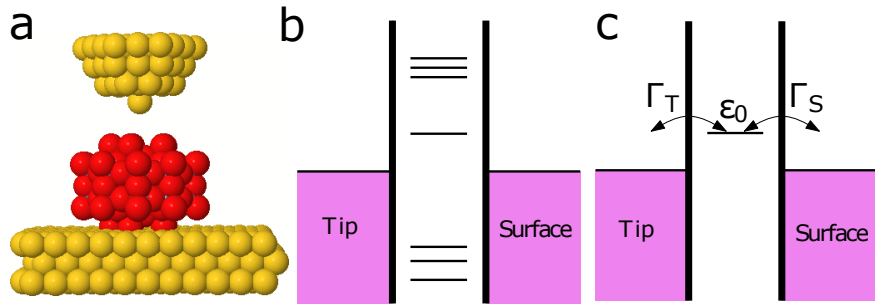


FIGURE 4.4: (a)Cartoon of Molecule in STM configuration forming metal-Molecule-Metal Junction (b) Equivalent Energy Level Diagram of (a), metallic electrodes are filled states up to the Fermi energy and Molecular Orbitals form discrete energy levels (c) Single level model: single level located at $\varepsilon_0$ is the dominant level (in this case LUMO) close to Fermi level .

$$I(V) = \frac{2e}{h} \int_{-\infty}^{+\infty} T(E,V)\ [f(E - eV/2) - f(E + eV/2)]\ dE \tag{4.2}$$

where f(E) is the Fermi function, and T(E, V) is the energy and voltage dependent transmission coefficient, that is expressed by the Breit-Wigner formula

$$T(E,V) = \frac{4\Gamma_S\Gamma_T}{[E - \varepsilon_0(V)]^2 + \Gamma} \tag{4.3}$$

where $\Gamma = (\Gamma_S + \Gamma_T)/2$. $\varepsilon_0(V)$ is the voltage dependent level position. The voltage drop the molecule - metal junction is determined by the scattering rate $\Gamma_{S,T}$. If the coupling of the molecule to the Tip and Surface is different, then the voltage drop across junction also varies. This asymmetry can be taken into account by modeling voltage dependent level position as $\varepsilon_0(V) = \varepsilon_0 + (eV/2)[(\Gamma_L - \Gamma_R)/\Gamma]$. This equation shows that the voltage drop is large at the electrode with the weaker coupling and vice versa. Figure 4.5 shows IVs curves calculated using Equation 4.2 for different ratios of $\Gamma_S$ and $\Gamma_T$. This figure shows that asymmetric in the coupling to the electrodes can lead to rectification.

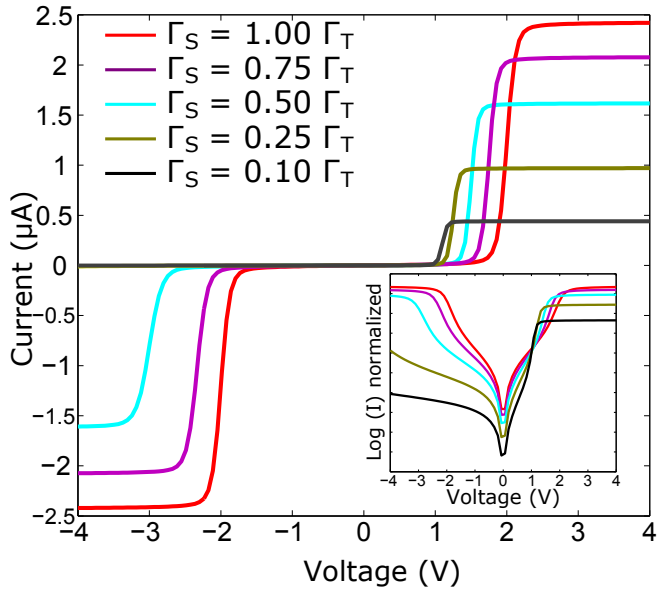


FIGURE 4.5: Simulation of IV curves with asymmetric coupling to electrode using Equation 4.2. T= 300K, $\varepsilon = 1eV$, $\Gamma_S = 50meV$. Inset shows semi log scale plot (log (Current) vs Voltage)

In the light of Single Level model discussed, the rectification in the POM can be modelled based on the asymmetric coupling of the molecule to the electrodes, tip and surface. In this model, which is sketched in Figure 4.6.a, considers two conduction paths or channels: a direct channel (from tip to substrate), giving rise to a current $I_D$, and a molecular pathway involving the electronic structure of the molecule, contributing a current $I_M$. The direct channel takes into account the coupling between the tip and the substrate, and can be described via an energy-independent tunnelling rate. It accounts for the tunnel-like current $I_D$ at low voltage. The molecular channel can be defined in terms of a single-level model. Voltage dependence of the current can be expressed by the equation 4.2. The direct channel involves coupling between the tip and the substrate, and can be described via an energy-independent tunneling rate $\Gamma_D = \pi t_D^2 \rho(E_F)$, where $t_D$ is the matrix element representing the coupling between the two electrodes and $\rho(E_F)$ is the local density of states at the electrodes, which are considered identical [2]. This direct channel

accounts for the tunnel-like current $I_D$, whose linear part can be written as $I_D = \frac{2e^2}{h} 4\pi\Gamma_D \rho(E_F)V$. The molecular channel can be described in terms of a single-level model [81]. In this model, one presume that the charge transport is mainly through the single molecular level. The level position in the absence of bias voltage is measured with reference to the Fermi energy and is represented by $\varepsilon_0$. This level corresponds to the lowest unoccupied molecular orbital (LUMO), for $\varepsilon_0 > 0$ or to the highest occupied molecular level (HOMO), for $\varepsilon_0 < 0$ and is coupled to the metallic electrodes via energy-independent tunneling rates $\Gamma_S$ and $\Gamma_T$, which describe the strength of the coupling of the molecule to the substrate and to the STM tip, respectively. These tunneling rates can be written as $\Gamma_S = \pi t_S^2 \rho(E_F)$ and $\Gamma_T = \pi t_T^2 \rho(E_F)$ , where $t_T$ ($t_S$) is the matrix element representing the coupling between the tip (substrate) and the molecule [2].

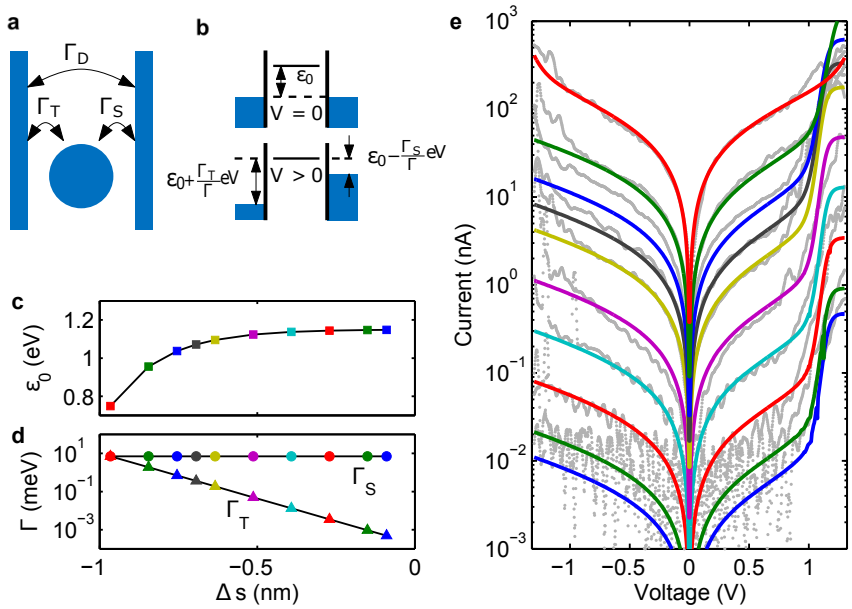


FIGURE 4.6: One-level model with the addition of a direct channel. (a) The molecule is coupled to the substrate and the tip through tunneling rates $\Gamma_S$, and $\Gamma_T$, respectively, and additionally tip and substrate are coupled directly through tunneling rate $\Gamma_D$. (b) Diagram for voltage drop. The position of the level with respect to the Fermi level of the electrodes depends on the applied voltage and the tunneling rates $\Gamma_S$, and $\Gamma_T$. (c), (d) Position of energy level, $\varepsilon_0$, and tunneling rates $\Gamma_S$ (circles) and $\Gamma_T$ (triangles), as a function of tip position. (e), I-V curves obtained from the one-level model (coloured curves) superposed on the experimental curves (gray curves). The coloured symbols in (c), (d) correspond to the coloured curves in (e). [82]

To model the variation in the I-V characteristics as the tip approaches the molecule, we assume that the tip-molecule coupling $\Gamma_T$ and the tip-substrate coupling $\Gamma_D$ have an exponential dependence on tip-molecule separation, $\Gamma_D$, $\Gamma_t \quad e^{(-\beta\ \Delta s)}$, as expected for tunnelling, while the molecule-substrate coupling remains constant. When tip makes a good contact with the molecule, the coupling becomes identical. During this process molecular level, $\varepsilon_0$, may also shift position due to the charge transfer between the molecule and the tip. Figure 4.6e shows the evolution of the I-V curves according to this model, with values for and given in Figure 4.6 c and d. In spite of the simplicity of the model that does not take into consideration level degeneracy, the proximity

of several molecular levels, etc., the model gives a good semi-quantitative agreement with the experiment.

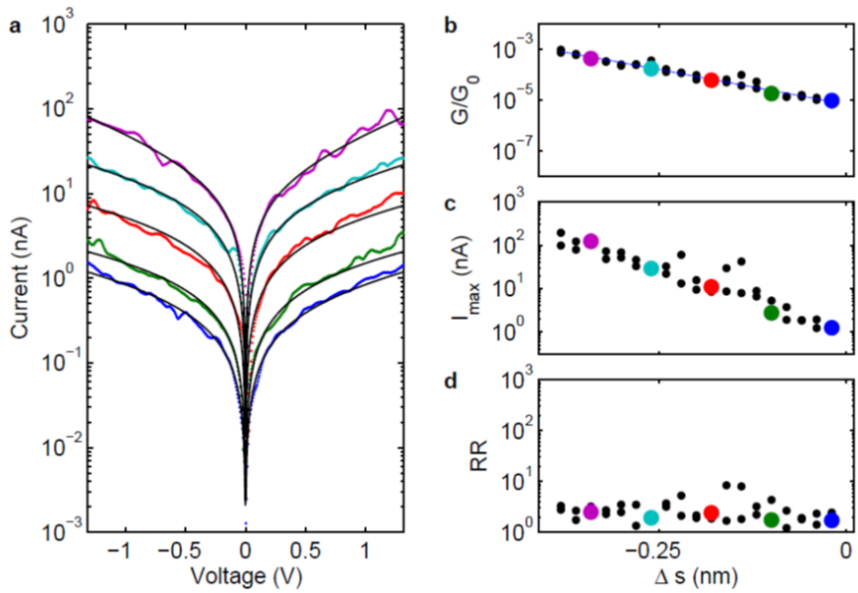


FIGURE 4.7: Variation with tip-substrate separation of the I-V curves on the bare gold substrate. (a) Selection of the I-V characteristics acquired as tip-substrate separation is reduced (linear-log scale). The thin black lines are a fit to a tunnel like current consisting of a linear and a cubic term,I(V) = AV+ $BV^3$, with A and B, constant. (b), (c), (d), Low bias conductance, maximal current $I_{max}$ at V = +1.3 V, and rectification ratio, RR, respectively, as the tip approaches the substrate. From the slope of the low-bias conductance in (b), we obtain, $\beta = 12.5$ nm$^{-1}$. The I-V curves show very slight asymmetries and the rectification ratio RR is approximately one independent of voltage. The black points in b, c, d, correspond to the positions where I-V curves have been acquired, the coloured points correspond to the I-V curves in (a). [82]

To compare the variation in the I-V characteristics as the tip approaches the molecule, the same was repeated on bare gold. Figure 4.7(a) shows the variation in the I-V as tip approaches bare gold. I-Vs are tunnel-like curves that can be fitted with a cubic function, I(V) = AV + $BV^3$, where A and B are constants. The fit is indicated in black colored curves in figure 4.7(a). Conductance vs displacement is plotted in 4.7 (b). $\beta$ obtained from the slope of the (b) gives 12.5 nm$^{-1}$. Rectification ratio obtained for the is, RR =$\sim$ 1.

Comparing this measurement with the one taken on top of the molecule it is clear that asymmetry clearly arises from the molecule.

### 4.1.2 Inversion of rectification

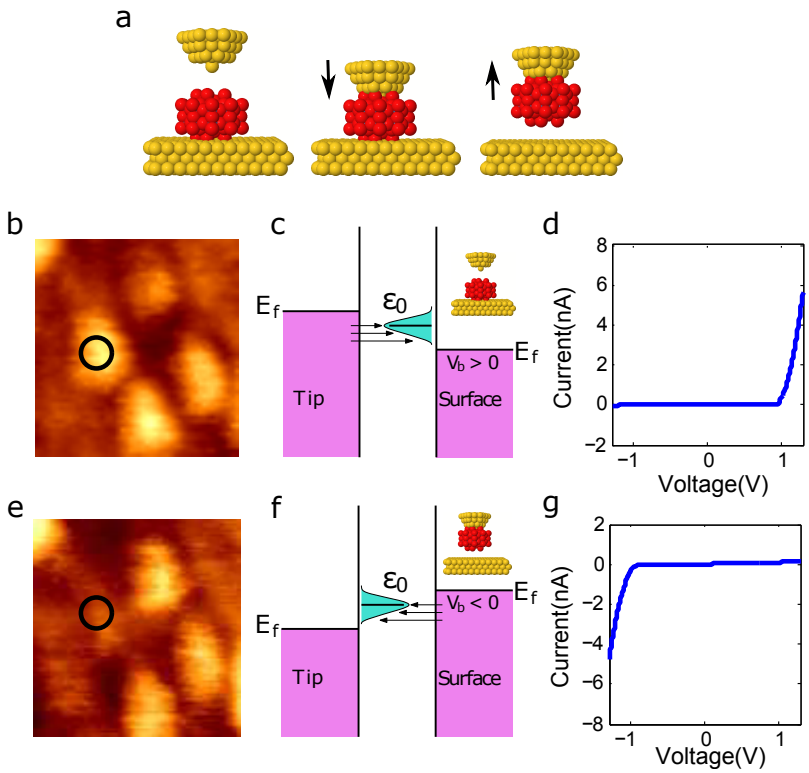


FIGURE 4.8: Inversion of rectification as the molecule is transferred from the substrate to the tip. (a) Cartoon shows the approach of the tip towards molecule and transfer of molecule to tip (b) STM image before approach experiment. (c) Cartoon showing the transport through level $\varepsilon_0$ when the molecule is attached to surface (note that $V_b > 0$) (d) Tunneling I-V characteristic on the molecule in the center of the black circle. (f) Cartoon showing the transport through level $\varepsilon_0$ when the molecule is attached to the tip (note that $V_b < 0$) (g) Tunneling I-V characteristic after performing an approach experiment. The inversion of the I-V characteristic is due to transfer of the molecule to the tip. (e) STM image after approach experiment. The target molecule has been transferred to the tip and then lost during scanning. [82]

The previous section deals with the evolution of IV symmetry with changes tip - molecule distance. Molecules can be transferred to tip during such vertical displacement [83]. During some I-Z approaches, the molecule was transferred to the tip. Cartoon showing Scheme of transfer is illustrated in figure 4.8a. I-V curve took on top of the molecule also give information of the level contributing to the tunnelling current [84]. When the molecule is on the surface, electrons from the tip have access to the single level for bias voltage $V_b > 0$ (see Figure 4.8c,d). This shows that the LUMO is dominant level. When the molecule is on the Tip, the is reversed. The electron has access to the level when $V_b > 0$. This clearly shows that the asymmetry in the I-V arises from the asymmetric coupling to the electrodes as described in the model.

### 4.1.3 Sweeping Molecule

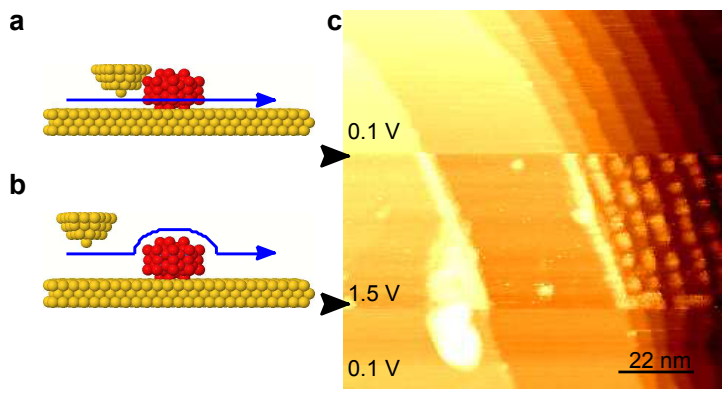


FIGURE 4.9: Effect of bias voltage in imaging $DyP_5W_{30}O_{110}$ polyoxometalate molecules deposited on an annealed gold substrate. STM topographic image starting at the lower left-hand side corner. Initially, a bias voltage of 100 mV was applied to the substrate. At the point marked by the lower arrow, the bias voltage was switched to 1.5 V, and back to 100 mV at the point marked by the upper arrow. At the lower voltage, the molecules are swept by the tip (as illustrated in a). Only at the higher voltage the molecules can be seen by the STM tip (b). [82]

We also observed that the molecules are swept when scanned at a low bias voltage. Figure 4.9 shows STM image when the bias voltage is changed during the scan. STM topography was taken at a lower voltage (0.1 V). Bias voltage was switched to 1.5 V for a certain time and switched back to low voltage. As shown in Figure 4.2 current is small for low bias region. The tip will be closer to the surface and will sweep the molecule as shown in Figure 4.9 (a). At high bias voltage, there is a sharp rise of current on molecule and tip will detect the current and move over the molecule (see 4.9 (b)). Molecules are only visible at high voltage. This also indicated that the molecule is weakly bound to the surface. I.e., coupling of the molecule with the surface is weak.

## 4.2 Rectification in $C_{60}$

For further verification of the molecular rectification due to asymmetric coupling we investigated another molecule. Fullerenes are well-known molecules in molecular electronics. They are easy to deposit and are very stable on the metal surface. Randel et. al. reported that $C_{60}$ shows a rectification of 2 ($I_{ref} = \pm 2.5$) when deposited on Au(111) (see Fig 3.11) [79]. We decided to investigate the role of electrode coupling in rectification on this molecule.

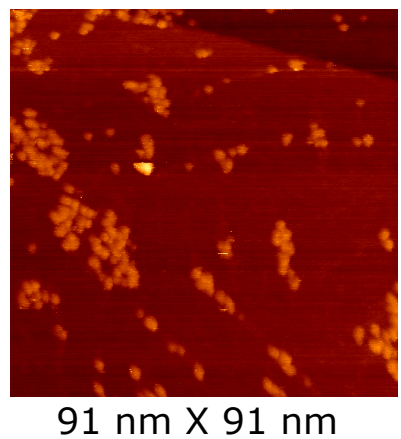


FIGURE 4.10: Large area scan of sample of $C_{60}$ deposited on Au(111) from 1,2,4-trichlorobenzene (TCB) solution

The $C_{60}$ molecules were deposited on the flamed annealed gold surface by drop casting using 1,2,4-trichlorobenzene (TCB) solution and dried it for several hours before measuring with STM [84]. The STM images show small clusters and isolated molecules immobilized at the gold terraces and step edges. After imaging the sample, STM tip was positioned on top of the molecule. I-V characteristics were acquired by ramping the bias voltage between -1.0V and +1.0 V, while the feedback was suspended. Figure 4.11.a show the IV curve took on the molecule at ambient condition. I-V curves show slight rectification of 3.5 at 1 V. This value is in good agreement with the value obtained by Randel et. al. on $C_{60}$ [79]. Figure 4.11.b shows distribution of the rectification ratio determined at $\pm 1.0V$ for $C_{60}$.

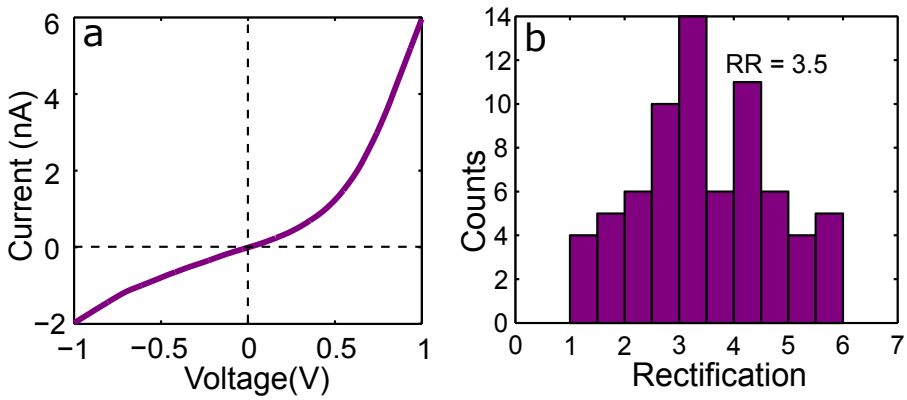


FIGURE 4.11: (a) Typical shape of IV measured over $C_{60}$ molecule (b) Distribution of the rectification ratio determined at $\pm 1.0V$ for $C_{60}$. 77 curves, (bin size 0.5)

IVs taken on top of molecules shows that the current raising is at the positive side, indicating that the LUMO is the dominant level. Unlike DyW30, in this case, other levels also contribute to the conductance. High conductance observed in the case of $C_{60}$, ($10^{-1}$ $G_0$) molecule compared to that of DyW30 ($10^{-3}$ $G_0$) is due this reason. However, there exists an asymmetric coupling in the molecule in STM tunnel junction. To verify the coupling dependence of the molecule we recorded IVs at different tip molecule distance as described in the previous section. The tip was approached until a stable contact is formed

between tip and molecule. Approach curves shows an exponential dependence (linear in semi-log plot) below ($10^{-1}$ $G_0$). Tip makes a contact with the around $10^{-1}$ $G_0$. Further approaching tip towards the molecule results in the saturation of the maximal current leading to a decrease in the rectification ratio RR (Figure 4.12 c and d). This change in RR is due to tip-molecule contact formation.

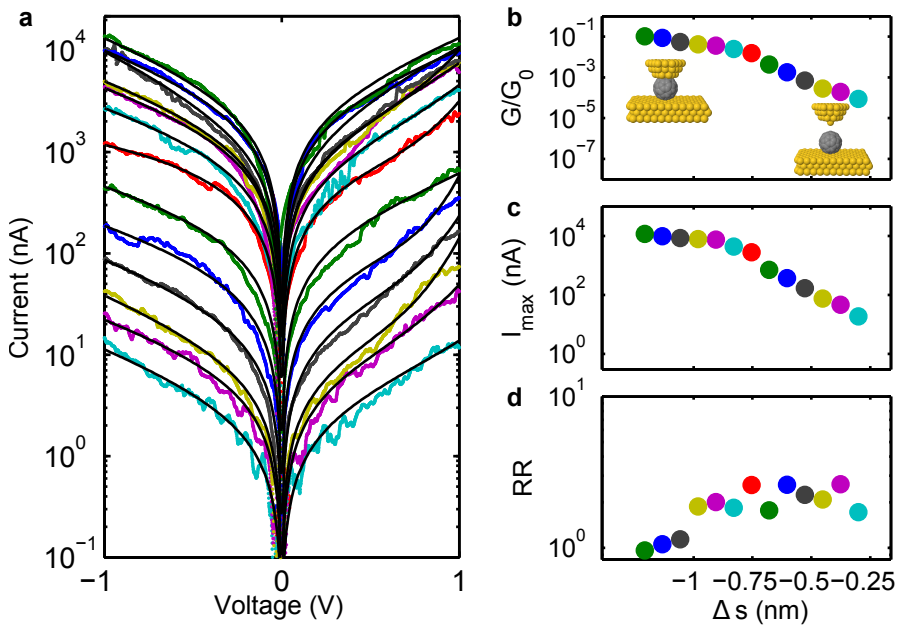


FIGURE 4.12: Tip-molecule separation dependence of rectification in a single molecule junction. (a) A selection of the I-V characteristics acquired as tip-molecule separation s is reduced (linear-log scale). The thin black lines are a fit to the diode model described by equation 4.1 (b) Low bias conductance (in log scale) as the tip-molecule separation decreases. (d) Maximal current $I_{max}$ at V = +1.0 V. (d) rectification ratio, RR. The coloured points in b, c, d correspond to the positions where I-V curves have been acquired, the coloured points correspond to the I-V curves in a.

Similar to the previous section, we recorded I-Vs as the tip approaches bare gold. Figure 4.13(a) shows a variation of the variation in the I-V as tip approaches bare gold. I-Vs are tunnel-like curves that can be fitted with a cubic function, $I(V) = AV + BV^3$, where A and B are constants. Conductance vs

displacement is plotted in 4.13 (b). Rectification ratio obtained for the is, RR $=\sim 1$ and clearly shows that the asymmetry is from the molecule - electrode coupling.

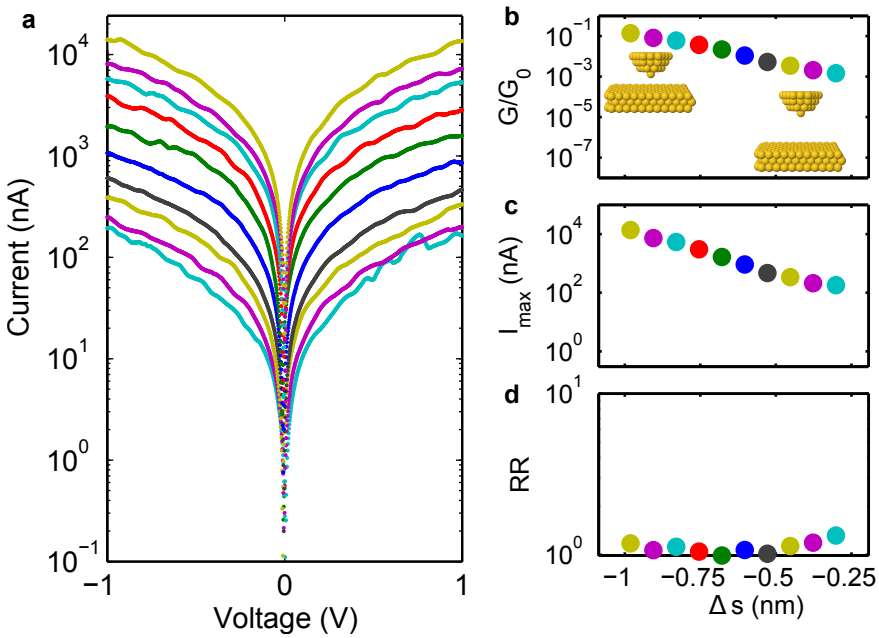


FIGURE 4.13: Variation with tip-substrate separation of the I-V curves on the bare gold substrate. (a) Selection of the I-V characteristics acquired as tip-substrate separation is reduced (linear-log scale). (b), (c), (d), Low bias conductance, maximal current $I_{max}$ at V = +1.0 V, and rectification ratio, RR, respectively, as the tip approaches the substrate. The I-V curves show very slight asymmetries and the rectification ratio RR is approximately one independent of voltage. The coloured points in b, c, d, correspond to the positions where I-V curves have been acquired, the coloured points correspond to the I-V curves in (a).

The Single level model was used to model the IV curve. Figure 4.14.a shows the one- level model (coloured curves) superposed on experimental curves (grey). Figure 4.14.b shows the tunnelling rates $\Gamma$ s with respect to tip position. $C_{60}$ molecules has better coupling to the substrate. $\Gamma_S$, 20 meV measured for the $C_{60}$ molecule is higher than that of the same observed for DyW30 molecule. Also $\Gamma_T$ is also higher in the case of $C_{60}$. Hence, this leads to

reduced asymmetry of the IV curves, i.e. rectification. However, the trends in the evolution of Gammas with respected to the tip-sample separation is same for both molecules. This clearly shows that the asymmetric electrode coupling plays a major role in the observed rectification molecular junctions.

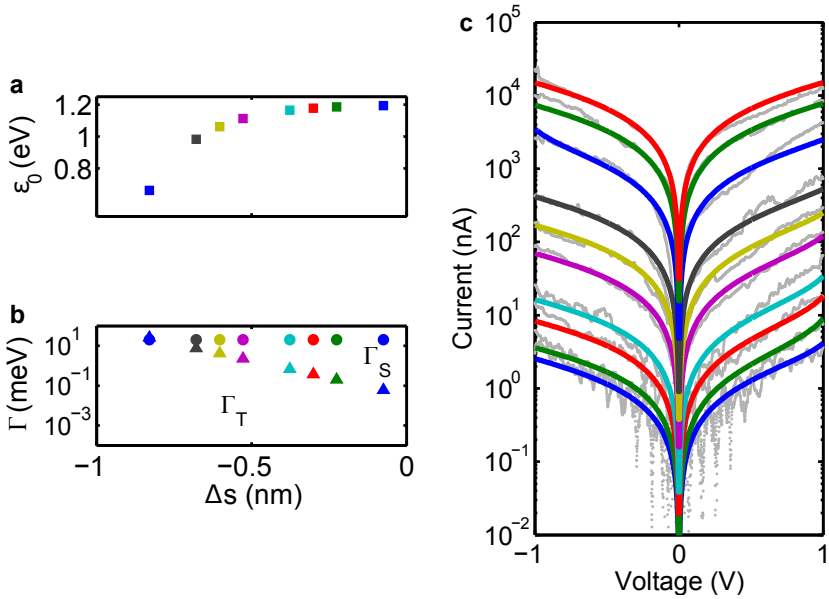


FIGURE 4.14: One-level model with the addition of a direct channel. The position of the level with respect to the Fermi level of the electrodes depends on the applied voltage and the tunnelling rates $\Gamma_S$, and $\Gamma_T$. (a), Position of energy level, $\varepsilon_0$, and (b) tunnelling rates $\Gamma_S$ (circles) and $\Gamma_T$ (triangles), as a function of tip position. (c), I-V curves obtained from the one-level model (coloured curves) superposed on the experimental curves (gray curves). The coloured symbols in a, b correspond to the coloured curves in c.

## 4.3 Recipe for Molecular Diode

From the above investigation, it is found that the rectification mechanism described in this work is due to two factors: (1) Asymmetrical coupling between molecule and electrodes , $\Gamma_T < \Gamma_S$ , and (2) an asymmetry in the electronic structure of the molecule. We can also identify the conditions for the simultaneous optimization of rectification and current density. To have a current

steep onset, the coupling of the molecule to the substrate must be small to avoid level broadening, i.e., $\Gamma_S << |\varepsilon_0|$. On the other hand, the coupling to the tip should be smaller than the coupling to the substrate but not be too small since that would reduce the current. Thus, ideally a molecular diode should work in the regime, $\Gamma_T < \Gamma_S << |\varepsilon_0|$with $\Gamma_T$ as large as possible. This implies that the metal-molecule coupling must be moderately asymmetric. In the present case, this coupling is expected to take place between the LUMO of the POM and the metallic substrate. Since the LUMO is essentially localized on the metal ions [85] its coupling with the substrate is expected to be relatively low, thus preventing level broadening. This ideal situation contrasts with that of fullerene derivatives, as these are $\pi$-conjugated molecules with accessible p-orbitals at their surfaces, which favors a larger coupling with the substrate.[86]

## 4.4 Difference between $C_{60}$ and DyW30

The One level model was used to explain the rectification in DyW30 and $C_{60}$. Even though, the one level model is cannot be perfectly applied to the $C_{60}$ molecule. The HOMO and LUMO levels of $C_{60}$ are close the Fermi-level, and contribute to the electronic transport through the molecule. We have to take these factors into account while calculating the transport properties. Since both the level contributes to the transport there will the current in the both polarities, and that reduces the asymmetry in IV spectra. This in-turn results in reduction of the rectification ratio in the case of $C_{60}$ even in the case of an asymmetric electrode coupling. In the case of DyW30, only one level is contributing to the transport and yields high rectifications. The other levels are either far from the Fermi level or less coupled to the electrodes. That makes the DyW30 an ideal candidate for one level model. This property of DyW30 combined with asymmetric coupling results in high rectification ratio.

## 4.5 Conclusion

In this chapter, we studied the rectification of a polyoxometalate molecule (DyW30) and fullerene ($C_{60}$) in the molecular junction using a scanning tunneling microscope. We observed that DyW30 single-molecule junctions shows large rectification ratios ( >100) and sustains high current densities ( $> 10^5\ A/cm^2$). This system provides the possibility of scaling down the diodes to nanometer dimensions. Reduction in the size is around $10^7$ in comparison with first Fleming diode ( Figure 3.1). By investigating the changes in the I-V curves with the tip-molecule displacement, we showed that the rectification is arising from the asymmetric coupling of the molecule with an asymmetric molecular level. Mechanism for rectification was explained based on the single level model. This was further verified by studying the rectification in $C_{60}$ molecule and evolution of rectification with respect to electrode coupling. These examples indicate that this mechanism of rectification is universal, and can applied to both inorganic and organic molecules. This result throws light on the rectification in molecular diodes and hence will help in the design and development of fture nanoscale rectifiers.

# Part III

# Single Molecule Magnets

# Chapter 5

# Review of Single Molecule Magnet

One of the goals of this thesis is to investigate the magnetism in the Single Molecule Magnets (SMM) by electronic transport measurements. A brief introduction to Single Molecule Magnets is given in this chapter. The first section gives an account on the historical development and theory of the Single Molecule Magnets. In the second section, a brief review on experimental techniques used to probe SMMs by electrical measurements is given.

## 5.1 Magnetism

Magnetism is one of the oldest phenomenon known to the human civilisation. Chinese were the first to make a practical use of this phenomenon. They used magnetic compass made from the lodestone for navigation [87, 88]. In middle ages, many practical applications of magnetic materials were invented. However, the explanations for the science behind magnetism was mostly metaphysical [88].

The first attempt to describe magnetism based on experimental results was done by William Gilbert [89]. In 1819, Hans Christian Oersted observed that an electric current could influence a compass needle. Following this observation, Jean-Baptiste Biot and Félix Savart quantified this effect by proposing an equation for the magnetic field generated by the current-carrying wire. Few years later Michael Faraday reported the converse effect, time-varying magnetic flux through a loop of wire can induce a current. Further studies revealed the relation between electricity and magnetism. circa 1906, J. J. Thomson discovered the electrons [90]. During the same period James Clerk Maxwell unified electricity and magnetism through Maxwell equations. Even then, the actual mechanism behind ferromagnetism remained a mystery. Then Pierre Weiss proposed a molecular field theory to explain ferromagnetism. Later, the discovery of the electron's spin by George Uhlenbeck and Samuel Goudsmit revealed the intrinsic angular moment of electron [91]. These discoveries played a vital role in developing a theory for magnetism observed in various materials.

Nowadays, the magnetic materials are used in a wide variety of application such as computers, telecommunications devices, medical imaging system, electric generators, motors. Especially, the ferromagnetic devices are an essential part of the electronic industry. Last quarter of the 20th century witnessed a drive in the research for miniaturisation of devices for improving the computational power. Following this trend, there were tremendous efforts to make miniature magnets as well. However, the miniaturization of the magnets below certain size is not possible.

One approach to overcome the size limitation is by using functionalized molecules that can perform roles of the electronic devices, i.e., molecular electronics [92]. Another approach is to exploit the spin of the electron. The devices utilising the spin degree of freedom are called the spintronic devices [93]. Molecular-Spintronics is the combination of spintronics and molecular electronics [94]. Single molecules magnets are promising candidates for molecular-spintronics.

### 5.1.1 Size Limit and Super-paramagnetism

As mentioned in the previous section, one of the main challenges in the electronic industry is to make miniaturised magnets. The minimum size one can attain is a single magnetic domain nano-particle. The direction of magnetisation in a microscopic ferromagnetic domain is typically aligned along its easy axes. Due to the magnetic anisotropy of the particle, the magnetic moment has two stable positions that are separated by an energy barrier, E and antiparallel to each other as indicated in figure 5.1.

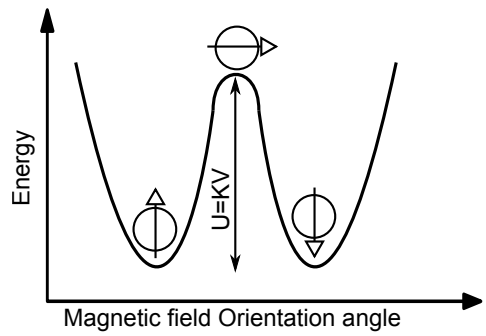


FIGURE 5.1: Anisotropic energy barrier of a super-paramagnetic particle.

The particle has the lowest energy when its magnetic moment is parallel or anti-parallel to the easy axis (As shown in the figure 5.1). Meanwhile, the magnetisation perpendicular to the easy axis has higher energy. The energy barrier (U) separating the low energy configurations is proportional to the volume (V) of the particle, and is given by the formula $U = KV$, where $K$ is the magnetocrystalline anisotropy constant of the particle. At low temperature, the particle will be in one of the lower energy configurations. When the size of the particle is lesser than 10 nm, the energy barrier is comparable to the thermal energy, $k_BT$ and this thermal energy sufficient to flip the lower energy configurations.

Néel proposed that the time required for flipping of the magnetisation between the two configurations follows an Arrhenius behaviour and can be expressed by [95]

$$\tau = \tau_0 exp\left(\frac{U}{k_B T}\right) \tag{5.1}$$

where $k_B$ is the Boltzmann constant, and T is the temperature. The blocking temperature is characterised by the temperature at which the relaxation time is equal to the time of the measurement. This criterion sets the limit for the thermal stability of the ferromagnetic material as a memory device, and is typically referred as super-paramagnetic limit [9]. For the stability of a magnetic bit for practical operation the blocking temperature of the particle should be of the range of room temperature.

### 5.1.2 Single Molecule Magnet

Single Molecule Magnets are molecules that show slow relaxation of the magnetic moment at low-temperature [28, 96]. These molecules are usually coordination complexes with one or more metallic ions. Magnetism in these systems are due to the high-spin ground state of the molecules. These molecules are smaller compared to the single domain magnetic nanoparticle. Single Molecule Magnet behaviour in a molecular system was first observed by R. Sessoli *et al.* in $[Mn_{12}O_{12}(OAc)16(H_2O)_4]$ (usually abbreviated as Mn12Ac) [97, 98]. Figure 5.2a shows crystal structure of Mn12Ac.

This molecule has 4 $Mn^{IV}$ ions in the inner core forming a tetrahedron and 8 $Mn^{III}$ ions forming an outer octahedron ring. These Mn atoms are interconnected by oxide ions. $Mn^{IV}$ has a magnetic spin of 2, and $Mn^{III}$ has a magnetic spin of 3/2. Mn atoms in the same oxidation state is linked by Super-exchange coupling through oxygen. Meanwhile the $Mn^{III}$ and $Mn^{IV}$ are coupled electromagnetically. This lead to a total ground spin state of 10

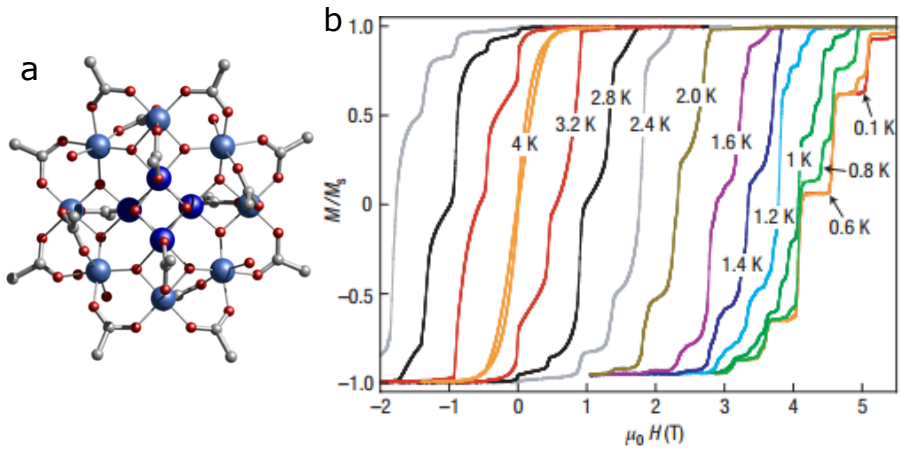


FIGURE 5.2: (a) Crystal structure of $[Mn_{12}O_{12}(OAc)16(H_2O)_4]$, Colour code: $Mn^{IV}$ - dark blue, $Mn^{III}$ - blue, Oxygen - red, Carbon- grey. [100] (b) Hysteresis loops of single crystals of Mn12Ac SMM at different temperatures. Hysteresis loops exhibit a series of steps due to resonant quantum tunnelling between energy levels[28]

$(8\times 2-4\times\frac{3}{2}=10)$. This molecule has a uni-axial anisotropy due to the Jahn-Teller distortion[1]. This uniaxial easy-axis anisotropy combined with a small transverse anisotropy produces a potential barrier separating the spin-up and spin-down states. The large spin ground state arising from the intramolecular exchange interactions and magneto-anisotropy results in SMM behaviour in the molecule [99]. The system behaves like a superparamagnetic particle. These molecules also shows the Arrhenius behaviour (as expressed by Equation 5.1) for temperature effects. J. R. Friedman *et al.* verified the magnetism in SMM by conducting the magnetic hysteresis studies on crystalline Mn12Ac [101]. Apart from thermal relaxation, SMMs can also relax magnetisation by the quantum tunnelling of spin states. This coherent process is known as the quantum tunnelling of magnetisation (QTM). Friedman *el al.* also observed the QTM during magnetic hysteresis measurements.

[1]Jahn–Teller effect: A system with a single electron (or hole) in a degenerate level will tend to lower their energy by distorting the crystal environment [9].

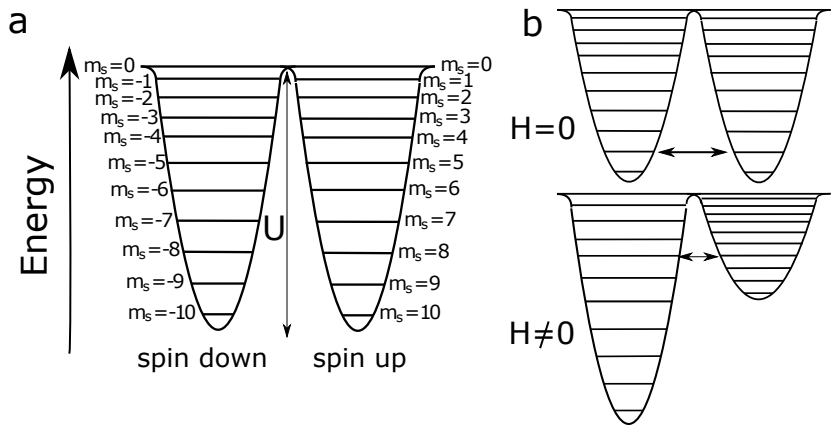


FIGURE 5.3: Schematic representation of the double-well potential of a MnAc. The vertical line shows splitting of the S = 10 ground state to 21 states(2S+1). (b) The scheme shows changes in the energy level diagram for a non-zero field H $\neq$ 0. Resonant magnetisation of tunnelling takes place when the levels are matched

The Hamiltonian for a spin-system with spin S and uni-axial anisotropy, in the absence of an external magnetic field, can be expressed by [88],

$$\mathcal{H} = -DS_z^2 \tag{5.2}$$

where, $D$ is the zero-field splitting parameter ($D > 0$)and $S_z$ is the component of spin(S). The lowest energy states of the system is then given by $m = \pm S$. The height of the barrier is $U = -DS^2$, for integer spin and $U = -D(S^2 - 1/4)$, for half-integer spin. Figure 5.3a shows the example of the double well potential in the case of Mn12 SMM where S=10. When a magnetic field applied to an anisotropic spin system in the z direction, the levels of the double-well potential shifts. The Hamiltonian Eqn 5.2 in presence of a magnetic field, $H$ takes the form

$$\mathcal{H} = -DS_z^2 + g\mu_B HS_z \tag{5.3}$$

Here $\mu_B$ is the Bohr magneton and g is the Lande tensor. This applied field leads to a degeneracy of the levels with $\pm m$. The levels with m $<$ 0 shows an increase in energy and those with m $>$ 0 decrease in energy. At a certain field,

the levels on both side matches and tunnelling occurs between these matched levels. This crossing occurs at $H_z = nD/g\mu_B$, with n=0,1,2,3, etc. Schematics showing Resonant Tunnelling of Magnetisation is showed in Figure 5.3b. Thus, the QTM opens an additional channel for the relaxation of magnetisation and results in the occurrence of characteristic steps in the magnetic hysteresis loops of SMMs. The step positions are related to the QTM levels (see Figure 5.3). This result shows that the SMMs can act as a magnetic particle exhibiting magnetic hysteresis loops similar to magnets and show slow magnetic relaxation below their blocking temperatures. For this reason, SMMs are considered as promising candidates for the applications such as quantum computing, high-density magnetic data storage, etc.

### 5.1.3 Single-ion Single Molecule Magnet

The first studies on molecular magnets were based on molecules with many ions. Recently, another class of Molecular Magnets called single-ion single molecule magnet, in which there is only one magnetic ion inside the molecule, were synthesized. The f-shell elements are typically used as the magnetic ion in these systems. The first of single ion SMM was synthesised by Ishikawa *et al.* in 2003 [102]. This compound was a bis-phthalocyanine complex in which a Tb ion is sandwiched between two phthalocyanine blocks.

In this complex, magnetic anisotropy arises from the splitting of the J ground state of the Lanthanide(3+), ($Ln^{III}$) subjected to the crystal field (CF) of the molecule, which results in splitting of ($Ln^{III}$) with large $|M_J|$. Another group of molecule used obtain single -ion SMM are polyoxometalates. First polyoxometalate based single ion SMM, $[ErW_{10}O_{36}]^{9-}$, was synthesized by Al Damen *et al.* in 2008 and has similar crystal field symmetry parameters of bis-phthalocyanine [35].

### 5.1.4 Single ion Lanthanide in Molecule

Lanthanides (Ln) are elements occupying 4f block of the periodic table. Electronic configuration of a lanthanide group element is $[Xe]6s^2 4f^n$, where [Xe] represents the configuration of Xenon. The most common oxidation state of a Lanthanide is 3+, ($Ln^{III}$) which is attained by losing two 6s and one 4f electron. Electronic configuration of $Ln^{III}$ ion is $[Xe]4f^{n-1}$. In Lanthanides, 5d electrons shield 4f electrons. The rules for obtaining a ground state multiplet of the $Ln^{III}$ ion is determined by Hund's rule [103, 104]. The rules are:

1. *The largest spin multiplicity :* The term with maximum S lies lowest in energy ($\Sigma_i m_{s,i} = M_S \rightarrow S$) ,where $m_s$ is quantum number corresponding to the projection of values of S
2. *The largest orbital multiplicity :* For a given spin multiplicity, the term with highest L lies lowest in energy ($\Sigma_i m_{l,i} = M_L \rightarrow L$), where $m_l$ is quantum number corresponding to the projection of values of L
3. *Hund's third rule :* For less than half-filled sub shells ($n \leq 2l+1$), the level with the lowest value of J lies lowest ($J = |L - S|$). For a sub-shell is more than half full ($n > 2l+1$), the highest J lies lowest, i.e. ($J = |L + S|$).

The forces that act on 4f electrons in a free Ln ions are - nuclear attraction, inter-electronic repulsion and spin-orbit coupling. In this case, Hamiltonian can be written as

$$\mathcal{H}_{ion} = \underbrace{\sum_{i=1}^{n}\left(-\frac{Z'}{r_i} - \frac{1}{2}\Delta_i\right) + \sum_{i\neq j}^{n}\frac{1}{r_{ij}}}_{\mathcal{H}_0} + \underbrace{\lambda.\vec{L}.\vec{S}}_{\mathcal{H}_{SO}} \tag{5.4}$$

The first term in $\mathcal{H}_0$, represent Hamiltonian for a multi-electron system with n f-shell electrons in the presence of screened nucleus charge $Z'$. Second term, in $\mathcal{H}_0$ represents repulsions between electrons. $\mathcal{H}_{SO}$ is Spin-Orbit Interaction term. $\lambda$, Spin-Orbit coupling constant, is positive for less than half fill and

negative for more than half filled shells. Due to the spin- orbit interaction, energy levels further split into ${}^{2S+1}\Gamma_J$ levels each with a multiplicity of (2J + 1) [2].

### 5.1.5 Crystal fields

When an ion is placed in a molecule, the electronic charge distribution $\rho_0(r)$ interacts with the surrounding charges in the crystal through Coulomb interactions, and this interaction is called crystal field interaction. This crystal field interaction results in the quenching of orbital angular momentum and creates single-ion anisotropy. The potential $\phi_{cf}(r)$ produced by the distribution of charge $\rho_0(r')$ outside the ion is given by [9]

$$\phi_{cf}(r) = \int \frac{\rho_0(r')}{4\pi|r - r'|} d^3r' \tag{5.5}$$

The total Hamiltonian in the case of an ion placed in a solid is expressed by.

$$\mathcal{H} = \mathcal{H}_0 + \mathcal{H}_{SO} + \mathcal{H}_{cf} \tag{5.6}$$

This Equation is similar to the Equation 5.4, but with an additional term$\mathcal{H}_{cf}$ (crystal field)

$$\mathcal{H}_{cf} = \int \rho_0(r)\phi_{cf}(r)d^3r \tag{5.7}$$

For a Lanthanoid ion, the crystal field is shielded by the 5d electrons. Hence $\mathcal{H}_{SO}$ is stronger in than $\mathcal{H}_{cf}$ in the case of 4f elements. In the case of d shell ions $\mathcal{H}_{cf}$ is stronger than $\mathcal{H}_{SO}$.

[2]Here ${}^{2S+1}\Gamma_J$ is general notation to represent multiplets. $\Gamma = S, P, D, F....$ corresponds to L = 0,1,2,3,...

The interaction energy $\varepsilon_a$ of a lanthanide ion with electron density $p_{4f}$ in crystal field $\phi_{cf}(r)$ is given by

$$\varepsilon_a = \int e\rho_{4f}(r)\phi_{cf}(r)d^3r \tag{5.8}$$

In the equation 5.8, $\rho_{4f}$ can be expanded using spherical harmonics and expressing the electrostatic interaction in terms of the 2n-pole moments of the $\phi_{cf}$, where n is even. The quadrupole moment term (n=2) can be expressed by

$$Q_2 = \int \rho_{4f}(r)(3cos^2\theta - 1)r^2d^3r. \tag{5.9}$$

The sign of $Q_2$ determines the shape of the 4f electron cloud. When $Q_2 > 0$, it results in prolate, and when $Q_2 < 0$ it results in oblate shape. The higher order terms $Q_4$, $Q_6$, etc determine the charge distribution of the 4f. The crystal field Hamiltonian , $\mathcal{H}_{cf}$ can be expressed in terms of angular momentum operators as [9] .

$$\mathcal{H}_{cf} = \sum_{k,q,i} B_q^k \hat{O}_q^k(i) \tag{5.10}$$

where $\mathrm{B_q^k} = \theta_\mathrm{q} < \mathrm{r_{4f}^n} > \mathrm{A_q^k}$ are ligand field parameters ($\theta_q$ is a constant) and $\hat{O}_q^k$ are Steven's operators. The running number k must be smaller than $2l$ and even, while q from -n to +n. Due to this interaction energy levels splits further. Kramer's theorem states that, if J is half-integral (Kramer ion), crystal field results in obtaining Kramer's doublets $| \pm \mathrm{M_J} >$. If J is integral, then it obtains a $| \pm 0 >$ singlet and other doublets. For the f shell elements, where k=2,4,6 , the equation 5.10 can be expressed as [10]

$$\mathcal{H}_{cf} = \sum_{k=2,4,6} \sum_{q=-k}^{+k} a_k(1-\sigma_k)A_q^k\langle r\rangle\hat{O}_q^k \tag{5.11}$$

where the $a_k$ s are the Stevens coefficients $\alpha, \beta$ *and* $\gamma$ for k = 2, 4, 6 respectively. $\sigma_k$ s in the Equation 5.11 are the Sternheimer shielding parameters of the 4f electronic shell.

The $A_q^k$ are determined by using the following parameter [10]

$$A_q^k = \frac{4\pi}{2k+1} c_{kq} (-1)^q \sum_{i=1}^{N} \frac{Z_i e^2 Y_{k-q(\theta_i,\varphi_i)}}{R_i^{k+1}} \tag{5.12}$$

here $R_i$, $\theta_i$, $\varphi_i$ specifies the polar coordinates of the point charge $Z_i$ representing the $i^{th}$ ligand linked to Lanthanide and $e$ is the charge of electron. The lanthanide is assumed to be positioned at the origin of the coordinates system. $c_{kq}$ is the numerical factor relating spherical harmonics $Y_{k-q}$ and the Stevens operators.

### 5.1.6 External Magnetic Field

External magnetic fields can also interact with spin moments. This interaction results in splitting of degenerate levels. This effect is called Zeeman effect. Zeeman Hamiltonian for the magnetic moment in the presence of a field B can be written as

$$\mathcal{H}_Z = (\mu_B/\hbar)(\hat{L} + 2\hat{S}).B \tag{5.13}$$

where g is the Landé g-factor, $\mu_B = 5.788 \times 10^{-2}$meV/T is the Bohr magneton. Zeeman Splitting of Karmer ion (S=3/2) is shown in Figure 5.4a. Its has four degenerate levels. Meanwhile non-Karmer ion (S=2) has 5 (2S+1) degenerate levels, one singlet $\mid 0 >$ and four other levels.

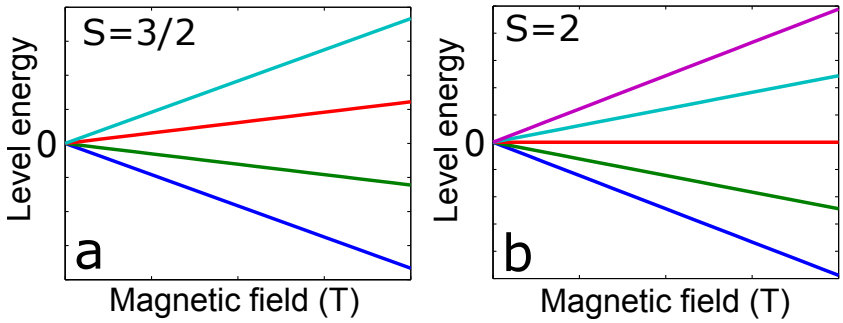


FIGURE 5.4: Zeeman Splitting of (a) Kramer ion (S=3/2) and (b) non-Kramer ion (S=2)

### 5.1.7 Diffrence between d shell and f shell ions

The SMMs are mostly made based on the 3d and 4f shell elements. However, the dominant effect causing magnetic anisotropy in these two groups varies. Table 5.1 show the magnitudes of energy terms in the Hamiltonian (expressed by equation 5.6) for 3d and 4 f ions,

| | $\mathcal{H}_0$ | $\mathcal{H}_{SO}$ | $\mathcal{H}_{CF}$ | $\mathcal{H}_Z$ |
|---|---|---|---|---|
| 3d | $1-5\times10^4$ | $10^2-10^3$ | $10^4-10^5$ | 1 |
| 4f | $1-6\times10^5$ | $1-5\times10^3$ | $\approx 3\times10^2$ | 1 |

TABLE 5.1: The table shows magnitude of relevant magnetic energy terms for 3d and 4 f metal ions (Energy is expressed in K). Zeeman term is calculated for 1 T [9]

For 3d ions, the orbital moments are largely quenched due to the strong crystal field interactions. Meanwhile, 4f ions have larger spin–orbit coupling energy compared to the crystal field splitting that results in unquenched orbital moments, which in turn leads to the high magnetic anisotropy observed in lanthanides.

### 5.1.8 Criteria for f-element single-molecule magnets

In 2011, Rinehart *et al.* identified two essential requirements to be followed while designing f-element single-molecule magnets [105].
*(1) The ground state should be doubly-degenerate and of a high magnitude $m_J$ quantum number.*
*(2) a large separation between the bistable ground $\pm m_J$ state and the first excited $\pm m_J$ state. .*
Double- degeneracy guarantees a bi-stable ground state, which is essential for obtaining SMM. High $m_J$ quantum number helps in maintaining high magnetic state at ground level. The second condition, i.e. the large separation between excited state, ensures slow relaxation of spin.

Rinehart *et al.* also investigated the role of the free-ion electron densities of 4f elements and how it is affected by various ligand configuration. Quadrupole approximation of 4f shell three types of electron density distribution - prolate, oblate and isotropic. Prolate and Oblate have high asymmetry. Molecule holding the ion should be designed in such a way that the crystal field produced by the molecule should increase the anisotropy of the ion. For an oblate ion, ligand electron density should be concentrated above and below the xy plane and for prolate, it should be equatorial.

Dysprosium (Dy) is one of the most used shell element to synthesize SMM. The atomic number of Dy is 66 and the electronic configuration is $[Xe]4f^{10}6s^2$. In the 3+ oxidation state, electronic configuration changes to $[Xe]4f^9$. The Dy(III) ion has an oblate electron density of state. In this case, the ground state electronic configuration can be written as

$Dy^{3+}$ $4f^9$ 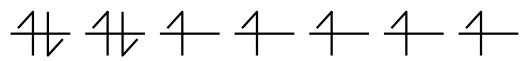

-3 -2 -1 0 +1 +2 +3

$S = 5/2$ $L = 5$ $J = L + S = 15/2$ $^6H_{15/2}$

This scheme yields J =15/2, which is represented by $^6H_{15/2}$. Dy has all the essential qualities proposed by Rinehart *et al.*. (1) It is a Kramer ion, (2) large magnetic moment ground state $^6H_{15/2}$, (3) Its has oblate shape with significant anisotropy. If Dy is placed in a suitable ligand field that increases anisotropy, then it will behave as a SMM. Figure 5.5 shows electronic structure of Dy(III) ion in an ideal crystal field.

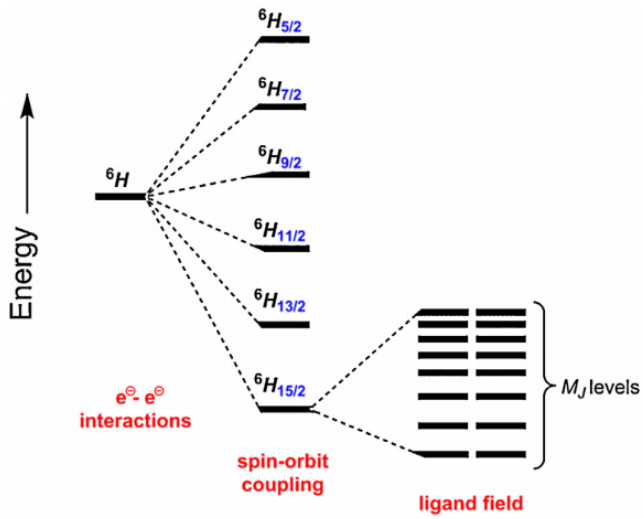


FIGURE 5.5: Low energy electronic structure of the Dy(III) ion with sequential perturbations of electron-electron repulsions, spin-orbit coupling, and the crystal field [106]

## 5.2 Electronic Transport Measurements on SMM

In past ten years, many molecules were reported to show SMM behaviour. Detailed review on these molecules are available in Friedman [107], Craig [108] and Gao [109]. Most of these observations were done by conducting magnetization measurements in powdered samples or single crystals. Electronic transport measurements across the molecule in can be used to probe the spin states of the molecule. These spin dependent experiments of the charge transport at single molecule level is essential for achieving electrical detection and control

on magnetism in SMMs [28]. However, transport experiments on individual SMMs are less explored. To conduct electrical transport studies, the molecules have to be anchored to the electrodes in a controlled manner. The effect of electrodes on the magnetic properties of SMM also need to be investigated.

### 5.2.1 Inelastic Spin FlipTunnelling spectroscopy

In the experimental section (1.1.4), we discussed about inelastic tunnelling spectroscopy (IETS). This section describes the use of IETS to detect magnetism in atoms and SMMs, especially in a STM configuration. Figure 5.6 shows the scheme of Inelastic spin flip tunnelling spectroscopy in the STM set-up. In 2004 Heinrich *et al.* [110] experimentally demonstrated that STM based Inelastic Tunnelling Spectroscopy can be used to probe magnetism of single atom. They observed spin-flip transitions on individual Mn atoms deposited on an ultra-thin insulator islands on a metal surface. At low bias voltages, tunnelling is elastic since the electrons do not have enough energy to excite atoms from lower energy state to higher energy state. An external magnetic field splits the ground levels into Zeeman levels with $\Delta = g\mu_B B$, where g is gyromagnetic ratio, $\mu_B$ is the Bohr magneton and B is the magnetic field.

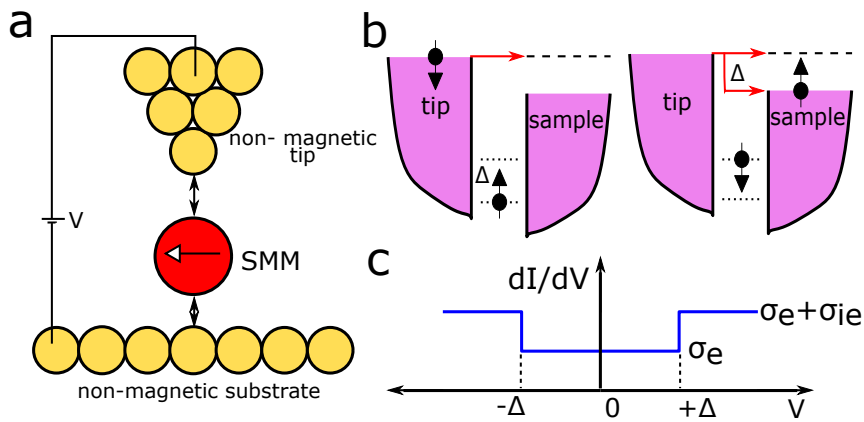


FIGURE 5.6: (a) Scheme of the IETS STM tip and aSingle Molecule magnet on a metal substrate. (b) energy level diagram showing inelastic tunnelling. (c)shows inelastic spectra.

Tunnelling electrons can excite these levels to resulting in spin-flip transition. Tunnelling electrons with an energy greater than $\Delta$ can flip this spin. This spin flip opens up an inelastic channel. Total conductance will be the sum of elastic ($\sigma_e$) and inelastic ($\sigma_{ie}$) terms as indicated in Figure 5.6c. Heinrich et. al. also observed that magnetism in Mn atom is quenched when the atom is placed on the bare metal surface (see Figure 5.7d). This quenching is due to the strong interaction between surface electrons and molecule. To probe spin excitation of atoms, it has to be decoupled the from the electron sea of the metal surface. Ultra-thin insulators such as $Al_2O_3$, MgO, NaCl,$Cu_2N$ , etc. have been used to decouple atom from the metal surface [111]. Another important observation they made is the variation of the gyromagnetic factor with respect to the position of Mn on the insulating island. The $g$ calculate from the slope of $\Delta$ vs $B$ is 1.88 and 2.01 for Mn on the edge of oxide and isolated Mn atom on island respectively. This difference in the $g$ value indicates that the adsorbed magnetic atom is affected by the local interactions. They also observed Kondo effect on the Mn atom located on the bare metal.

Hirjibehedin *etal.* further extended STM based IETS technique to investigate the interaction of individual spins [112]. They made a linear chain of Mn atom on top of $Cu_2N$ (a thin insulating layer) and measured spin excitation by IETS. They observed that the chain shows an anti-ferromagnetic coupling. The even numbered chains shows a spin zero ground state while the odd numbered chains shows a non-zero spin ground state. They also found that the Mn atoms shows different spectra depending on the position (Cu site or N site).

These path-breaking experiments opened up access to a new regime, use of a local probe to investigate and manipulate the spin of individual atoms. Following this experiments spin of different atoms deposited on ultra thin layers were studied. Otte *etal.* [113] studied the spin excitations of a Co atom coupled to a Fe atom and observed that the Kondo peak in the Co atom is affected by coupling of Fe atom.

In all these experiments, thin insulating layer plays a significant role. There have been attempts to measure IETS on atoms deposited on bare metals.

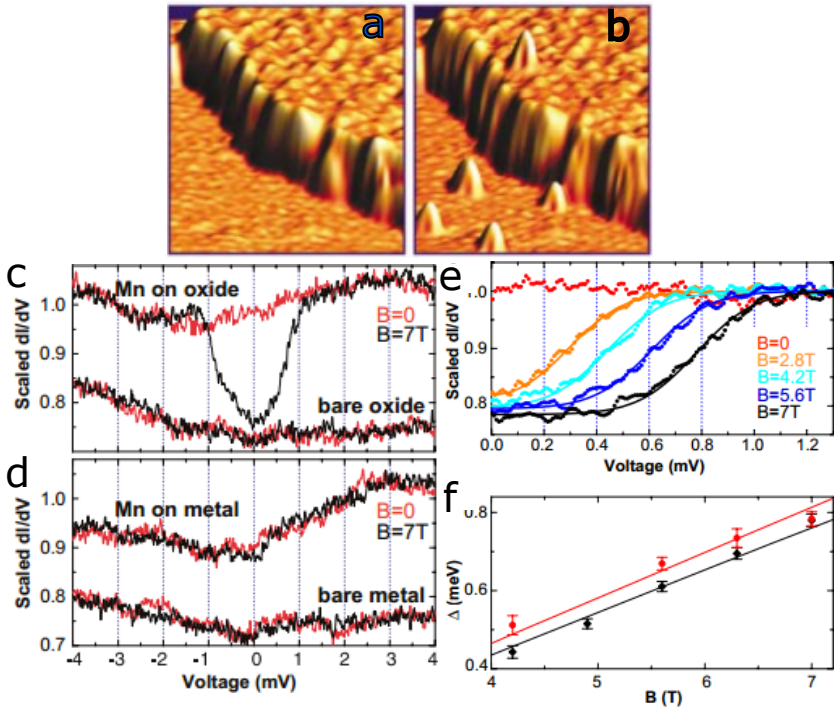


FIGURE 5.7: Spin Flip Spectroscopy on Mn. Comparison of Mn atoms deposited on top of oxide and metal. (a) STM constant-current topography of a NiAl surface partially covered with$Al_2O_3$ (b) Same area after dosing with Mn. (d) Conductance spectra on the Mn atom on oxide measured at B = 7 T (black) and B = 0 T (red). The lower curves were measured over the bare oxide surface. (d) Conductance spectra on a Mn atom on NiAl (upper curves) and the bare NiAl surface (lower curves). (e) Conductance spectra for an isolated Mn atom on oxide at different magnetic fields. Solid lines show fit to the temperature-broadened step model (f) Magnetic field dependence of the Zeeman energy. Black points are obtained from the fits in (e), and red points were taken on a Mn atom located at the edge of an oxide patch. Gyromagnetic ratio g obtained from the linear fits of black and red lines are 1.88 and 2.01 respectively. Figures from Ref [110].

Depositing atoms directly on metal reduces the lifetime of the adsorbate excitation and lead to broadening of the observed spectrum. Due to this reason it is hard to observe spin excitations on atoms on bare metals. However, Balashov *et al.* measured IETS on Fe and Co atom deposited on bare Pt(111) [114]. Another difficulty in these measurements are the low efficiency ($< 2\%$) in producing magnetic excitation by the tunnelling current in the case of Fe

and Co on Pt(111). Due to this problem, Balashov *et al.* interpreted the inelastic part from the second derivative. In 2011, Khajetoorians *et al* succeeded in measuring clear IETS on Fe atom deposited on Cu(111) [115]. These experiments shows that the Inelastic spin-flip spectroscopy serves as an ideal technique to investigate magnetism at nano-scale and can be employed to probe SMMs.

### 5.2.2 Kondo Effect

The Kondo effect is a many body-phenomenon that appears in non-magnetic metals due to the interaction between a local spin and the surrounding conduction electrons [116]. When the temperature of a metal is lowered below the Debye temperature, the phononic contribution due to the conduction electron scattering decreases, and results in a reduction in the resistivity. The resistivity of a metal measured at low temperature saturates at a constant value except for the superconductors. This saturation value is determined by the impurity scattering and defects in the crystal lattice. The situation is different when a magnetic impurity is present in the metal. In the presence of magnetic impurity, the resistivity of metal increases at low temperature [117, 118]. The resistivity vs. temperature curves show a minimum at low temperature (Figure 5.8.a).

This anomaly in resistivity of metals was one of the perplexing problems in physics. The first theoretical model to explain this effect using the perturbation theory was proposed by Jun Kondo, and hence the effect is named after him [119]. He proposed that the increase in resistance at low temperature is due to the scattering of the electrons by the magnetic impurities. At high temperature, the scattering effect of the magnetic impurity on a conduction electron is negligible. The scattering potential caused by the magnetic impurity is small since it flips direction freely. But at low temperature, these magnetic impurities start aligning and starts interacting with the electrons and leads to an anti-ferromagnetic coupling between them. These electrons

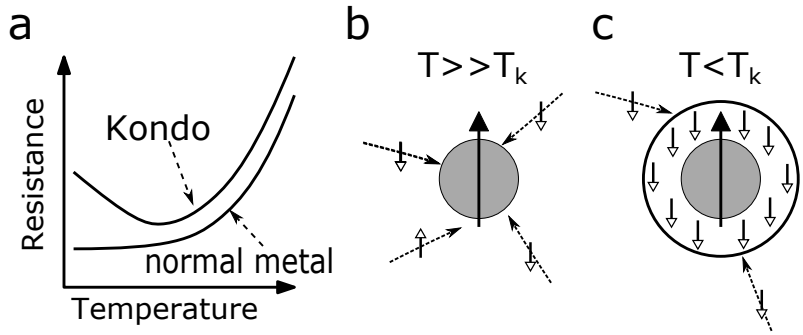


FIGURE 5.8: (a) Resistance of a normal metal decreases as the temperature of a metal is lowered. Metal that is containing magnetic impurities shows an increase in the resistance due to the Kondo effect. (b) and (c) depicts a magnetic impurity in a sea of conduction electrons. (b) The magnetic impurity weakly scatters the conduction electrons at temperatures above the Kondo temperature ($T_k$). (c) At temperatures below Kondo temperature ($T_k$), the conduction electrons are screened by the local spin to form a spin-singlet. The formation of the Kondo screening cloud enhances the effective scattering cross-section of the magnetic impurity.

have a confined wave-function and will not contribute to the charge transport. This results in the increase in the resistivity as observed. However, the model proposed by Kondo was only partially successful in explaining the effect. This is due to the breakdown of perturbation series below a certain critical ratio of interaction strength to temperature, leading to a logarithmic divergence that is not physically feasible. This problem is known as Kondo Problem. This was solved by K. Wilson by applying a renormalization group method to the Anderson impurity model [120]. The temperature at which the Kondo systems show minimum resistivity is called Kondo temperature. The Kondo effect dominates below this temperature. A cloud of conduction electrons formed around magnetic ion collectively screens the magnetic moment of the ion. This enhances the effective scattering cross section of the ion and thereby increasing the resistance (see Figure 5.8c). This spatial extent of the Kondo cloud is called Kondo coherence length.

The advances in nano-fabrication techniques made it possible to probe Kondo effect at the nanoscale. First experimental observation of single magnetic moment at nano-scale was done by Gregory [121]. Goldhaber *et al.* [122]

observed Kondo effect in a single-electron transistor. Following these experiments, Kondo effect was observed in a wide variety of semiconducting heterostructure. In 1998, Madhavan *et al.* [123] and Li *et al.* [124] observed Kondo effect in the magnetic adatoms using STM. This experiments opened up a new test ground for Kondo system.

These Kondo systems can be described by evoking Anderson single level impurity model. In this model, the magnetic impurity is considered as a one level system with an unpaired electron at the energy level $\varepsilon_0$. An unpaired electron with the spin $\frac{1}{2}$ is present at this level. According to the classical physics, an electron in this system cannot come out of this level. However, quantum mechanically it is possible to do that by the exchange mechanism. The uncertainty principle allows the electron in the level to jump to an external electrode for a time scale of $\frac{\hbar}{|\varepsilon_0|}$ [116]. Meanwhile, another electron from the left electrode jumps to the level (Figure 5.9.c). The spin of an incoming electron may be either spin-up or spin-down. Hence, the final state is a coherent superposition state of these two events. Many such events take place, and its combined results lead to the Kondo effect. Due to these processes, an extra resonance level emerges at the Fermi energy (Figure 5.9.d) and is called Kondo Resonance. In the single-molecule device, the electron transport is mainly by tunnelling through a single magnetic site in the junction. In this case, the scattering couples states the external electrodes and thereby results in an increase in conductance. This is in contrast with that observed in the bulk systems [116, 125].

As mentioned above, the Kondo effect appears due to the coupling of the degenerate local state to electrodes (electron reservoirs). Anderson Hamiltonian for describing the system can be written as

$$H = \sum_{\kappa\sigma} \varepsilon_\kappa c^\dagger_{\kappa\sigma} c_{\kappa\sigma} + \sum_\sigma \varepsilon_\sigma d^\dagger_\sigma d_\sigma + U n_{d\uparrow} n_{d\downarrow} + \sum_{\kappa\sigma} \left( \nu_\kappa d^\dagger_\sigma c_{\kappa\sigma} + \nu^*_\kappa c^\dagger_{\kappa\sigma} d_\sigma \right) \quad (5.14)$$

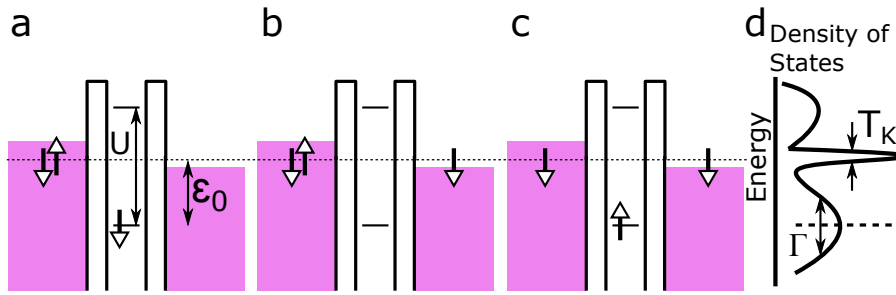


FIGURE 5.9: Scheme shows Kondo transport mechanism a) initial state, b) virtual state c) final state.(d) the resulting density of states

The first term in the equation accounts for the electrons in the electrodes, where $\kappa$ and $\sigma$ represents momentum and spin respectively. The second term describes the localized electrons in the single spin-degenerate state. The third term accounts for the Coulomb interactions among localized electrons. The last term deals with the tunnelling between the dot and the electrodes, with a strength of $\nu_\kappa$. By conducting some transformations and approximation on Equation 5.14, we can obtain Kondo Hamiltonian for a singly occupied state in the system [125]. Then the Kondo Hamiltonian, $H_k$ can be written as

$$H_k = H_{cond} + H_{int} \tag{5.15}$$

where the first term deals with the conduction part. The second term deals with the interaction between the conduction electron and quantum dot/-molecule, and this can be approximated as an anti-ferromagnetic coupling,

$$H_{int} = Js_{cond}.S_{moleucle} \tag{5.16}$$

where $S_{molecule}$ is the spin of the quantum dot (or molecule), s is the sum of spin operators of the conduction electrons and J is the strength of the effective spin-spin interaction [125, 126].

The width of the resonance is determined by the characteristic energy scale of the with Kondo state which is given by

$$k_B T_K = \frac{\sqrt{\Gamma U}}{2} \exp\left[\frac{\pi\varepsilon_0(\varepsilon_0 + U)}{\Gamma U}\right] \tag{5.17}$$

where, Γ is the coupling strength, and U is the charging energy, $e^2/C$. The zero bias conductance amplitude observed in the Kondo effect shows a logarithmic temperature dependence. For a Spin - $\frac{1}{2}$ system temperature dependence of the linear conductance can be expressed by an empirical formula [2]

$$G(T) = \frac{G_0}{\left[1 + (2^{1/0.22} - 1)(T/T_K)^2\right]^{0.22}} \tag{5.18}$$

where $G_0 = 2e^2/h$ is the conductance quanta. The situation is different when there are an even number of electrons. For even electron systems S = 0 (spins are paired) and hence, Kondo resonance is not observed in such cases. However, Kondo effect can be induced in quantum dots with an even number of electrons by applying magnetic field [127].

Heinrich *et al.* observed Kondo effect while carrying out IETS measurements on magnetic ad-atoms [110]. They observed the Kondo effect when the ad-atoms were lying on the bare metal surfaces. The Kondo scattering is occurring at zero energy since the incoming and outgoing electrons are not exchanging energy in this process. i.e., Kondo is an elastic Spin-flip process. The IETS taken on adatom on top of thin insulating layer did not show any zero bias feature. Kondo exchange mechanism can influence the spin flip IETS even when no Kondo effect is observed in system [128]. Also, the Kondo temperature is affected by the de-coupling insulating layer [129]. Kondo temperature measured on the magnetic ad-atom on an insulating layer is lower than that of same measured on the magnetic ad-atom on a bare surface.

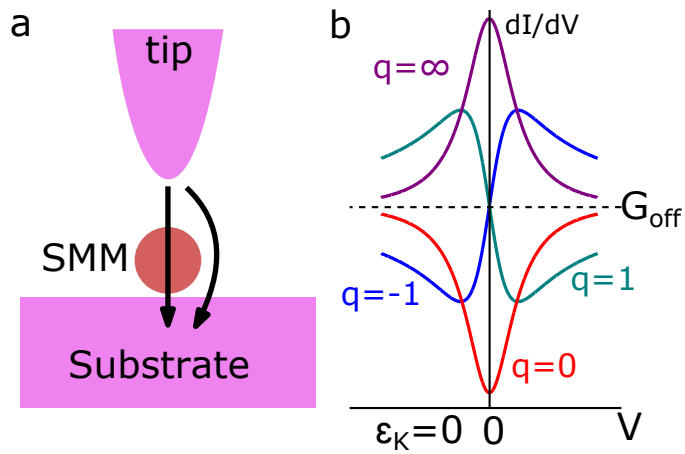


FIGURE 5.10: (a) shows the experimental setup schematically (b)Coloured line shows curves obtained using Fano equation 5.19 for different q values. When q=0, curve shows a Lorentzian dip that corresponds to direct tunnelling, and when q = $\infty$, curve is a Lorentzian peak is obtained which corresponds to inelastic tunnelling. Intermediate values of q result in a tilted S-shaped curve.

In the case of magnetic ad-atom in an STM tunnel junction, there exist two tunnelling channels (Figure 5.10), (1) electrons tunnelling through the Kondo resonance and (2) electrons tunnelling directly to the substrate. In this situation, scanning tunnelling spectroscopy of the Kondo effect observed using STM need not appear as a peak. Instead, it appears as a Fano Resonance [123]. In this situation, the conductance,$G(V)$ can be expressed using Fano formulae [130, 131]

$$G(V) = G_{off} + \frac{A}{(1+q^2)}\frac{(\varepsilon+q)^2}{(\varepsilon^2+1)} \tag{5.19}$$

where $\varepsilon = (eV - \varepsilon_k)/\Gamma$, $G_{off}$ is the conductance offset, A is the amplitude of the Fano resonance, q is Fano factor, $\varepsilon_k$ is the energy position with respect to the Fermi level, and $\Gamma$ is the half-width of the Kondo peak. The Fano factor, q determines the line shape of the resonance. The line shape can take the form of a peak, a dip or an asymmetric shape depending on the values of $q = \infty, 0, \pm 1$. These lines also give information about the hybridization of the

two pathways. The presence of the Fano features in these systems makes the analysis of the Kondo effect complicated.

The Kondo effect has been observed in the SMM systems as well [132–134]. It was also shown that the Kondo effect in the SMM can be manipulated mechanically [133] or chemically [134]. These results show that the observation of the Kondo effect helps to understand the magnetism in SMMs.

### 5.2.3 SMM Spin Valves

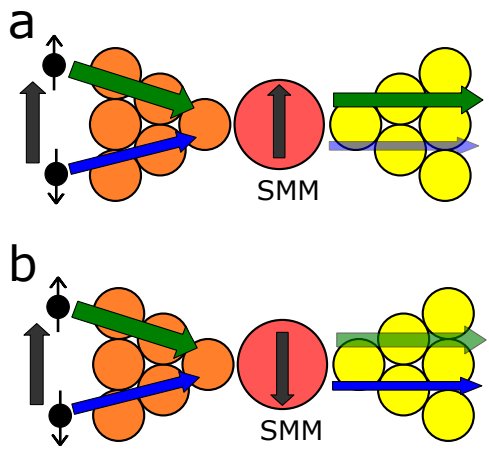


FIGURE 5.11: Figure shows spin valves based on molecular magnets. Grey arrows indicate the magnetisation direction. (a) Shows the spin valve configuration in which the magnetic source electrode (orange) and the molecule is aligned in the same direction. Yellow colour marks the diamagnetic drain electrode. In this configuration, spin-up majority carriers (thick green arrow) are not affected by the molecular magnetization. However, the spin-down minority carriers (thin blue arrow) are partially reflected back. Hence, this configuration has little resistance to current. (b) shows the anti-parallel configuration, the magnetisation of the electrode and molecule are in opposite direction. The majority spin-up electrons are transmitted partially. Meanwhile, minority spin-down electrons pass unaffected. This configuration has a higher resistance with respect to the parallel configuration. Figure from Ref [28]

In addition to the IETS and Kondo effect, Spin-Valve Effect can also be utilised to probe the magnetism in the molecular magnets. The spin-valves are electrical devices that are made out of at least two conducting magnetic elements. Typically ferromagnetic layers are used as the magnetic components. The electrical conductance through these devices varies depending on the relative alignment of magnetisation of the magnetic elements [138]. The Single Molecule Magnet based Spin valve also utilises a similar concept. In this case, one of the electrodes used to contact the SMM is magnetic (see figure 5.11) [28]. When the magnetisation of the electrode is aligned parallel to the spin of the SMM in the molecular junction, then there is an increased current flows through the junction. Conversely, the current in the junction reduces when the spins are aligned anti-parallel. This effect also results in the selective transfer of spin from one electrode to another, and the effect is called giant spin amplification [139]. This phenomenon can also be used to detect the spin state of the SMMs experimentally.

### 5.2.4 Experimental Schemes for SMM

The transport measurements in single molecule magnets are usually done in two configurations, (1) Two terminal method and (2) Three terminal method.

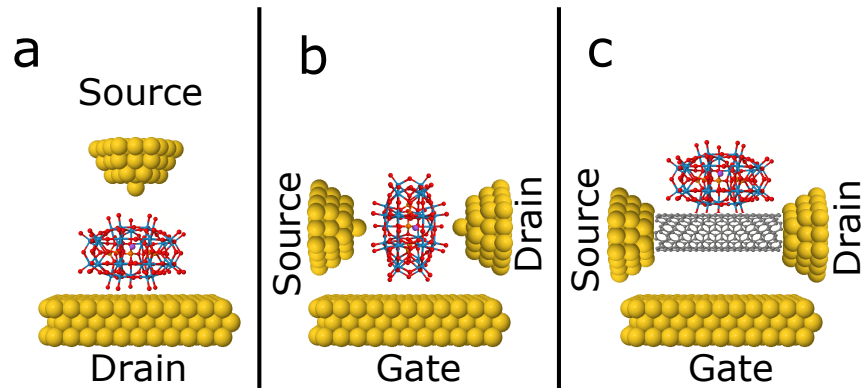


FIGURE 5.12: Schematic shows three ways to measure the electronic transport across the single molecule magnet, (a) Two Terminal method-typically two terminal method is done in STM configurations. The tip of an STM acts as the source and substrate act as the drain electrode. (b) and (c) shows 3 terminal methods. In the three terminal method, there is a third electrode (gate) which is capacitive coupled to the molecule. In (b), the molecule is directly wired to the electrodes, source and drain. Meanwhile, in (c), a carbon nanotube or graphene is directly wired to the electrodes and SMM is attached to this intermediate structure. In this method, the spin is detected by observing the effect of SMM on the current passing through the nanotube/graphene.

*Two terminal method*: In this method, the molecule is directly wired between two electrodes. Commonly, this is done in a STM configuration. The tip and substrate acts as the electrodes. The STM can image the molecule lying on the substrate and detect the adsorption geometry of the molecule. This helps in establishing a precise contact with the molecule. One of the main challenges in this method is to deposit the molecule on the substrate in a precise way. Different methods used for depositing molecules is reviewed in the previous chapter 2. The magnetic properties can be probed by conducting inelastic spin flip (IETS) measurement on an SMM deposited on substrates using STM.

Recently, Kahle *et al.* succeeded in depositing isolated Mn-12 using electrospray deposition method and performed IETS measurements on the molecule [33]. The Figure 5.13 b-c shows the STM image of the molecule deposited on BN/Rh(111). The ultra-thin layer of Boron-Nitride (BN) decouples the molecule from the bare metals. Inelastic spin-flip spectroscopy conducted at 1.5 K shows symmetric steps around the Fermi level revealing the spin-flip transition in the molecule (Figure 5.13 d). Corresponding second derivative shows dips and peaks. They also observed that the magnetism in the Mn-12 molecule is quenched when it is deposited on a bare metal.

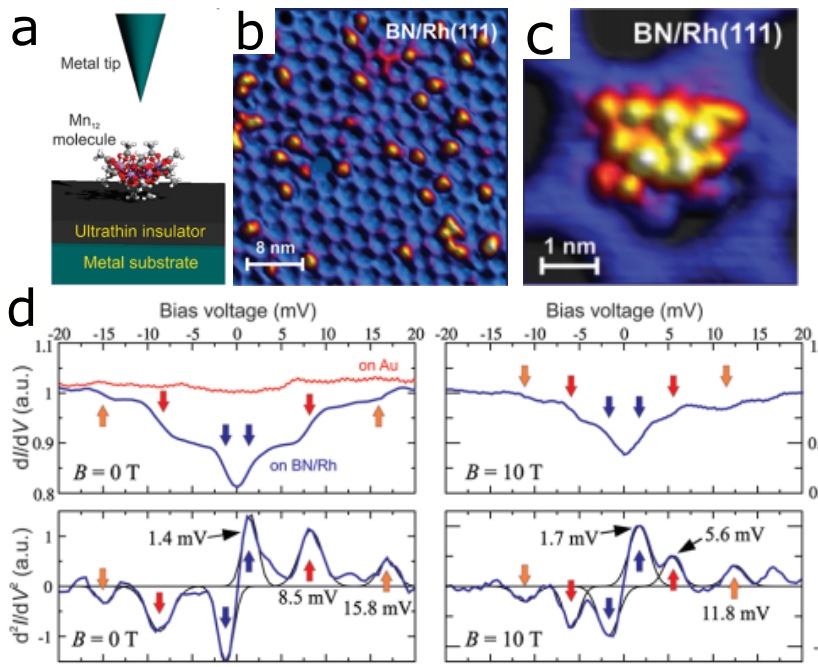


FIGURE 5.13: (a) Shows the scheme of STM measurement of Mn-12 deposited on BN, (b) STM image of the molecules adsorbed on BN/Rh(111) , (c) STM image of an individual molecules adsorbed on BN/Rh(111) and (d) dI/dV spectra and second derivative $d^2I/dV^2$ observed on a Mn-12 molecule adsorbed on BN/Rh(111) surface at B = 0 T (left) and B = 10 T (right). Clear inelastic spin flip steps are visible in the spectra. Meanwhile, Mn12 on Au(111) does not show such features (red line in the top left panel). Image taken from ref [33]

*Three Terminal devices*: The main disadvantage of two terminal devices is

the absence of gate electrode to probe the charge states of the molecule. This problem is solved by placing a third electrode (gate). This three-terminal method can be classified based on the way by which the molecule is linked to the source and drain. In direct connection method, the molecule is directly bound to the source and drain (See Figure 5.12b). The gap between the source and drain should be of the same size of the molecule. These nanogaps are usually prepared by electro-migration [141] or by break-junction technique [142]. These gaps are capacitively connected to the gate electrode. Gate electrode induces an electric field in the gap to probe the redox state of the molecule. Charging of the molecule in the gap affects the magnetic properties of the molecule [94]. Zayazin et. al measured Fe-4 [3] SMM using this method and they observed that the anisotropy as a function of magnetic field [143]. Figure 5.14a shows the scheme of measurement in 3 terminal configurations. In this method, the current and dI/dV of the molecule is recorded as a function of the bias voltage and the gate voltage. The current (or dI/dV) is plotted as a function V (source-drain) and $V_G$ (Gate voltage), which results in a 2D plot (Stability diagram). Figure 5.14b shows stability diagram obtained for the Fe4molecule. Figure 5.14 clearly displays the evolution of the dI/dV spectra with changes in the magnetic field for different redox levels of the molecule. The three-terminal devices prepared by the electromigration techniques are very stable compared to the STM devices, since the electro-migrated devices do not have any moving parts. Depositing the molecules precisely in the nanogap of three-terminal devices is a challenging task. Some experiments use SMMs with particular anchoring groups to attach the molecule to the electrodes. One of the recent advance in the three-terminal devices is the utilisation of the graphene-based electrode as the source and drain [144]. The drawbacks of this method are 1) the inability to quantify the number of molecules in the gap, 2) the inability to determine the stability and orientation of the molecule in the junction. However, these informations can be deduced indirectly by analysing the stability diagram and the evolution of the spectra with respect to the field.

[3] Fe4 - $[Fe_4L_2(dpm)_6]$ (Hdpm) 2,2,6,6-tetramethyl-heptan-3,5-dione

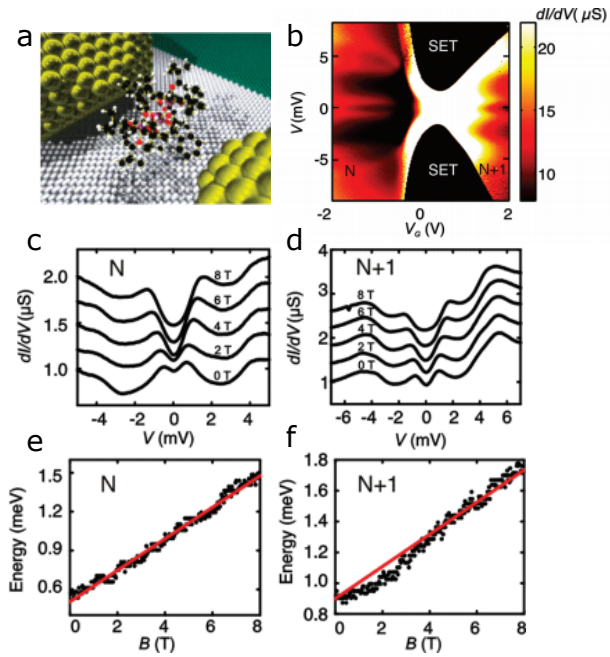


FIGURE 5.14: (a) Scheme of a three-terminal junction with a single Fe4Ph molecule bridging two gold electrodes (yellow) on top of an oxidized aluminum gate (gray) (b) Stability diagram obtained for the molecule in this configuration (c) and (d) are dI/dV as a function of V for $V_G$= -1.5 V and 2 V respectively, various magnetic field values. (e) and (f) are excitation energy as a function of magnetic field for the same $V_G$ values as in (c) and (d). [143]

In the case of the directly linked molecules, the electron transport occurs mainly through the SMM itself, and this might alter the spin state of the molecule. In the indirect three-terminal methods, instead of linking the molecule directly to the electrode, it is coupled to an intermediate structure and the intermediate structure is wired to the electrodes directly. Most of the charge transport takes place through the intermediate structure. Typically carbon-nanotube [145–148] or graphene [149] are used as an intermediate structure. Molecules are connected to the intermediate group by a covalent or non-covalent binding [94]. The spin of the SMM is explored indirectly by measuring the influence of the molecule on the properties of the intermediate structure. The mechanical properties of the carbon nanotubes could be used to probe the spin of SMM by investigating a bis(phthalocyanine)terbium(III)

single-molecule magnet attached to a carbon nanotube [147]. This indirect method also offers the option of attaching more than one SMM to the intermediate part. Urdampilleta *et al.* utilised this possibility to arrange SMMs on carbon-nanotube and fabricated a supra-molecular spin valve [145].

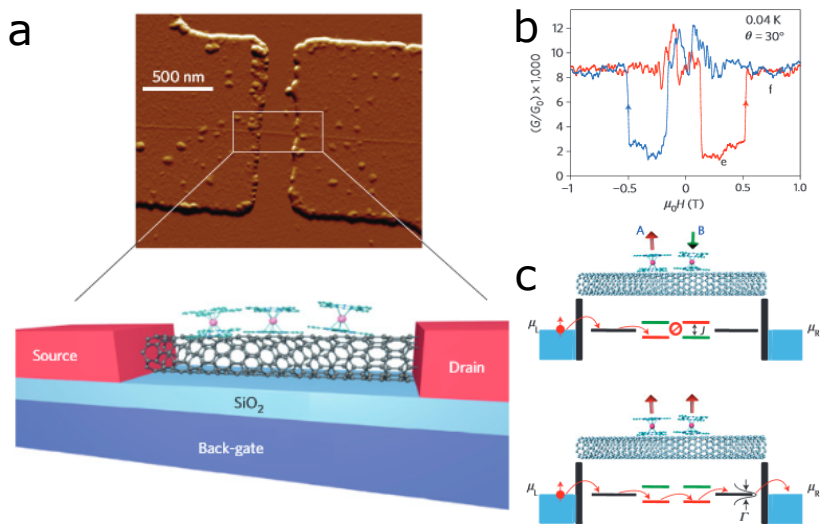


FIGURE 5.15: (a) atomic force image of a supramolecular spin valve. Cartoon displays the detailed scheme of the system. Single-walled nanotube deposited on $SiO_2$ surface is attached to source and drain electrodes. SMMs are coupled to the nanotube. (b) Butterfly hysteresis loop at 40 mK for a nanotube connected to two SMM (c) Shows the scheme of measurements. In an antiparallel spin configuration, the energy mismatch between levels leads to a current blockade and in parallel spin configuration, energy levels of the same spin are aligned and allows passage of current. [145]

.

Figure 5.15 shows the scheme of a supra-molecular spin valve measurement. The localised magnetic moments of the SMMs affects the electrical transport through the carbon- nanotube. At low temperatures, these devices exhibit magnetoresistance. This experiment was the first demonstration of a spintronic valve using molecular [145]. Recently same group used a molecular spin valve to investigate the coupling between a terbium ion and a radical in a single $TbPc_2$ complex [146]. The indirect three-terminal method is one of the fast-developing fields in molecular spintronics.

In the first two methods described above, the molecules are linked directly to the electrodes. Experiments in the direct contact methods can be further classified into two regimes, based on the strength of coupling between molecules and electrodes, 1) *weak coupling* and 2) *strong coupling* [150]. The coupling is defined by the parameter Gamma $\Gamma$, the rate of transfer of charge carrier from the electrodes to the molecular level. The coupling to the left and right electrode can be denoted by $\Gamma_L$ and $\Gamma_R$ respectively. The $\Gamma$ is defined as the sum of $\Gamma_{\mathrm{L}}$ and $\Gamma_R$. In the weak coupling limit, the molecular level remain sharp. Also, the tunnelling electron spends more time in the molecule. If $\Gamma << k_BT$ *and* $\Gamma <<$ coulomb addition energy $(e^2/C)$, then the transport will be dominated by the sequential tunnelling. Coulomb Blockade is observed in this regime. In contrast, in the strong coupling regime, $\Gamma >> e^2/C,\ k_BT$ the levels of the molecule and electrodes are hybridised. In this case, the coherent elastic tunnelling is dominant over the coulomb blockade. Sometimes an intermediate coupling limit existing between these two regimes is also described [2]. In the intermediate regime, higher-order tunnelling processes such as elastic and inelastic co-tunnelling and spin-flip co-tunnelling can occur.

These are the main experimental techniques used for conducting electrical transport measurements in the SMMs. In this thesis, we focus on the STM-based methods to probe the magnetism in the molecules.

# Chapter 6

# Magnetism in DyW30

In this chapter, we investigate magnetic properties of the polyoxometalate based single molecule magnet $K_{12}(DyP_5W_{30}O_{110}).nH_2O$ (DyW30). We experimentally probed the magnetic properties of an isolated molecule by conducting inelastic spin flip spectroscopy at low temperature. The results show that these molecule preserves magnetism when deposited on a metal surface.

## 6.1 Introduction and Motivation

In the previous chapter, the major developments and experimental techniques related to single-molecule magnets (SMMs) were reviewed. The studies on these nanometer-sized SMMs are of great importance due to its quantum effects on magnetic properties and long magnetic relaxation times [28]. Early research on the SMMs was based on polynuclear transition metal complexes [96]. Lately, Ishikawa *et al.* demonstrated that the molecules with mono nuclear Lanthanide ion can behave as SMM [102]. This compound is based on the bis-phthalocyanine complex. Following this discovery, Aldamen et. al. synthesized a new class of single ion SMMs based on Polyoxometalates [35] that are metal-oxide compounds forming arge poly - anion clusters [80, 151].

In single ion molecular magnets, the magnetism is arises from the zero field splitting of gound state (J) of the Lanthanide ion by the crystal field [35]. The crystal field splitting can stabilize sub-levels with a significant $\mid M_J \mid$ value for certain crystal field symmetries and promote an easy axis of the magnetization [152]. Most of the Single ion SMMs are based on the anti-prismatic $D_{4d}$ crystal field symmetry. Recently, Cardona-Serra *et al.* explored the magnetism in a single ion SMM with 5-fold symmetry [4]. They used POM molecule $[LnP_5W_{30}O_{110}]^{12-}$ with $C_5$ axial symmetry and observed that the molecule shows a SMM behaviour for Ln = Dy, Ho.

One of the goals in molecular spintronics is to detect and manipulate the magnetism of an individual single molecule magnet. The POM molecule $[DyP_5W_{30}O_{110}]^{12-}$ is an interesting candidate for studying SMM behavior at single molecule level. The advantage of this POM is that the large non-magnetic framework will provide an effective magnetic isolation between them in the solution and solid state [4]. Magnetic susceptibility and heat capacity measurements carried out on this molecule have confirmed the magnetism in this molecule. However, these measurements were performed on tiny crystals and powdered sample. One of the central question about DyW30 is whether the molecule preserves its structural stability and magnetism when it is deposited directly on a metal surface. We address this issue by probing the magnetism of the molecule on a Au(111) surface by spin-flip spectroscopy using a Low Temperature STM.

## 6.2 Preyssler Anion Based Single ion SMM

Preyssler anion, $[NaP_5W_{30}O_{110}]^{14-}$, is a well known member Polyoxometalate (POM) family. This new molecule is represented by formula $[LnP_5W_{30}O_{110}]^{12-}$ (hereafter LnW30), where Ln is Lanthanide ion in 3+ oxidation state ($Ln^{3+}$ = Tb, Dy, Ho, Er, Tm, and Yb). Figure 6.1 shows the crystal structure of the $[LnP_5W_{30}O_{110}]^{12-}$.

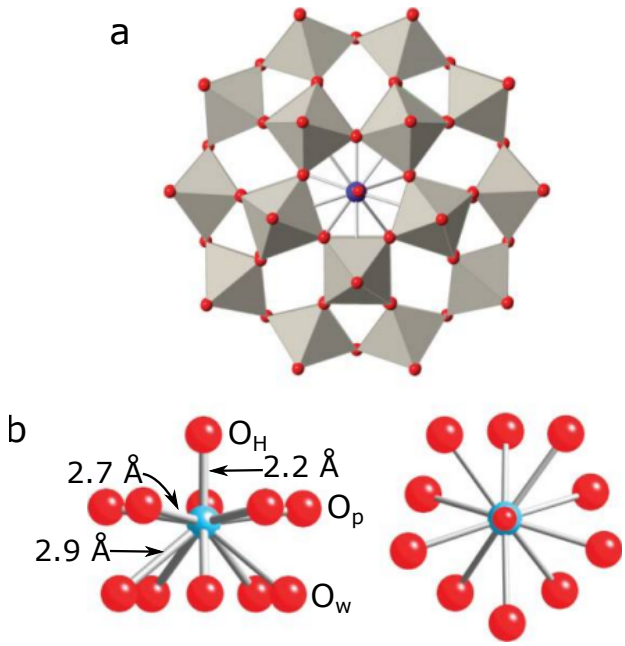


FIGURE 6.1: (a) Crystal structure of Preyssler anion $[LnP_5W_{30}O_{110}]^{12-}$, Ln - Lanthanide. (b) Scheme showing the coordination of the lanthanide ion in a 5-fold environment. (oxygen- Red colour ) $O_P$ - Oxygen atoms linked to Phosphorus and $O_W$ - Oxygen atoms linked to Tungsten. [4]

The molecule posses an Ln ion encapsulated in outer Tungsten-oxide cage. The central ion is linked to the cage by oxygen ions. There are two type of oxygen atoms linking the Lanthanide ion, (1) oxygen atoms that are bound to the phosphorus atom and (2) oxygen atoms that bridging tungsten atoms. The 5 oxygen atoms linked to phosphorous ($O_P$) have a Ln - oxygen bond length of 2.7 Å and are arranged in the corners of a pentagon. Similarly 5 oxygen linked to tungsten ($O_W$) also forms a pentagon (see Figure 6.1. b). In this case Ln - oxygen bond is 2.9 Å. Coordination site in the other side has a water molecule (indicated by $O_H$ in Figure) and has Ln - oxygen bond length of 2.2 Å. The Potassium atoms surrounding the molecule acts as counter cations. Due to pentagonal anti-prism structure, Lanthanide ion in the molecule is subjected to a $C_5$ coordination symmetry. This makes the LnW30 molecules different from the previously reported Single ion SMM such as bis-phthalocyanine, $[ErW_{10}O_{36}]^{9-}$), etc which had a $D_{4d}$ symmetry. The

large POM ligands encapsulating the lanthanoid provides an excellent isolation to the anisotropic Ln3+ ions in the solid state.

The Crystal Field arising due electric fields effects of the ligands around the lanthanoid ion splits the electronic ground state ($J$) free ion into $M_J$ singlets and doublets. In this case, the LnW30 molecule has a $C_5$ symmetry and Crystal Field Hamiltonian of can be written as [4].

$$\hat{H} = \alpha A_2^0 r^2 \hat{O}_2^0 + \beta A_4^0 r^4 \hat{O}_4^0 + \gamma A_6^0 r^6 \hat{O}_6^0 + \gamma A_6^5 r^4 \hat{O}_6^5 \tag{6.1}$$

where $\alpha$, $\beta$ and $\gamma$ are the Stevens constants, $\hat{O}_k^q$ are the operator equivalents expressed as polynomials of the total angular momentum operators. $< r^k >$ is expectation values of the radial factor $r^k$, and $A_k^q$ are ligand shell depended numerical parameter. $A_2^0$ is the prominent term that determines the ground state of the system. In this case of Preyssler ion $C_5$ symmetry in also results in a large off-diagonal anisotropy parameter ( $A_6^5$ in Equation 6.1). This leads to the mixing of magnetic states $\mid J, M_J >$ with different $M_J$. The resulting levels are combinations of various $M_J$ level.

Cardona-Serra et. al. also conducted Magnetic Susceptibility, $\chi_m$ measurements on powdered samples of the DyW30 molecule [4]. They fitted the magnetic susceptibility curves to obtain the crystal field parameters. The plot observed for the Susceptibility is shown in Figure 6.2. The fit for the Crystal Field Hamiltonian, expressed by equation 6.1, is marked in red colour.

In 2003, Ishikawa *et al.* proposed a procedure to find the CF parameters of an isomorphic series of lanthanoid complexes by simultaneous fit of the all $\chi_m T$ values where they assumed that the CF parameters from the$f^8$ to the $f^{13}$ will show a linear variation [153].

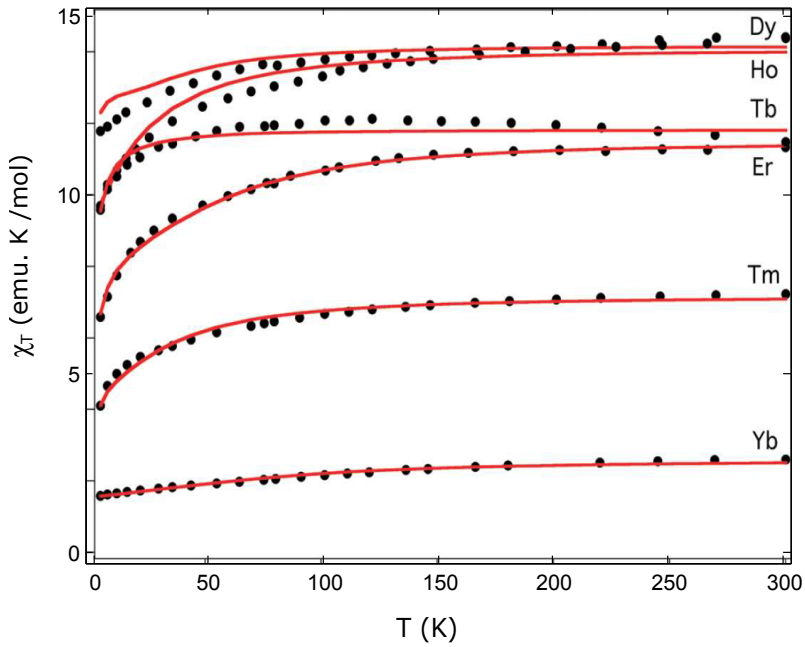


FIGURE 6.2: $\chi_m$T data measured on powdered samples of the LnW30 series under a magnetic field H = 1000 Oe. The red lines are least-squares simultaneous fits of all these curves obtained by the method described above using the CF Hamiltonian. Image from ref [4].

Assuming this condition, the coefficients $A_k^q < r^k >$can be expressed as

$$A_k^q < r^k >= a_k^q + b_k^q(n_f - 7) \tag{6.2}$$

where $n_f$ goes from 8 to 13 when moving from $Tb^{3+}$ to $Yb^{3+}$. Cardona-Serra et. al. used this procedure to obtain crystal field parameters from the magnetic data. Even though, the fit and experimental curves show good agreement for Yb, Tm, Er it shows noticeable deviation in the case of Dy, especially at low temperature.

Unlike the bis-phthalocyanine and other POMs with $D_{4d}$ symmetry, the $A_2^0$ parameter of LnW30, have positive and negative value depending on the lanthanoid metal present in the core. The sign of this term is determined by the

ligand interactions of the different oxygen atoms coordinated with the Ln ion. The interactions of oxygen atom from water molecule ($O_H$) results in a positive $A_2^0$ term. Meanwhile, the oxygen, $O_P$, in the pentagonal plane (also termed as equatorial) results in a negative $A_2^0$ value. The oxygen atoms (marked by $O_W$) are farther away from the Ln ion, and their effect is smaller than the other two types of oxygen atoms. In the case of Tb and Er encapsulated molecule, the cations move deeper between the pentagons and the interactions results in a negative $A_2^0$. This also indicates that the $A_2^0$ becomes more positive when the Ln ion is closer to the $O_H$.

Similar to the $A_2^0$ term, $A_4^0$ term also shows a deviation from the value obtained for $D_{4d}$ complexes. In the $D_{4d}$ anti prism complexes, all ligands are placed equally around magic angle, which leads to a negative $A_4^0$ term. In the case of Preyssler ion complex, the closest ligands could be either axial or equatorial. The value of the $A_4^0$ term depends on the axial water - Ln distance and the equatorial pentagon -Ln distance. Another important point to be noticed is that the reduction of crystal field symmetry from $D_{4d}$ to $C_5$ results in a non-negligible off-diagonal CF parameters $A_6^5$. This term leads to the mixing of different $M_J$ levels. To understand the various allowed transition we calculated energy level scheme for the molecule in the magnetic field using *EASYSPIN* [154, 155]. The J, L, and S of the Lanthanide (III) ions subjected to $C_5$ crystal field are not good quantum numbers. Instead its is a mixture of state, i.e., it is not pure states. It is easily observed that many transition states are possible in this case. Also, Russell–Saunders selection rules are not strictly followed in the case of mixed states. The Table 6.1 ground state multiplets and contribution of mixed states calculated using these CF parameters [4]. This mixing of levels favours tunnelling process which makes it difficult to observe the SMM behaviour.

TABLE 6.1: Energies and modulus of the contribution of each $M_J$ to the wave functions of the ground state multiplets of DyW30. Computed using EasySpin [4, 154]

| Energy $cm^{-1}$ | meV | $\|15/2>$ | $\|13/2>$ | $\|11/2>$ | $\|9/2>$ | $\|7/2>$ | $\|5/2>$ | $\|3/2>$ | $\|1/2>$ | $\|-1/2>$ | $\|-3/2>$ | $\|-5/2>$ | $\|-7/2>$ | $\|-9/2>$ | $\|-11/2>$ | $\|-13/2>$ | $\|-15/2>$ |
|---|---|---|---|---|---|---|---|---|---|---|---|---|---|---|---|---|---|
| 0 | 0 | 0 | 0 | 0 | 0 | 0 | 0 | 0 | 0 | 0 | 0 | 0.22 | 0 | 0 | 0 | 0 | **0.98** |
| 0 | 0 | **0.98** | 0 | 0 | 0 | 0 | 0.22 | 0 | 0 | 0 | 0 | 0 | 0 | 0 | 0 | 0 | 0 |
| 19.483 | 2.4 | 0 | 0 | 0.44 | 0 | 0 | 0 | 0. | **0.85** | 0 | 0 | 0 | 0 | 0.28 | 0 | 0 | 0 |
| 19.483 | 2.4 | 0 | 0 | 0 | 0.28 | 0 | 0 | 0 | 0 | **0.85** | 0 | 0 | 0 | 0 | 0.43 | 0 | 0 |
| 21.000 | 2.6 | 0 | 0 | 0 | 0 | 0.12 | 0 | 0 | 0 | 0 | **0.62** | 0 | 0 | 0 | 0 | 0.78 | 0 |
| 21.000 | 2.6 | 0 | 0.78 | 0 | 0 | 0 | 0 | **0.62** | 0 | 0 | 0 | 0 | 0.12 | 0 | 0 | 0 | 0 |
| 80.159 | 9.9 | 0 | 0 | 0 | 0 | 0.43 | 0 | 0 | 0 | 0 | **0.68** | 0 | 0 | 0 | 0 | 0.60 | 0 |
| 80.159 | 9.9 | 0 | 0.60 | 0 | 0 | 0 | 0 | **0.68** | 0 | 0 | 0 | 0 | 0.43 | 0 | 0 | 0 | 0 |
| 91.710 | 11.4 | 0 | 0 | 0 | 0 | 0 | 0 | 0 | 0 | 0 | 0 | **0.98** | 0 | 0 | 0 | 0 | 0.22 |
| 91.710 | 11.4 | 0.22 | 0 | 0 | 0 | 0 | **0.98** | 0 | 0 | 0 | 0 | 0 | 0 | 0 | 0 | 0 | 0 |
| 98.678 | 12.2 | 0 | 0 | 0 | 0.56 | 0 | 0 | 0 | 0 | 0.23 | 0 | 0 | 0 | 0 | **0.80** | 0 | 0 |
| 98.678 | 12.2 | 0 | 0 | 0 | 0 | **0.80** | 0 | 0 | 0.23 | 0 | 0 | 0 | 0 | 0.56 | 0 | 0 | 0 |
| 115.488 | 14.3 | 0 | 0 | 0.18 | 0 | 0 | 0 | 0.41 | 0 | 0 | 0 | 0 | **0.90** | 0 | 0 | 0 | 0 |
| 115.488 | 14.3 | 0 | 0 | 0 | 0 | **0.90** | 0 | 0 | 0 | 0 | 0.41 | 0 | 0 | 0 | 0 | 0.18 | 0 |
| 129.186 | 16.0 | 0 | 0 | 0 | **0.79** | 0 | 0 | 0 | 0 | 0.47 | 0 | 0 | 0 | 0 | 0.41 | 0 | 0 |
| 129.186 | 16.0 | 0 | 0 | 0.41 | 0 | 0 | 0 | 0 | 0.47 | 0 | 0 | 0 | 0 | **0.79** | 0 | 0 | 0 |

## 6.3 Experimental

We deposited the molecule $K_{12}DyP_5W_{30}O_{110}.nH_2O$ on Au(111) by spray deposition technique as mentioned in the Chapter 2. We used $10^{-8}$ molar solution to obtain a low coverage sample which is essential for probing individual molecule. After deposition of the molecules, the substrate was immediately transferred to the STM. The STM image of substrate is shown in Figure 6.3. The images show that the molecules does not decompose on deposition on a gold surface and can be stably imaged at room temperature. The molecules are found adsorbed on the step edges and terrace of the Au(111) surface. Also, XPS measure conducted on similarly prepared samples confirms the stability of the molecule. We know from the previous results that the molecules are swept by the tip while scanning with negative bias voltages (see Section 4.1.3). This is due to the rectifying nature of the molecule. Since the molecules are swept at voltages $< +1.2$ V, the bias voltage while scanning is set above this value.

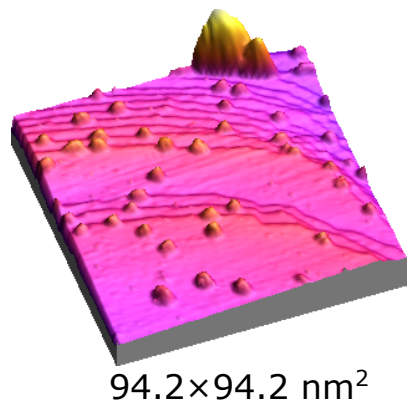


FIGURE 6.3: STM image: Large area scan of DYW30 molecule on gold taken at room temperature. ($V_b = +1.3$ V, $I_t = 0.13$ nA)

After charactering the surface at room temperature, the inner vacuum chamber of cryostat is immediately sealed and cooled down to low temperature. To minimize the effect of sample contamination we employed the clean cooling

procedure while cooling down. Details of this procedure can be found in the section 2.4.

The images were taken after stabilizing the STM at low temperature. Figure 6.4a shows STM image of isolated DyW30 molecules adsorbed on gold surface taken at 350 mK. This images shows that the molecules are stable and immobile at low temperature. Line profile on top of molecule, marked by doted white line in Figure 6.4b, is plotted in Figure 6.4c. Apparent height measured on the molecule at bias voltage of 1.3 V is 0.65 nm.

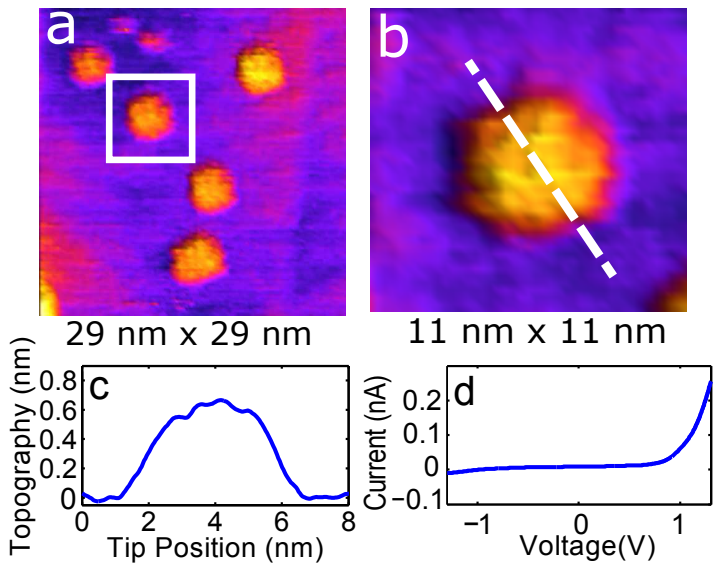


FIGURE 6.4: (a)STM image of DyW30 molecule (V=1.3 V, I = 0.27 nA). (b) zoom in on image (a), indicated by white square (c) topography of the molecule along the line indicated in the (b). Sub-figure (d) shows Scanning Tunnelling Spectroscopy taken on top of molecule

### 6.3.1 IETS on DyW30

After imaging the molecule, we probed the magnetism of the molecule by conducting inelastic spin-flip spectroscopy (IETS). As shown in the Figure 4.9, scanning at low voltage results in sweeping of molecule and we have to apply a

high bias voltage (> 1.2 V) while scanning. We follow the following procedure to conduct IETS on molecule. After imaging and locating an isolated molecule, the STM tip is positioned on top of it. The Current - Voltage ($IV$) curves are taken on the molecule by ramping the bias voltage and recording the resulting current simultaneously. These high voltage $IV$ curves are taken at a conductance of $\approx 10^{-4}G_0$. The high voltage (> 1.2 V) spectroscopy taken on the molecule is shown in 6.4d. The $IV$ curves obtained are highly asymmetric and confirms the rectifying behaviours of DyW30. This IVs also shows that the current at the low bias voltage (±100meV) is negligibly small. Typically, inelastic Spin-flip signals for the magnetic molecules are small, and the magnitude is less than 100 meV. We have to switch the voltage to a low value to conduct the IETS measurements. This voltage switching results in the movement of the tip towards the molecule. The movement of tip depends on the set value of the current in the feedback control. Since the current measured on the molecule is low for small bias voltages, and PID is ON, the tip approaches towards the molecule till a measurable current is observed. Typically, these measurements are done in the range between $10^{-3}$ $G_0$ and $10^{-4}$ $G_0$.

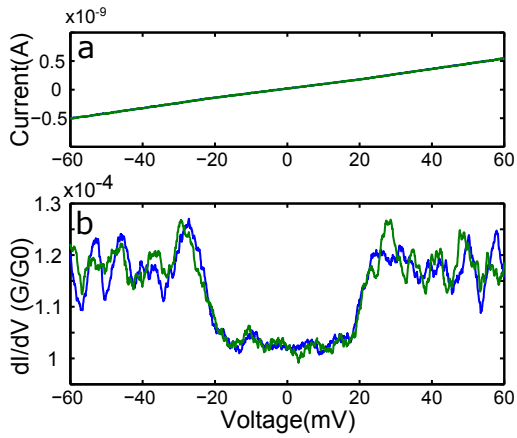


FIGURE 6.5: (a) IV and (b) dI/dV taken on DyW30 on gold surface.

Figure 6.5a shows the average of 4 IETS IVs taken on molecule. The numerical

derivative of the average of these curves gives differential conductance. The differential conductance is shown in Figure 6.5b. The green and blue curves corresponds to the ramp up and ramp down of bias voltage. Typically many voltage ramps are taken at same tip position. Many such sets of $IV$s are taken on the molecule. All these curves were averaged and smoothed to obtain Figure 6.6.

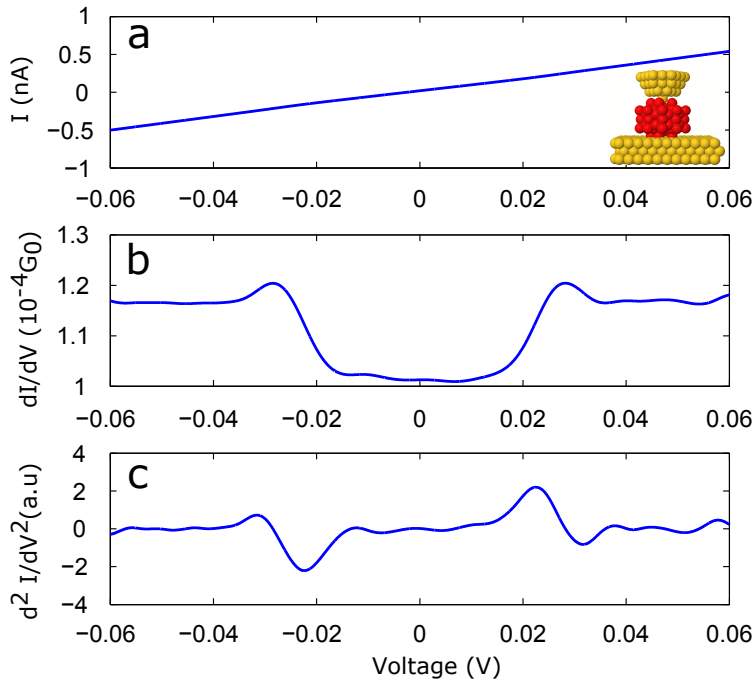


FIGURE 6.6: Figure shows (a) I-V, (b) dI/dV and (c) $d^2I/dV^2$ taken on DyW30 on gold surface. The spectroscopy was taken at bias voltage, $V_b$ = 100 mV and set current, $I$ = 0.5 nA at temperature, T = 350mK. Magnetic field, H = 5 T. Figure (a) inset shows schematic of the tip-molecule-surface configuration. Average of 60 curves

Figure 6.6 shows the filtered inelastic tunnelling spectroscopy measured on a DyW30 molecule taken at 5 T and 350 mK. The spectra show clear steps around 22 mV. $d^2I/dV^2$ (Figure 6.6 c ) obtained numerically helps to assign the position of the step.

The origin of IETS signal in the molecular junction could be due to the vibrational or spin coupling. The electron-vibration couplings are much weaker than electron-spin coupling, and inelastic signals due to vibrational modes are around $1-2\%$ or even lesser [129, 156]. The change in the conductance observed in IETS signal of DyW30 is more than 10 %. This strikes out the possibility of the vibrational coupling and could arise only from the electron-spin couplings. The possibility of the Coulomb Blockade (CB) can also be neglected since the energy of the Coulomb blockade is typically high. It is also worth to note that the IETS signals are not observed in all the molecules measured. One reason could be due to the absence of the Dy in all the molecules. I.e., the sample used in th experiment are not 100 % pure. There are molecules with Na atom instead of Dy atom, and these molecules are non-magnetic. We observe magnetic feature in 31 molecules and at different fields. 10 of them shows IETS signals and the rest of them showed Kondo features.

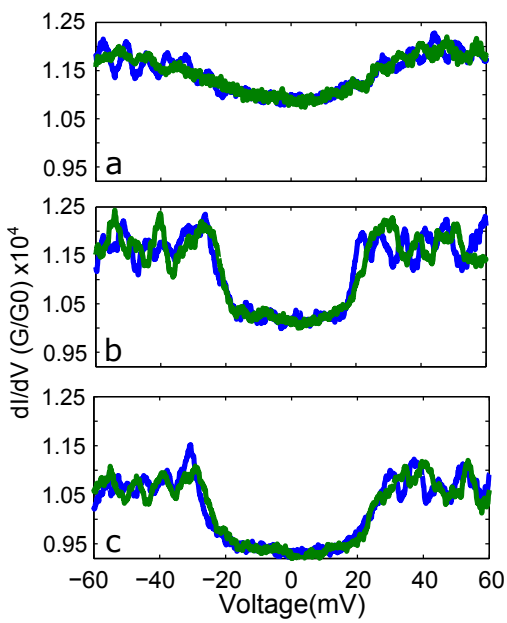


FIGURE 6.7: Figures shows evolution of dI/dV on changing the conductance from $1.15 \times 10^{-4} G_0$ to $1.05 \times 10^{-4} G_0$

We also observe that the IETS varies with the small movement of the tip.

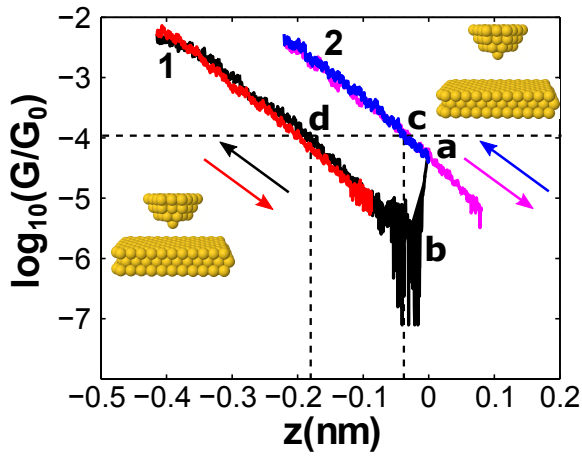


FIGURE 6.8: Figure shows approach and retraction conductance curves for a bare gold tip on clean area. Curve 1 (curve 2) was taken at a low bias voltage 0.1 V (1.3 V). Black and blue colour represents approach curve. Red and Violet colour represents retraction curves

This changes in $dI/dV$s are shown in Figure 6.7. Due to the low conductance of the molecule, the tip has to be approached toward the molecule to measure IETS. Also, the IETS signals measured varies for different conductances. We conducted conductance vs tip-sample displacement ($G - z$) measurements to estimate the distance tip moves during this approach.

At first we measured the Conductance - displacement (G-z) for bare gold. The G-z was taken by positioning the tip on top of a clean gold area and moving tip closer to the substrate after turning off the feedback control loop. Figure 6.8 shows curve G-z taken on gold. The $G - z$ s were taken at two bias voltages, Curve **1** at low bias voltage (0.1 V) and Curve **2** at higher bias voltage (1.3 V). In both case curves shows exponential dependence. The work function calculated from the slope of curves gives similar values, 3.70 eV for curve **1** and 3.65 eV for curve **2**. In the case of curve **1**, initially bias voltage is at a higher value. The feedback loop is turned OFF and voltage is switched to a lower value before approaching the tip towards the surface. This switching results in a steep drop in the conductance ( **a-b** in curve 1). Usually, the conductance drops to limits of measuring range of *current to voltage* (IV)

converter. For this reason there is an increased noise in the low conductance region (Region close to **b**).

The switching of the bias voltage while feedback control is ON results in the displacement of the tip from the initial position. To maintain constant tunnelling current, the feedback controller moves the tip close to the surface. The displacement of the tip during this process can be estimated from the $G-z$ curves in Figure 6.8. Assume that the PID is initially set at a conductance of $10^{-4}\mathrm{G}_0$. For higher bias voltage, 1.3 V, the tip is at a position marked by **c** in Figure 6.8. When a voltage is changed to 0.1 V (with feedback ON), the tip moves towards the surface along **c-d** to the final position d. In this case, the tip displacement (c-d) is 0.15 nm.

After measuring gold, we conducted $G-z$ s on individual DyW30 molecule. An isolated molecule is located by imaging the surface and confirmed by taking STS on top of it. Since the scanning is done at a high voltage, the initial bias voltage is high. Bias voltage is switched to a lower value, 0.1 V, before approaching the tip towards molecule. Figure 6.9 shows typical examples of the approach and retraction curves taken on isolated DyW30 Molecule. As the tip

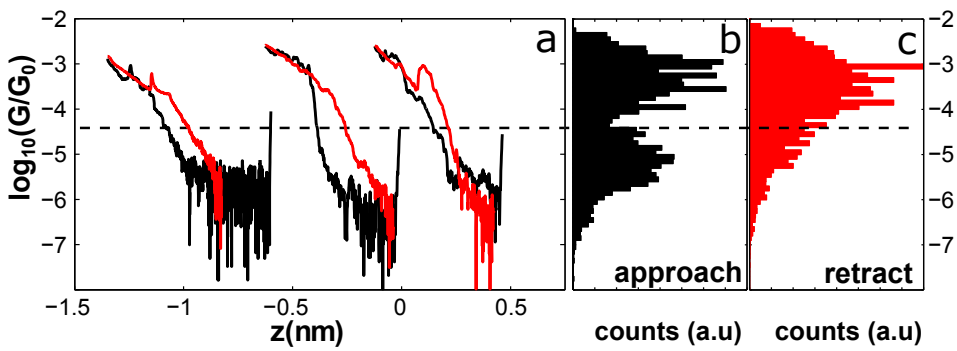


FIGURE 6.9: (a) Shows conductance curves taken on isolated DyW30 molecules after imaging. Black colour indicates the approach curve and red colour indicates retraction curves. ($V_b = 0.1$ V) (b) Shows conductance histogram for the approach curves and (c) shows conductance histogram of the retraction curve.

approaches and makes contact with the molecule, the slope of the conductance curve changes. This change is due to the elastic deformation of the nano-scale metallic contacts. This typically occurs between $10^{-3}$ $G_0$ and $10^{-4}$ $G_0$.The figure 6.9 b,c shows the histogram of approach and retraction curves of 28 G-Z curves. A second peak observed in histogram below conductance, $\sim 10^{-4.5}$ $G_0$ (see figure 6.9 b) is due to the initial jump to the noisy region and hence can be ignored. The distance tip moved before making the contact with the molecule depends on the initial bias voltage. The STS taken on molecule shows steep increase in current for voltages above 1.2 V (see 6.4d). Hence, the movement of tip also varies a lot for small variation in initial bias voltage.

The $G - z$ measurements shows that the tip is already in contact with the molecule while taking $IV$s, i.e. around conductance $10^{-4}$G/G$_0$. We indicate this regime as soft contact. We repeated the IETS measurement on different molecules and for different magnetic fields. Figure 6.10 shows $dI/dV$ and $d^2I/dV^2$ obtained. A large variety of inelastic steps was observed. These signals are sensitive to the tip-molecule configuration geometry. It is important

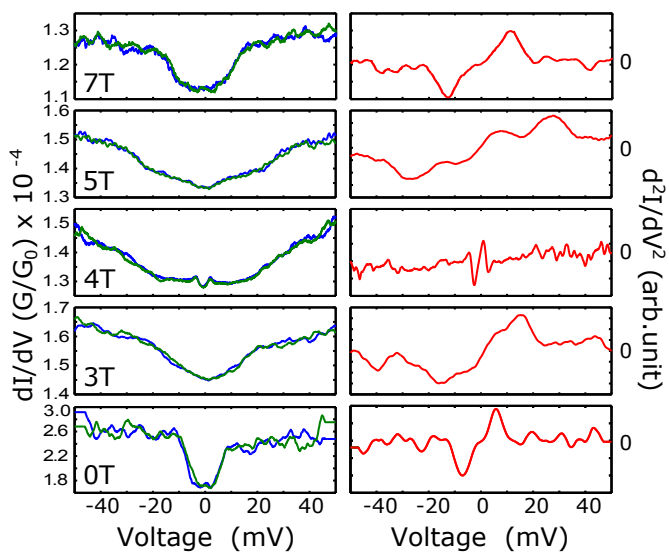


FIGURE 6.10: (a) Shows IVs taken on molecules at different magnetic fields. (b) d$^2$I/dV$^2$ spectra corresponding to dI/dV on (a).

to note that these measurements were carried out in the soft contact with the molecule. Bringing the tip close to the molecule also affect the crystal field anisotropy of the molecule. However, in our case the contact with molecule is unavoidable since the the signal is very weak for lower conductance values.

### 6.3.2 Calculating the Energy Levels

To further investigate link between the IETS signals and magnetism in the DyW30, we calculated the Energy Level diagram of the of the molecule for the applied field. These calculations were done using the *EASYSPIN* software package for Matlab [154]. Figure 6.11 show the Energy Level Diagram for the applied an applied magnetic field. The open circles correspond to the positions where steps are observed on the spectra (see figure 6.10). The jumps are calculated from the ground state. We should keep in mind that for this molecule the $M_J$ s are mixed states. i.e the levels are not pure . Fo this reason, it is difficult to assign the exact transitions. However, the diagram gives some information about the range of energy corresponding to the transitions.

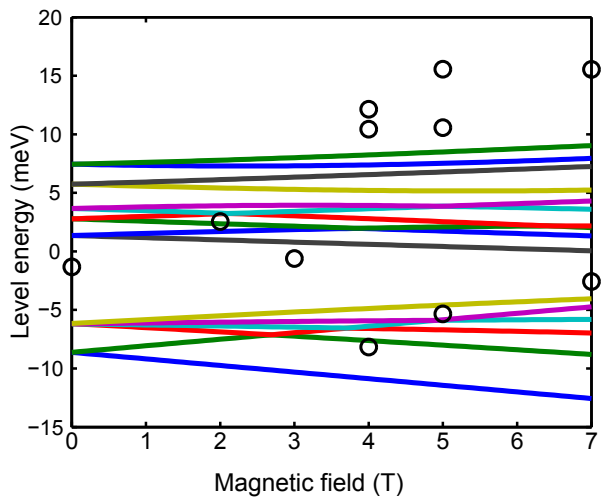


FIGURE 6.11: Energy level diagram of the molecule as function of applied field calculated using EASYSPIN. Black open circles indicates the transition from the lower level measured by inelastic tunnelling spectroscopy.

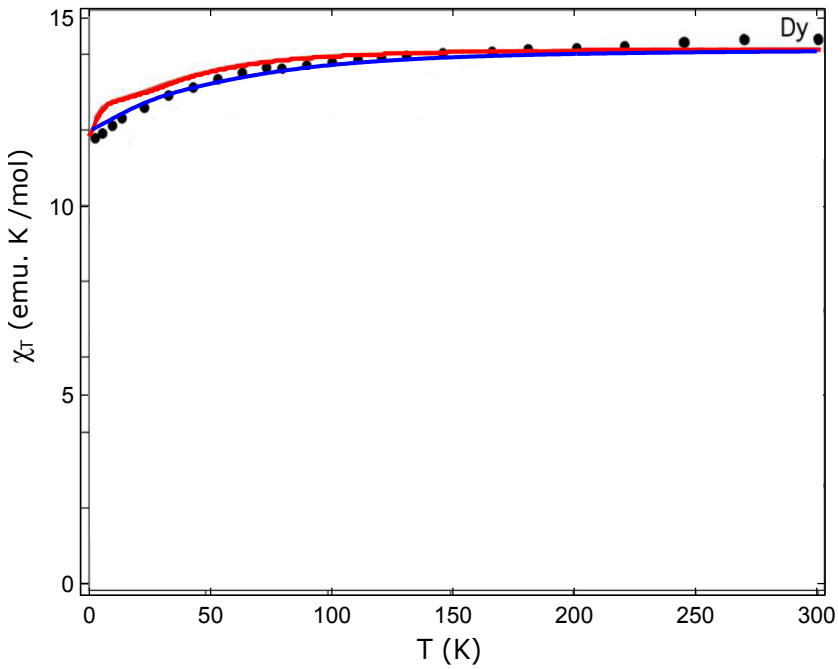


FIGURE 6.12: $\chi_m - T$ data measured on powdered samples of the LnW30 series under a magnetic field H = 1000 Oe. The red lines are least-squares simultaneous fits of all these curves obtained by the method described above using the CF Hamiltonian. Image from ref [4]. The blue line shows the curve obtained by modifying the coefficient of the Stevens constant

The figure 6.11 shows that the transition jumps at the low magnetic field are within the calculated range of the energy level diagram. Most of the observed transitions at magnetic field (H $\geqslant$ 4T) shows considerable deviation from calculated. The CF parameters for simulating the function was taken from the reference [4] which they obtained by fitting the magnetic susceptibility data. This magnetic susceptibility data fitting is shown in the Figure 6.12. The red line indicates curve fit plotted by Cardona et. al. [4]. This red curves clearly shows deflection from the experimental values obtained for susceptibility, especially at low temperature.

To obtain a better fit, we changed the CF parameters. The parameters were obtained from reference [10]. We changed the pre-factor term to the Stevens

Operator and varied it to obtain a better fit for susceptibility - temperature curve. The blue coloured line in the Figure 6.12 shows this modified fitting. The parameters obtained for this fit is shown in the Table 6.2 (Fit2) . The new crystal field parameters thus obtained was used to calculate the energy level diagram of the molecule.

| | $A_2^0 < r^2 >$ | $A_4^0 < r^4 >$ | $A_6^0 < r^6 >$ | $A_6^5 < r^6 >$ |
|---|---|---|---|---|
| Fit 1 | 49.7 | 43.6 | 11.3 | $-1.16 \times 10^3$ |
| Fit 2 | 99.4 | 69.8 | 18.08 | $-0.12 \times 10^3$ |

TABLE 6.2: The table shows CF Parameters for the DyW30 molecule. Fit1 shows the parameters for the red curve. Fit2 shows the same for the modified curve (blue)

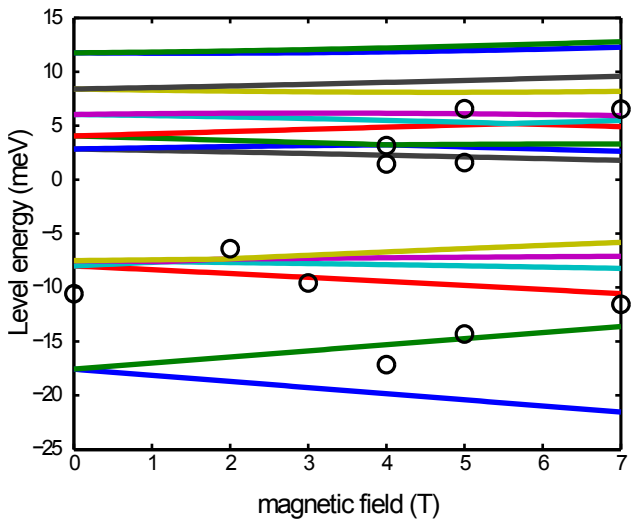


FIGURE 6.13: Modified Energy level diagram of the molecule in field calculated using EASYSPIN. Black circles indicates the transition from the lower level measured by inelastic tunnelling spectroscopy.

The modified crystal field parameters are considerably different from those values calculated by Serra et. al. [4]. However, the energy level diagram and $\chi_m - T$ calculated using modified CF calculated are in good agreement with

experimental results. The recalculated Energy Level Diagram is shown in the Figure 6.13. The transition jumps obtained from IETS are well within the range of expected energy level transitions.The important factor in this system is the $A_6^5$ term arising from the $C_5$ symmetry of the molecule,which is represent off diagonal anisotropy term. The value obtained for this term is lower than the previously calculated one. This indicates that the off-diagonal anisotropy is lower than the one estimated for the molecule. The reduction in $A_6^5$ term will also affect the extend of mixing of the $M_J$ s. However, it is difficult to estimate the extend of mixing by our experimental technique alone.

### 6.3.3 Kondo regime

The molecule was further pressed using the tip by increasing the PID set point conductance ( $> \ 10^{-3}G_0$). Tunnelling Spectroscopy taken on these pressed molecules shows Fano like structure at zero bias. Fano line observed at Fermi level is the manifestation of the Kondo effect. Fano formula can be used to describe the conductance of a magnetic ad-atom on top of metal surface [131, 157].

$$\frac{dI}{dV} = G_{off} + \frac{A}{(1+q^2)}\frac{(\varepsilon+q)^2}{(\varepsilon^2+1)} \tag{6.3}$$

where $\varepsilon = (eV - \varepsilon_k)/\Gamma$, $G_{off}$ is the conductance offset, A is the amplitude of the Fano resonance, q is Fano factor, $\varepsilon_k$ is the energy position with respect to Fermi level and $\Gamma$ is the half-width of the Kondo peak. Fano factor, q determines the line shape of the resonance. Line shape can vary from peak, dip or an asymmetric shape depending on the values of $q = \infty, 0, \pm 1$. Lines also give information about the hybridization of the two pathways. Fano fit for representative curves in shown in black colour in Figure 6.14.

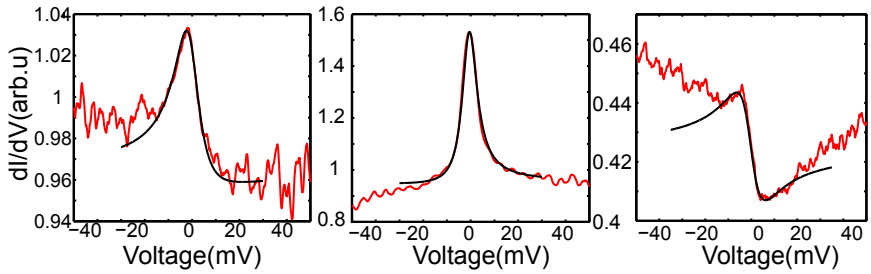


FIGURE 6.14: (a) and (b) $)dI/dV$ taken at contact regime $(10^{-3}G/G0)$ regime shows Fano resonances observed on molecule. Black lines are the Fano fit for the curves in low voltage regime

The Γ in the equation (1) is related to the Kondo temperature by the formula.

$$\Gamma = 2\sqrt{(\pi K_b T)^2 + 2(K_b T_k)^2)} \tag{6.4}$$

Γ obtained by fitting the Fano curves is 6.7 mV (average of all fields) and measurements were carried out 350 mK. Kondo temperature obtained by substituting these values in Equation 6.4 is 27.5 K. This value is similar to the Kondo temperature obtained in Dy - Pc2 Single Molecule deposited Cu2N/Cu using similar technique [158]. The interaction of the magnetic ad-atom spin with the conduction electrons of metal can change the magnetic state of the ad-atom. In order to access magnetic states and observe crystal field anisotropy it is necessary to decouple ad-atom from metal environment. Recently, Oberg *et al.* demonstrated that the exchange coupling interaction plays a major role in this when a magnetic ad-atom is placed in ultra-thin insulator on top metal [159]. Co atoms deposited on central region of insulating Cu2N showed purely inelastic tunnelling transitions while the one on the edge of Cu2N islands showed Kondo peak. They demonstrated that there is competition between crystal field anisotropy and Kondo effect which in fact determined by the coupling to metal surface.

Similarly in the case of DyW30, the outer polyoxometalate shell controls the coupling of the magnetic ion with the electrode. When the tip is far, the

molecule act as an insulator as seen in the high voltage spectroscopy. Unlike the case of Cu2N where magnetic atom lies on top of the insulating layer, here the magnetic atom is buried inside the dielectric. This weakens the strength of the signal from the magnetic ion when tip is far. As the tip is approaches towards the molecule, the tip – molecule coupling changes. When the molecule is in the intermediate coupling, we observe inelastic jump. Further increasing the coupling leads to an increased exchange coupling and results in Fano like shape at zero bias. The shape of the Fano is dependent on the q factor as explained in the section 5.2.2. This shows that the coupling between molecule and electrodes plays a major role and shape of curve depends on hybridization of the two pathways arising form this coupling.

## 6.4 Conclusions

Here we have shown that the magnetism in the polyoxometalate molecule, DyW30, deposited by spray deposition method can be investigated by using STM operating at cryogenic temperatures. The STM images show that the molecule is stable at the cryogenic temperature and can be addressed individually. The spin IETS conducted on the molecule shows clear magnetic signatures indicating that the molecule preserves magnetic on deposition on a metal surface. The spin transition values obtained from IET spectra are comparable with the same obtained from magnetisation measurement of the bulk samples. The emergence of Kondo on pressing the molecule to surface shows that the coupling of the molecule with the electrodes plays a significant role in spin dependent charge transport in metal-SMM-metal junctions. This results obtained during this work gives an insight about the magnetism of individual molecules on metallic surfaces and pave the way for the addressing the challenges in the molecular magnetism.

# Part IV

# Superconducting Proximity Effect in Graphene

# Chapter 7

# Review of Superconductivity and Graphene

In this chapter, I review the main developments in the field of superconductivity and Graphene. The first part of this chapter deals with the superconductors and the proximity effect in superconductors. The second part deals with the Graphene and proximity-induced superconductivity in Graphene.

## 7.1 Superconductivity

Superconductivity is a phenomenon, occurring in some materials, in which the resistivity of the materials drops to zero when it is cooled below a certain temperature.In this section, I will give a brief introduction to the superconductivity and the characteristics of superconductors.

### 7.1.1 How it all started

In 1911, Dutch physicist H. Kamerlingh Onnes and his assistant Gilles Holst observed that the dc resistivity of the Mercury dropped abruptly to zero when

it was cooled to a temperature below 4.2 K [160] (see Figure 7.1). This discovery marked the beginning of the Superconductivity. The temperature at which resistance drops to zero is called critical temperature, $T_c$. Soon after this observation they found that the lead and tin also shows superconductivity, but with a higher transition temperature [161]. The same group also observed that a sufficiently large magnetic field can restore the material to its normal state from the superconducting state [162]. Immediately after this pathbreaking discovery many researchers started looking for new superconducting materials. In the subsequent years, a lot of metals and alloys were found to be superconducting. However, superconductivity was not observed in noble metals such as gold, silver, etc. which usually good conductors of electricity at room temperature. Niobium shows the highest critical temperature of all the pure metals (Tc=9.2).

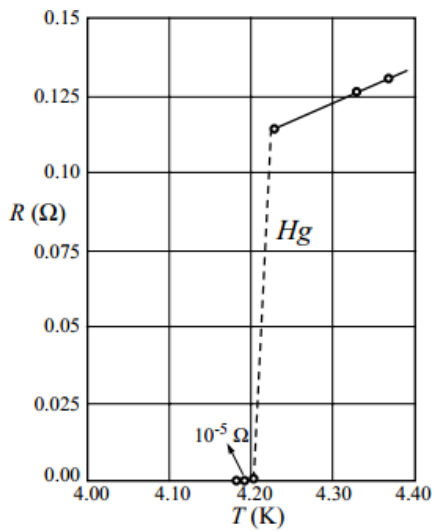


FIGURE 7.1: Experimental data of the resistance of mercury as a function of temperature performed by mercury by Gilles Holst and H. Kamerlingh Onnes. Figure from Ref [5]

In 1933, W. Meissner and R. Ochsenfeld discovered another fundamental property of the superconductors, perfect diamagnetism [163]. They observed that the magnetic flux is expelled from the interior of a superconducting material

when it is cooled below the critical temperature in the presence of a weak magnetic field.

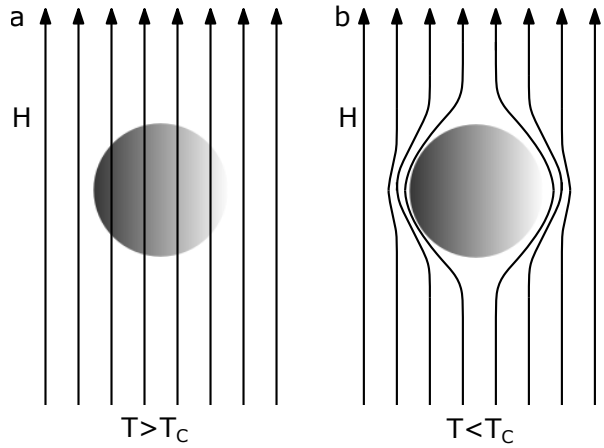


FIGURE 7.2: The figure shows Meissner effect, a superconductor cooled below its transition temperature ($T_c$) expulse external magnetic field from its interior. A superconductor (a)at $T > T_c$, and (b) at $T < T_c$.

In 1934, a phenomenological theory, two fluid model was proposed by C. J. Gorter and H. B. G. Casimir to explain superconductivity [164]. This approach was based on the assumption that there are two components for conducting electron fluid, normal and superconducting. This model was similar to the two-fluid model for Superfluids. In 1935, London brothers proposed two equations based on two fluid model to explain Meissner effect [165]. They described the expulsion of the magnetic field inside a Superconductors are due to the presence of supercurrents in the surface, which screens the magnetic field. The London equations also suggested that the magnetic field inside the superconductor decays exponentially up to a characteristic distance from its surface, which is called the London penetration depth, $\lambda_L$.

Later in 1937 Vortices in superconductors are discovered by Shubnikov [166]. This discovery showed that the total expulsion of the magnetic field from inside is only true for a particular type of superconductors.The superconductors exhibiting complete Meissner effect are called Type I superconductors. Eg: Al, Zn, Hg. In such materials, the diamagnetism completely vanishes at the

critical field, and it becomes a normal conductor. This transition in the type 1 material is very sharp. In type II superconductor, there are two critical fields, Lower Critical Field ($H_{c1}$) and Upper Critical Field ($H_{c2}$). The type 2 superconductors are perfectly diamagnetic below $H_{c1}$ and normal conductor above $H_{c2}$. In between these two critical fields, there exists a mixed state, in which the magnetic field partially penetrates the interior of the superconducting sample in microscopic filaments called vortices.

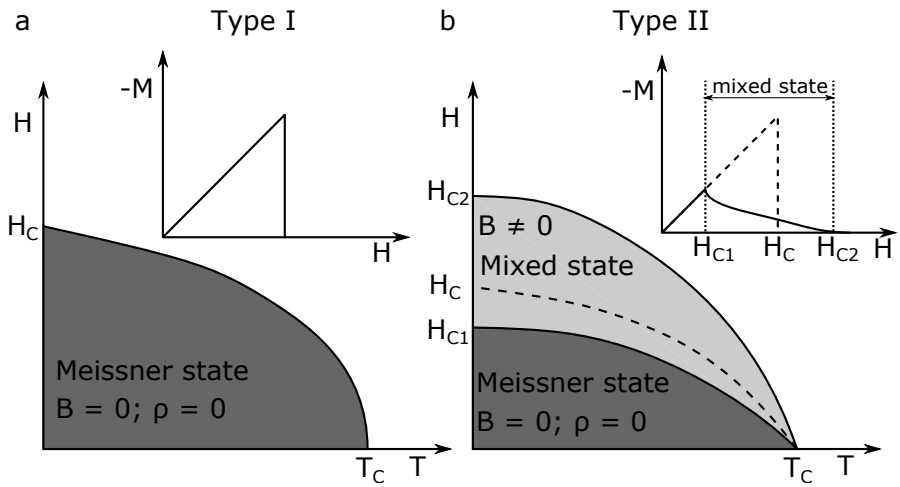


FIGURE 7.3: Figure shows schematics of magnetic field H vs Temperature T of the type I (a) and type II (b) superconductors. Inset figures shows magnetization curve for Type I (a) and Type II (b) Superconductors.

### 7.1.2 Ginzburg - Landau phenomenological theory

In 1950, V. L. Ginzburg and Lev Landau proposed a phenomenological theory (GL theory) to explain superconductivity based on the theory of Second-order phase transitions developed by Landau [167]. The state of a body changes gradually while its symmetry changes discontinuously at the transition temperature. According to two fluid model, there exist superconducting and normal electrons below the transition temperature $T_c$. In the GL theory, a order parameter $\Psi(r) =\mid \Psi(r) \mid e^{i\theta}$, where $\theta$ is the phase, is used to describe the

superconducting electrons. The density of probability, $\mid \Psi(r) \mid^2 = \Psi(r)^*\Psi(r)$ is a measurement of the superconducting electron density, $n_s$ at a point r.

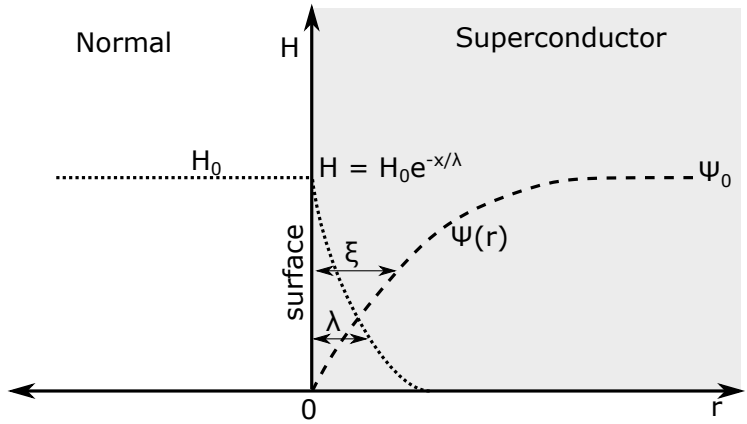


FIGURE 7.4: Spatial distribution of the magnetic field (H) and the superconducting order parameter $\Psi$ along normal-superconducting interface.

According to the Ginzburg-Landau (GL) theory, the characteristic scale over which variation of order parameter $\Psi$ occur is called Coherence length, $\xi_{GL}$. Ginzburg-Landau theory, obtained two equations for describing superconductivity presence of uniform magnetic field

$$\frac{1}{2m^*}(\imath\hbar\nabla + e^*A)^2\Psi + \beta \mid \Psi \mid^2 \Psi = -\alpha\Psi \tag{7.1a}$$

$$-j = \frac{\nabla^2 A}{\mu_0} = \frac{\imath e^*\hbar}{2m^*}(\Psi^*\nabla\Psi - \Psi\nabla\Psi^*) + \frac{e^{*2}}{m^*} \mid \Psi \mid^2 A \tag{7.1b}$$

Where A is the magnetic vector potential, $\alpha$ and $\beta$ are the two the phenomenological expansion coefficients that depend on the material and $m^* = 2m$ and $e^* = 2e$, the mass and charge of the superconducting electrons, respectively. These two equations are called Ginzburg-Landau equations, and it describes the superconducting order parameter and the penetration of magnetic field into the material in its superconducting state. They solve these equations in terms of penetration length $\lambda$ and coherence length $\xi_{GL}$. This solution showed

that, for certain conditions the magnetic field can enter the material, which results in uniform distribution of superconducting and non-superconducting (normal) regions. In this case, the magnetic field is expelled from the superconducting region and, meanwhile it passes through the normal regions. This scheme is showed in the Figure 7.4.

A vast majority of the majority of metallic superconductors are type - I superconductor. The magnetization curves of type I and type II superconductors are shown in the inset of Figure 7.3 . The magnetic field is expelled below the critical magnetic field $H_c$. The type I superconductors obeys the empirical relation $H_c = H_c(0)(1 - (\frac{T}{T_c})^2)$. For type - II materials, this is different. Type II materials have two critical fields (see figure 7.3). The lowest field at which the at which the field starts to penetrate the material is called lower critical field $H_{c1}$. The field at with a type II superconductor totally becomes normal conductor is called upper critical field $H_{c2}$. GL theory was helpful in explaining many observed characteristics of the superconductors. However, the phenomenological theory failed to give a complete picture of superconductivity.

### 7.1.3 BCS Microscopic Theory

In an ordinary metal, electrical resistance originates from the interaction of the electrons with the crystal lattice. What BCS predicted was that under certain circumstances electron- lattice interactions can lead to superconductivity. The role of lattice vibration in superconductivity was first predicted by H. Fröhlich in 1950 [168]. In the same year, E. Maxwell found Isotope effect verifying the predictions of Fröhlich

In 1956, Cooper showed that electrons in a solid will always form pairs if there exist an attractive potential [169]. An electron propagation in a solid can interact with the positively charged ions in the surroundings and cause a deformation of the crystal lattice. This deformation causes an excess of positive charge locally. This local created positive charge attracts another electron

passing near this region. Thus, a lattice vibration (phonon) mediated interaction generates attractive potential between two electrons, otherwise repulsed.

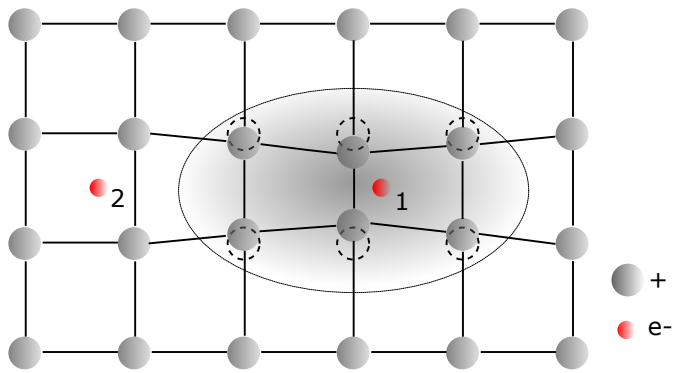


FIGURE 7.5: Schematic showing the formation of Cooper pair by a phonon mediated electron - electron interaction. The electrons are indicated red spheres and positive ions in the lattice by gray spheres. An electron moving in crystal attracts the positively charged lattice ions and generates a region of excess positive by distorting the crystal lattice. The pale glow in the figure indicates the positive cloud. Another electron (2) passing nearby is attracted toward the cloud. The figure is for illustration, in reality second electron also cause lattice distortion.

In his 1956 seminal paper, Copper showed that these electrons may be considered as pairs bound by mutual exchange of virtual phonons. The Figure 7.6 illustrates this process. An electron, near the Fermi surface, in a state $\mathbf{k_1}$ emits a phonon $\mathbf{q}$ and scatters into a $\mathbf{k_1'} = \mathbf{k_1} - \mathbf{q}$. Another electron in state $\vec{k_2}$ absorb this phonon and changes to a state $\mathbf{k_2'} = \mathbf{k_2} + \mathbf{q}$. To preserve the law of conservation of momentum, the process must follow the condition, $\mathbf{k_1'} + \mathbf{k_2'} = \mathbf{k_1} + \mathbf{k_2} = \mathbf{K}$, where $\mathbf{K}$ is the total momentum.

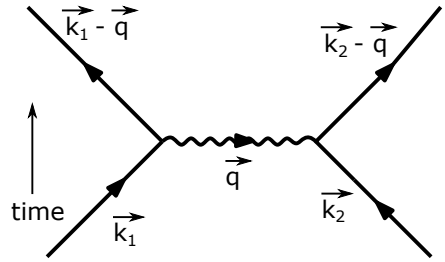


FIGURE 7.6: (a)Feynman diagram showing electron-electron interaction via exchange of a virtual phonon of momentum $\hbar q$

This interaction could be of attractive or repulsive nature, depending on two factors - (1) The energy of interacting phonon and (2) The energy difference between the initial states and final states of the participating electron. When the phonon exchange energy is greater than the Coulomb repulsion energies, it results in an attractive potential energy. This pair of participating electrons occupying this phonon mediated bound state is called a Cooper pair. To achieve a lower energy configuration, it requires a strong interaction between the Cooper pairs, which is achieved through inter-pair electron transfer between the pairs. The inter - pair electron transition has maximum probability when all the pairs have the same momentum. This condition is satisfied when the total momentum ($\mathbf{P} = \hbar\mathbf{K}$) is zero. Hence, total wave vector $\mathbf{K} = \mathbf{k_1} + \mathbf{k_2}$ should be zero. This is satisfied when ($\mathbf{k_1} = -\mathbf{k_2}$ i.e. ($\mathbf{k_1} = \mathbf{k}$ & $\mathbf{k_2} = -\mathbf{k}$). This shows that the pair forming electrons should have equal and opposite momentum. Another requisite for minimizing the energy is that the electrons forming Cooper pair should have opposite spin. This condition makes the net spin of Cooper pair is zero. Hence, the Copper pair behaves like a boson (integer spin particle). These particles can occupy the common ground state.

Later in 1957, Bardeen, Cooper and Schrieffer extended the work of Copper and proposed a theory for superconductors. This theory was a breakthrough because it was the first microscopic theory for explaining superconductivity. This theory predicted an instability of the Fermi surface in the presence of attractive interaction between electrons. The system forms Copper pairs to

reduce the total energy. The average distance between the electron pair is called the coherence length, $\xi$. The coherence length can be found by measuring the superconductors in the presence of a magnetic field, and the value obtained is of the order of 100 nm, which is very large comparing the inter - atomic distance ($0.1 - 0.4$ nm) in crystals. Due to the large coherence length the copper pair the wave function associated with various pairs overlap. Thus, the ground state is formed in the case is a result of the coherent superposition of these Cooper pair wave-function. At $T = 0$, these copper pairs behave as bosons and forms a superconducting condensate. The superconducting condensation leads to a reduction in potential energy. Thus, the electron pairs have lower energy and posses an energy gap in the ground state. Hence, these pairs are unaffected by the collision interactions due to the defects in the lattice. The energy gap $\Delta$ at the Fermi level in the excitation spectrum of a superconductor is a characteristic property of superconductor. When the thermal excitation energy is less than the band gap, the material shows zero resistivity. The elementary excitation spectrum of a superconductor is shown in Figure 7.7a. The BCS theory gives an expression for the elementary excitation spectrum of a superconductor [170]

$$E_k = \sqrt{\Delta^2 + \varepsilon_k^2} \quad ; where\ \varepsilon_k = \left( \frac{\hbar^2 k^2}{2m} - \frac{\hbar^2 k_F^2}{2m} \right)^2 \tag{7.2}$$

Where $k$ is the momentum measured with respect to the Fermi momentum. The Figure 7.7b shows the $E_k$ - k diagram. This clearly shows that an energy of $\Delta$ is required to excite a Cooper pair to an excited state. Also, the number of states is conserved during the superconducting state.

$$N_N(\varepsilon_k) d\varepsilon_k = N_S(E_k) dE_k \tag{7.3}$$

Where $N_N(\varepsilon_k)$ is the density of states for the normal state phase, which is a constant near Fermi level, and $N_S(E_k)$ is the density of states for superconducting phase.

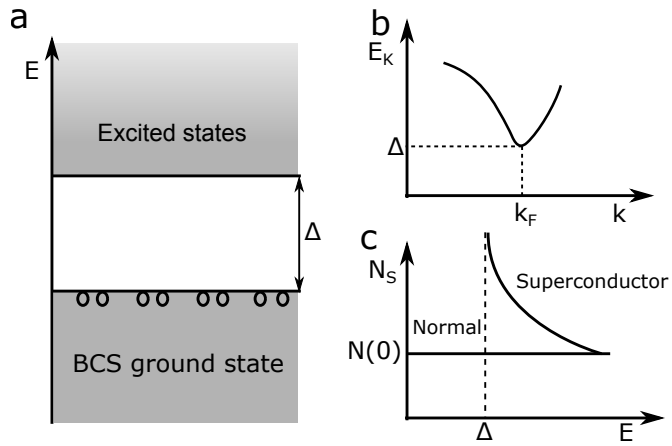


FIGURE 7.7: (a)Schematics showing excitation spectrum of a superconductor at temperature,T = 0. An energy gap of Δ separates the BCS ground state and excites states. (b) Shows $E_K$ - k diagram of a superconductor (c) Shows the density of states of a normal metal N(0) and Superconductor $N_S$. The superconductor density diverges near energy Δ.

From the Equation 7.2 and 7.3, we can deduce an expression for the ration of density of states of a superconductor to the normal state.

$$\frac{N_S(E)}{N_N(0)} = \begin{cases} 0 & \text{for } E-\mu < \Delta \\ \frac{E-\mu}{\sqrt{(E-\mu)^2+\Delta^2}} & \text{for } E-\mu > \Delta. \end{cases} \tag{7.4}$$

Schematics of this expression is shown in Figure 7.7c. When $E-\mu < \Delta$, there are no available states close to the Fermi Level, $E_F$. When, $E-\mu > \Delta$ it follows the above formula. At $E = \Delta$ the density of state shows divergence as shown in the figure 7.7c. The BCS theory also gives expression for this Δ. At T =0, $\Delta(0) \approx 1.76 k_B T_c$, where $k_B$ is the Boltzmann constant and $T_c$ transition temperature.

BCS theory was successful in explaining the properties of superconductors. In 1972, they were awarded Nobel Prize for this work [171]. Later in 1986, Bednorz et. al. discovered superconductivity in LBCO, which had a transition temperature of 30 K [172]. This lead to the discovery of new class

of superconductors called High $T_c$ superconductors, that are materials whose transition temperature is above 30 K ( the maximum $T_c$ predicted by the BCS Theory). Recently, high $T_c$ superconductivity was reported in Iron-based materials [173]. Even though, many high $T_c$ materials were discovered in past 30 years, the theory behind these materials remains as a mystery and is one of the open problems in physics.

### 7.1.4 Proximity Effect

When a superconducting material S is in contact with a normal metal N, it exhibits the proximity effect, i.e., the superconductor induces superconductivity in the Normal metal. This induced superconductivity exists only in a thin surface layer of the normal metal near the NS interface, typically around 100 nm. The metal in electrical contact acquires superconducting characteristics such as zero resistivity, perfect diamagnetism, etc.

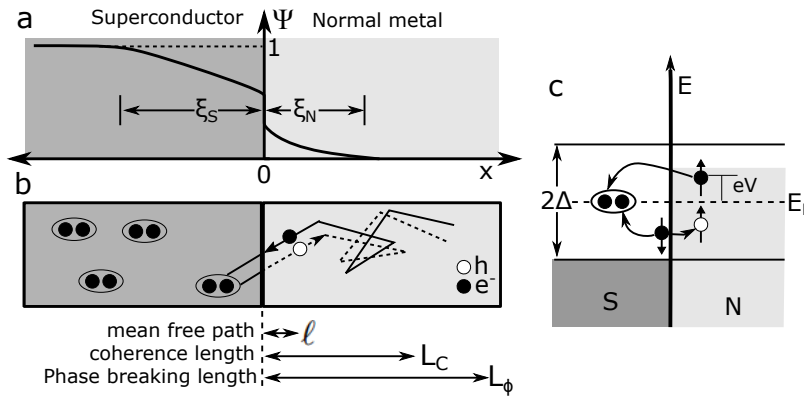


FIGURE 7.8: (a) Schematics showing the changes in Order parameter $\Psi$ in Superconductor - Normal Metal interface at temperature, $T < T_c$, (b) Scheme showing the Andreev reflection in a NS interface. Different length scales are also marked. (c) depicts the energy level diagram for the formation of Cooper pair by Andreev Reflection

Consider an interface between a normal metal and a superconductor as shown in Figure 7.8 (region $x < 0$ is Superconductor and$x > 0$ is Normal Metal). The distance to which the order parameters enters in the Normal metal is

called effective coherence length $\xi_N$. In a normal metal, when the electron means free path, $\ell$ is larger than the effective coherence length ( $\ell >> \xi_N$ ), and then the condition is referred as the clean limit. If $\ell << \xi_N$ then its called the dirty limit. The proximity effect takes place by the penetration of Cooper pairs into the Normal metal. Consider an electron from the normal metal region moving towards the NS interface. If the electron energy is less than the energy gap of the superconductor ($E < \Delta$), then the electron cannot enter the superconductor since there is no available states. The charge transfer in this case occur through Andreev Reflections [174]. This process is depicted in Figure 7.8c. The electron can only enter the superconducting region as a Cooper pair. The incident electron pairs up with another electron to form a Cooper pair. This new electron is obtained by creating a hole at the interface. If the incident electron is spin up, it pairs up with a spin down electron to form Cooper pair. To conserve the total spin, the hole created must have spin up. This hole moves away from the interface. The momentum of the electron is given

$$k_e = \sqrt{2m(E_F + E)} \quad ; \quad k_h = \sqrt{2m(E_F - E)} \tag{7.5}$$

This process results in the charge transfer from N to S region. The hole reflected back at the interface trace back the path of the incident electron pair coherently over a distance $L_C$. This coherence length, in this case, is expressed by equation [7, 175]

$$L_C = min\left\{\sqrt{\frac{\hbar D}{E}}, L_\phi\right\} \tag{7.6}$$

where, D is the diffusion constant of the material, E is the energy of the electron states, and $L_\phi$ is the phase coherence length in Normal metal.

### 7.1.5 Spatially resolved measurement of Proximity effect

As mentioned above, the diffusion of Cooper pair into the N region alters local density of state. This extends to a length $L_C$ from the interface (see Figure 7.8). Combined Scanning Tunnelling Microscopy and Spectroscopy enables one to resolve spatially these changes in density of states with atomic precision. However, these experiments are difficult to carry-out since (1) this requires well-defined NS interface and (2) STM operating at milliKelvin temperature.

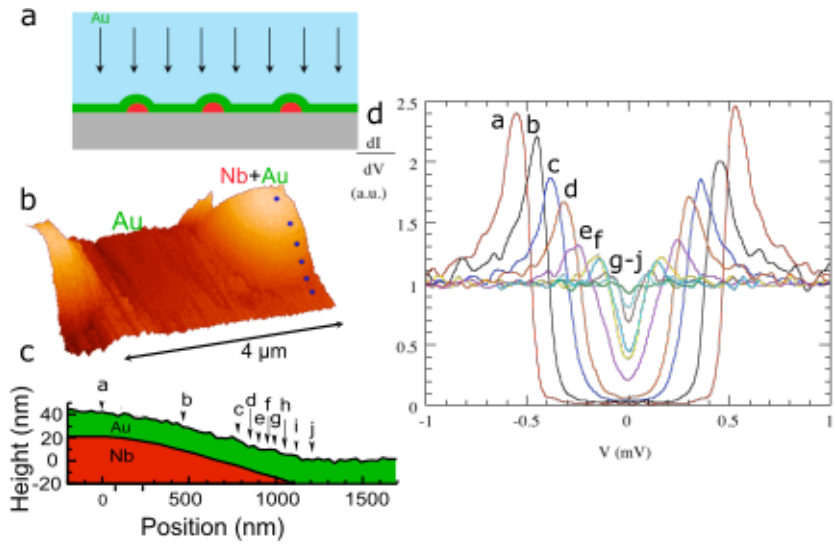


FIGURE 7.9: (a) Shows the scheme of sample preparation, Au (green colour) is evaporated on to a pre-deposited Nb spots (red) (b) STM image of the sample showing the hill created by deposition (c) shows the line profile of the surface extracted from image (d) Experimental spectra measured on locations a to j . Figure from Ref [6].

One of the first attempts to measure proximity was carried out by Moussy et.al. [6]. The Scheme of the experiment is shown in Figure 7.9a-c. They were able to probe the local density of states in the region close to N-S interface. They observed in the inverse proximity effect in the superconducting region. They also observed a pseudo-gap with decreasing amplitude along the N-S interface and theoretical model using Usadel equations. They estimated the

characteristic length of NS material around 300 nm. However, in this case, the NS interface was determined indirectly.

Recently, with the advancement of the advanced in-situ sample preparation techniques and combined low-temperature STM proximity effect was studied with unprecedented precision [7, 176, 177].

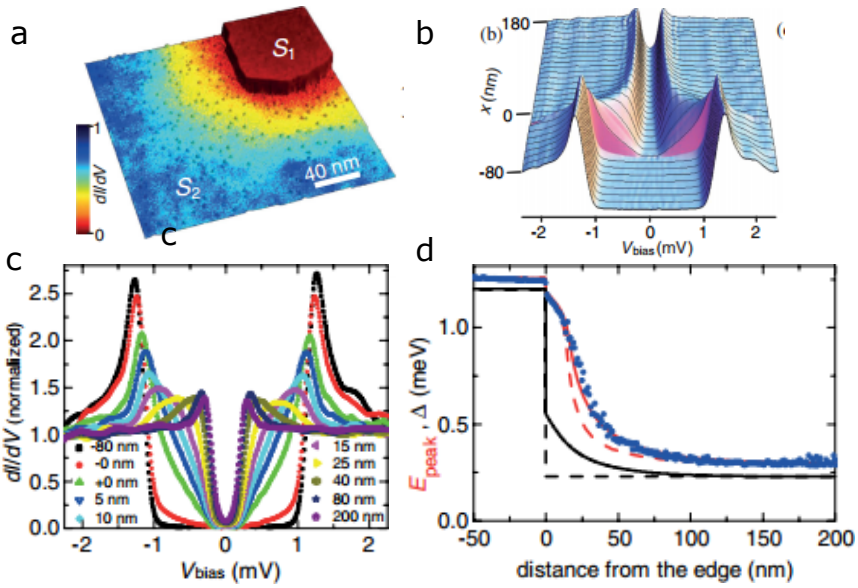


FIGURE 7.10: The figures shows a Super - Super region. (a) Topographic STM image of the sample showing the Pb nanoisland S1 connected to the striped incommensurate Pb monolayer S2. (b) shows the Spatial and energy evolution of the tunneling conductance spectra obatained across the junction (c) Selected local tunneling spectra (d) Spatial evolution of the energy of the peak maximum across the interface. Figure from Ref [7].

One of the noteworthy experiment performed recently was conducted by Cherkez et. al. [7]. They could be experimental measure proximity effect between two superconductors. They could grow a lateral junction composed of a large-gap Pb island $S_1$ and a small-gap crystalline atomic Pb monolayer with a gap $S_2$ and probed using an LT-STM. The observed proximity induced changes in tunnelling spectra was modelled using a self-consistent solution of the Usadel

equations. They could observe proximity-induced superconductivity in sample. Also, they could find a weak inverse proximity effect and resolve one of the old problems regarding proximity effect.

## 7.2 Two Dimensional Materials

Discovery of Graphene by Andre Geim and Kostya Novoselov in 2004 commenced a new era of two-dimensional materials [178]. This experiment paved the way to experimental and theoretical advancement in 2-D materials. In 2010, Geim and Novoselov were awarded the Nobel Prize in physics "for ground breaking experiments regarding the two-dimensional material Graphene" [179]. A lot of 2-D materials with astonishing properties and a wide range of application were discovered following the discovery of graphene [180]. Even after ten years Graphene remains as one of the hot topics in materials research.

### 7.2.1 Graphene

Graphene, the first discovered 2 D material, is a one-atom-thick sheet of carbon atoms which forms a two-dimensional honeycomb lattice. The Graphene arises from the properties of the carbon atom to form various allotrope. The carbon has atomic number 6 and a ground state electronic configuration of $1s^2 2s^2 2p^2$. The outer 2s and 2p orbitals are separated only by a 4 eV energy. This low energy helps to the outer orbitals to form various hydrations. One 2s and two 2p orbitals hybridize to form three $sp^2$ hybridized orbital which form a planar structure. These orbitals form $120^0$ to each other. The remaining one hybridised 2p orbital is perpendicular to this plane. In Graphene, these $sp^2$ orbitals combine to form a honeycomb structure.

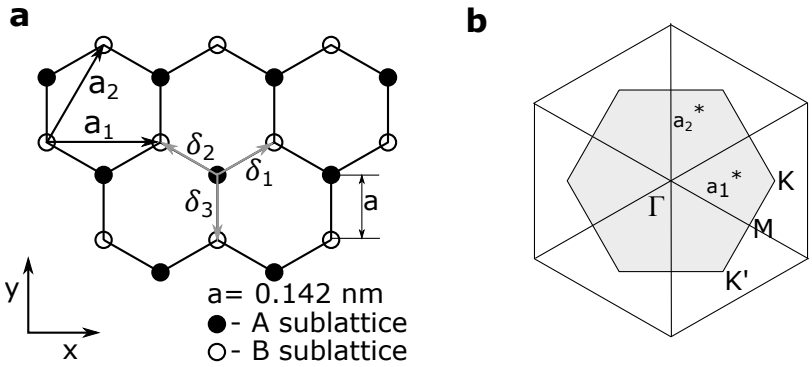


FIGURE 7.11: (a)The vectors $\mathbf{a_2}$ and $\mathbf{a_2}$ marks the unit vectors of the triangular Bravais lattice. Meanwhile vectors $\delta_1$, $\delta_2$ and $\delta_3$ are the nearest neighbour vectors. (b) Shows the reciprocal lattice of the triangular lattice. The primitive lattice vectors are $\mathbf{a_1^*}$ and $\mathbf{a_2^*}$. The grey region inidcates the first Brillouin zone (BZ), with centre Γ and the high symmetery corners K, K' and M. Image adapted from ref [8].

The Figure 7.11 shows triangular Bravais lattice. The unit cell in the Bravais lattice has two equivalent carbon atoms marked as the A and B. The A and B sublattice are separated by a distance, $a = 0.142$ nm.

The three vectors connecting A sub-lattice with nearest-neighbour B sublattice are

$$\delta_1 = \frac{\mathbf{a}}{\mathbf{2}}\left(\sqrt{\mathbf{3}}\mathbf{e_x} + \mathbf{e_y}\right); \quad \delta_2 = \frac{\mathbf{a}}{\mathbf{2}}\left(-\sqrt{\mathbf{3}}\mathbf{e_x} + \mathbf{e_y}\right); \quad \delta_3 = -\mathbf{a}\mathbf{e_y} \tag{7.7}$$

and the triangular Bravais lattice is represented by the basis vectors.

$$\mathbf{a_1} = \sqrt{\mathbf{3}}\mathbf{a}\mathbf{e_x}; \quad \mathbf{a_2} = \frac{\sqrt{\mathbf{3}}\mathbf{a}}{\mathbf{2}}\left(\mathbf{e_x} + \sqrt{\mathbf{3}}\mathbf{e_y}\right) \tag{7.8}$$

The lattice spacing is given by, $\bar{a} = \sqrt{3}a = 0.24$ nm. The area of the unit cell is given by $A_{uc} = \sqrt{3}\bar{a}/2 = 0.051\text{nm}^2$. There are two atoms per unit cell. hence the density of carbon atom is , $n_C = 2/A_{uc} = 39$ nm$^{-2}$. Every carbon atom has one electron from the hybridized orbital. In the sp2 hybridization, the

hybridized in plane atoms forming $\sigma$ bond and unhybridized p orbital forming $\pi$ bond. The energy dispersion relation for the two-dimensional Graphene was solved by Philip Wallace in 1947 using the tight-binding method and can be expressed as [8, 181]

$$E^{\pm}(k_x, k_y) = E_F \pm \gamma_0 \sqrt{1 + 4cos^2\left(\frac{k_x a}{2}\right) + 4\,\cos\left(\frac{k_x a}{2}\right) cos\left(\frac{\sqrt{3}k_y a}{2}\right)} \tag{7.9}$$

where $\gamma_0$ is the nearest-neighbor hopping energy ($\gamma_0 \approx 2.8$ eV). The excitation spectrum of Graphene has two bands that are symmetrical around E = 0. The $E^+$ branch correspond to the $\pi^*$ and $E^-$ to the $\pi$ branch. Figure 7.12 shows the electronic energy dispersion relations for graphene as a function of the two-dimensional wave-vector k in the hexagonal Brillouin zone. The band crossing occurs at the K and K' points.

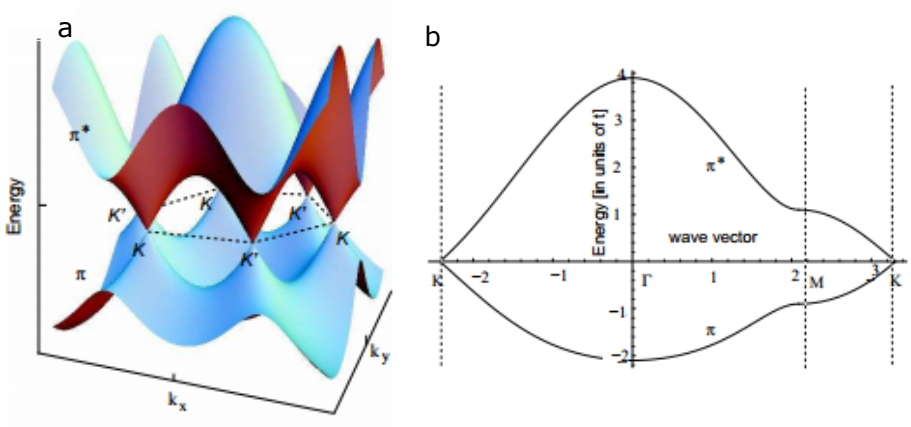


FIGURE 7.12: (a) Energy dispersion as a function of the wave-vector components $k_x$ and $k_y$. (b) Cut throught the energy dispersion along characteristic lines (connecting the points $K \to \Gamma \to M \to K$. The energy is measured in units of t and the wave vectors in units of 1/a. [8].

The Graphene energy dispersion is similar to that of the Dirac spectrum for massless fermions [182]. Hence, the charge carriers in Graphene are described

by a Dirac-like spectrum. This is due to the Graphene structure. As shown in the Figure 7.12 has a conical energy dispersion. Thus the quasiparticles in graphene exhibit a linear dispersion relation $E = \hbar v_F \sqrt{k_x^2 + k_y^2}$ and behave as massless relativistic particles analogous to photons.

### 7.2.2 Proximity Effect in Graphene

Even though, Graphene is not an intrinsic superconductor; superconductivity can be induced in Graphene. This is achieved mainly by two methods, (1) *Graphene intercalated Compounds (GIC)* and (2) *Proximity Effect* . Graphene Intercalated Compounds are materials based on Highly Ordered Pyrolytic Graphic (HOPG) in which Graphene layers are separated by intercalated ions. Superconductivity in such materials was first reported by Hannay et. al. in 1965 [183]. The recent discovery of Graphene re-initiated research in Graphene intercalated materials, and superconductivity was reported some of the newly found intercalated compounds [184, 185]. However, the mechanism of superconductivity in these compounds are not very clear.

Another mechanism to induce superconductivity in Graphene is by Proximity Effect. i.e. by keeping Graphene in close contact to a superconductor. In recent years, many groups reported proximity-induced superconductivity in Graphene [186–189].

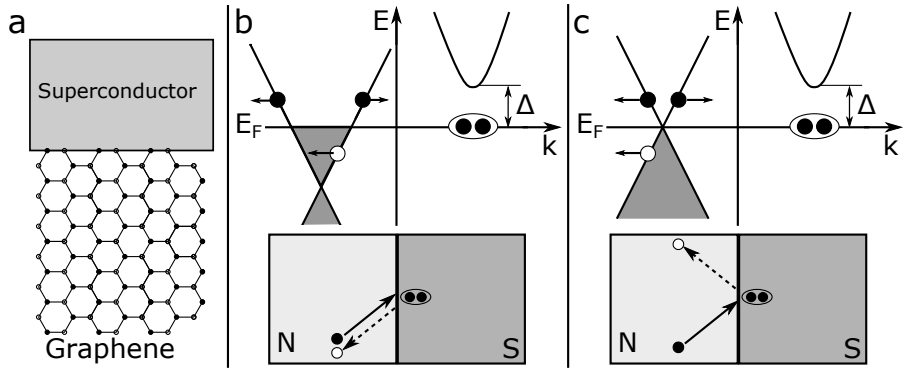


FIGURE 7.13: (a)Schematic showing Graphene - Superconductor interface. The cartoon showing (b) Normal Andreev Reflection, (c) Specular Andreev Reflaction and corresponding energy level diagram. In normal reflection, hole is reflected in the same direction of the incident electron. Meanwhile, the hole makes a reflection angle with the incident electron direction.

In proximity effect, the Cooper pairs from the superconducting region penetrate into the Graphene area. When $E < \Delta$ Andreev Reflection (AR) takes place. However, there are two types of Andreev Reflection in the case of Graphene - Super Interface. (1)Specular AR and (2) Normal AR [190, 191] .

In the case of specular Andreev reflection, the Graphene is not doped ($E_F = 0$). The end of cone lies in the $E_F$. The schematic of the specular Andreev reflection is shown in Figure 7.13c. When the energy of the incident electron is less than $\Delta$ Andreev reflection takes places as mentioned in section 7.1.4. To obey the conservation laws, the reflected hole should process same energy but in valence band .i.e (-E). In this case, electron and hole lie in the same energy band. The hole is reflected in an angle from the incident electron path (see Figure 7.13c bottom panel). Hence the name specular Andreev Reflection. The schematic for the normal AR is shown in Figure 7.13b. In this case, the Graphene is heavily doped ($E_F >> 0$) and hence the Dirac point is far from the Fermi level. In this case, the hole and electron lie in the same band. The reflected hole trace back the path of the incident electron (retro-reflection). Depending on the doping of Graphene, i.e. the position of Dirac cone with respect to the $E_F$, specular or normal Andreev reflection can occur

in Graphene - Superconductor Junction. Beenakker theoretically showed that, for retroreflection the subgap conductance increases with voltage from 4/3 to twice the ballistic value and in the case of specular reflection conductance drops from twice to 4/3 the ballistic value [191].

This prediction clearly shows that the changes in the local density of state induced by the normal and specular AR will be different. This changes can be investigated using scanning probe microscopes. Also, we need to fabricate a sample with the clear Graphene - Superconductor interface. However, preparing such samples and conducting spatially resolved measurements on this sample are technically challenging.

# Chapter 8

# Proximity Induced Superconductivity in Graphene

In this chapter we investigate the feasibility of fabricating atomically flat superconducting substrates using graphene placed in close proximity with a bulk superconductor. The properties of the resulting hybrid substrate is characterized using scanning probe microscopy.

## 8.1 Motivation

In the previous chapter, we discussed about Single Molecule Magnets deposited on a non-magnetic metal surface and probing the spin using inelastic tunnelling spectroscopy. To make an actual spintronic devices using SMMs, we need to investigate spin sensitive of these systems. This spin sensitivity of SMM can be studied by depositing them on magnetic surfaces [192] or superconducting surface [190]. Typically these experiments are carried out at ultra-high vacuum (UHV) and is limited to molecules which are compatible with UHV

conditions. To deposit a non-UHV compatible molecule we need to resort to wet deposition methods, and hence these substrates have to be exposed to ambient conditions. Unlike gold substrates, the magnetic and superconducting substrates get oxidised very quickly in ambient conditions and loses its surface properties. Hence, these substrates are not suitable for wet sample preparation method. One way to overcome this problem is to use an intermediate material to cover these magnetic or superconducting material that protect its surface from oxidation and at the same time preserves the magnetic or superconducting characteristics. A suitable material for this purpose could be graphene, which is a one-atom-thick layer of graphite. Intrinsically graphene is a not a superconducting material. However, graphene can be made superconducting by utilising proximity effect [186].The proximity induced superconducting graphene surface could serve as an ideal candidate for depositing SMMs. We fabricated samples in which graphene is placed in contact with a bulk superconductor in various geometries. The samples were characterised in ambient temperature using AFM and at low temperatures using STM with a superconducting tip.

## 8.2 Fabrication of Samples

### 8.2.1 Superconductor Deposited from STM Tip

In the previous investigations where proximity-induced superconductivity was studied by measuring spatially resolved scanning tunnelling spectroscopy, the samples were prepared at Ultra High Vacuum (UHV) conditions. In most of these studies, a superconducting island is grown in-situ on a well-defined substrate using various UHV deposition techniques [176, 177]. However, in our case the system is non-compatible with the UHV deposition methods. Hence, we tried an alternative method to deposit superconducting material on the substrates.

Recently, Andres Castellanos *et al.* described about a method to make metallic islands on substrates at low temperature using STM tip [193]. They applied a high voltage pulse (3 V - 9 V) between STM tip and substrate, and deposited tip material on the substrate. This sign of the voltage pulse and magnitude controls the size of the islands created.These islands were used for mechanically annealing the STM tip [193]. They used a normal metal (Au) as tip. This opens up the possibility of depositing superconducting materials in-situ by using superconductors STM tip. The use of superconducting lead (Pb) as STM tip was pioneered by Rodrigo *et al.* [194]. We followed his procedure to obtain a superconducting Pb tip.

A freshly cut metal piece of lead is soldered to STM tip base. Unlike the metallic wires (Au, Pt, Pt-Ir, etc.) used for STM, Pb is very soft making very sharp tip using lead is difficult, and also thin Pb tips bends faster on crash to surface. The tip is prepared by mechanical polishing and sharpening to obtain an inverted pyramidal shape. The STM tip is brought into tunnelling contact with the surface using piezo actuators. Then a voltage pulse is applied between the tip and surface. In the STM set-up, voltage is applied to the surface, and the polarity of the tip is selected such that the tip is kept at a negative potential with respect to the surface. Typically a +9 V pulse is applied for 0.05 seconds as mention in the above reference. This is repeated two or more times. The tip is mechanically annealed as described in ref [193] .

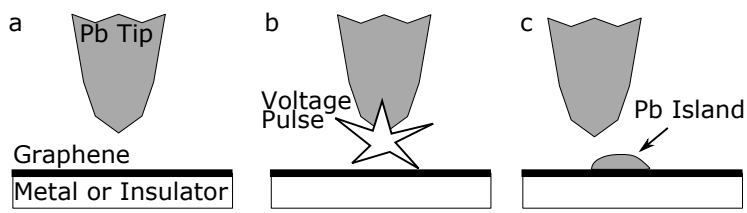


FIGURE 8.1: Scheme showing deposition of Lead on a graphene sample. (a) STM tip is moved close to the sample (b) a high voltage pulse is applied between tip and sample (c) Lead island deposited on substrate.

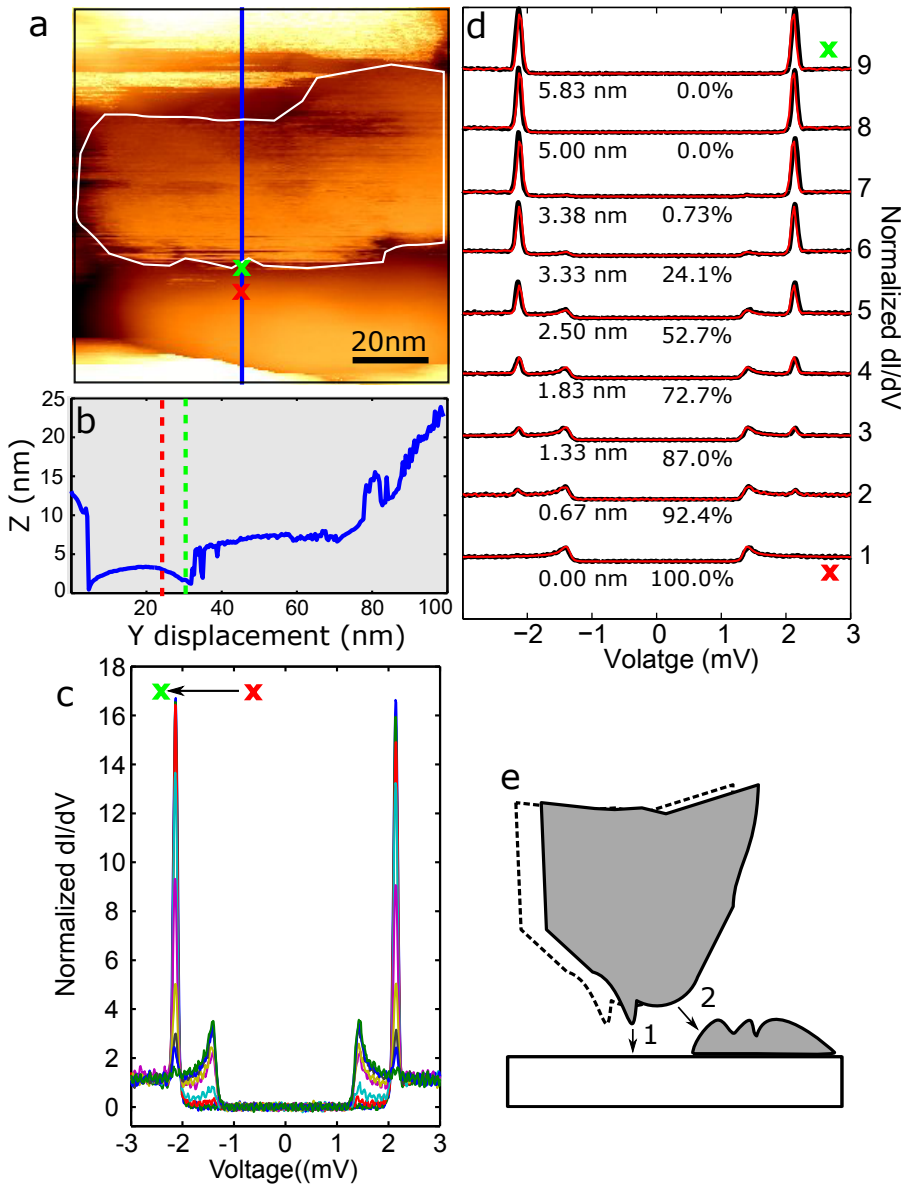


FIGURE 8.2: (a) STM image of the Pb island deposited from the tip by applying voltage pulse ($I_t = 10.0\ mV$, $I_t = 1.0\ nA$). The red and green cross mark indicates the region where spectroscopy was carried out along the line (b) Line profile of the blue line drawn on (a). (c) STS taken along a line from red cross mark to green cross mark (d) STS and fit for two channel model. dI/dV are shifted for clarity. (e) cartoon showing the scheme of experiment

We initially tested this method on the gold substrate. The Figure 8.2a shows the STM image of Pb deposited on Gold surface. The white coloured indicates the boundary of the lead deposited from the tip. The Figure 8.2b displays the line profile drawn on Figure 8.2a (blue colour). The Pb region has an approximate height of 3.0 nm and spread in around a 40 nm $\times$ 100 nm area. Scanning tunneling spectroscopy is done at different points along the line connecting red and green cross. The STS on the red line show Super-Normal(SN) curves with a superconducting gap of 1.4 eV, which correspond to the tip. Meanwhile, the STS taken on green shows two gaps. The super-super gap is 2.1 eV. One gap is corresponds to the STM tip and the other to the substrate. This indicates that the Pb deposited from the tip has a reduced superconducting gap (0.7eV). This reduced gap can be due reduced dimension since the size effect can alter the superconducting gap in the nano-islands of superconductors as observed in previous experiments [176, 177, 195, 196]. In these experiments, the superconductor was grown on the well-defined surface, and hence they could estimate the atomic layer involved in the formation of the islands. In our case determining the number of layers involved is difficult since the bottom layer is not well defined. However, the spectroscopy could clearly distinguish the superconducting region for the normal region. The gap on the island is uniform, indicating that the Pb is uniformly spread. There is a change in the Spectroscopy as we move from along the border of the island. The change in the STS from Normal to Super near the Pb island is due to the tip size effect rather than proximity. This change is observed only for the small distance ($< 6\ nm$) from the island.

The tip prepared in this experimental set-up is blunt. However, the blunt part also contributes depending on the shape of the sample. Figure 8.2e shows a cartoon showing a situation similar to our case. In this case, there are two channels, (1) one tunneling channel from the sharp tip to the Normal region and (2) another channel that links the superconducting island. SS part is modelled with a BCS tunnelling model between two superconductors. In this case, they have two different gaps tip (1.4 $eV$) and Pb island (0.7 $eV$). NS is modelled with BCS Normal - Super tunnelling equation (Tip gap of

1.4 $eV$). The total current observed is the sum of these two channels. The resulting current depends on the extent of the contribution of each channel. The experimental curve (black) and fit (red) is shown in the Figure 8.2f. The curves are shifted vertically for clarity. The percentage shows the extent of the contribution of Normal - Super channel. 100% indicates the tunnelling is totally N-S while 0% indicates that process is totally through SS. As the STS shows, as the tip moves close to the island the SS part dominates the process.

This results shows that to measure the proximity effect using the present experimental configuration, the sample should hold following conditions; (1) graphene layer lying on a flat substrate, (2) the substrate should have superconducting and non-superconducting regions, and (3) well-defined boundary should separate these two areas (see figure 8.3).

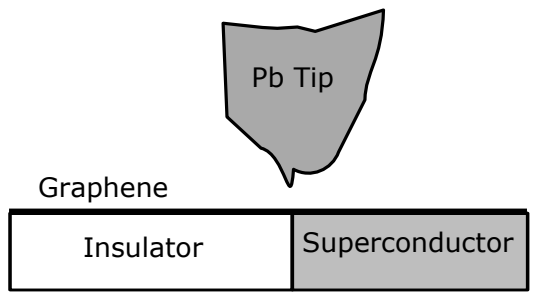


FIGURE 8.3: Scheme showing Tip - Sample arrangement to measure Proximity Effect in graphene

### 8.2.2 Preparation of Graphene/Pb/PMMA Samples

As shown in the Figure 8.3, the graphene should be lying on a substrate with superconducting and non- superconducting regions. We followed the following strategy to such a substrate.

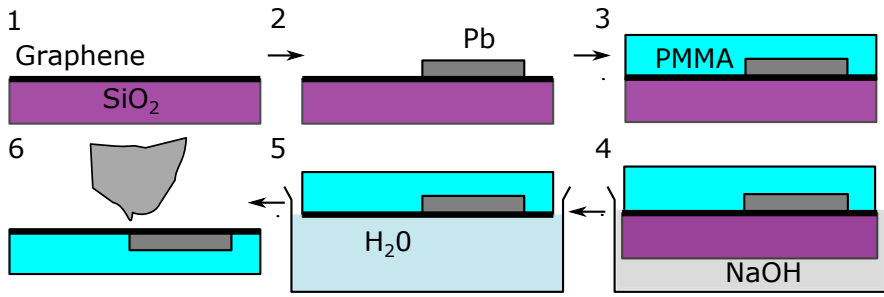


FIGURE 8.4: Scheme showing the device Fabrication of Graphene/Pb/P-MMA samples

The Figure 8.4 shows the scheme of preparation of the samples. The steps involved in the process are

*Step 1 :* Graphene on $SiO_2$/Si (Doped Si wafers with a 300 nm thick layer) purchased from Graphena was used as the base substrate. 10 mm $\times$ 10 *mm* sized wafers were cut and cleaned by sonication in isopropanol for 5 minutes.

*Step 2 :* Th lead was deposited on this sample by thermal evaporation method. The lead is heated in Tantalum boat and evaporated on to the sample. The mask is used to cover the sample is arranged in such way that only on one-half of the sample is exposed. A 300 nm thick lead was deposited on the sample. The base pressure of the evaporation chamber was kept around$5 \times 10^{-6}$ mbar.

*Step 3 :* Spin-coat the substrate with Polymethyl methacrylate (PMMA) for 1 min @ 5000 rpm. The sample was dried overnight.

*Step 4 :* Then the sample is partially dipped into a beaker of 1 molar aqueous solution of NaOH at $100^0$ C. This process will etch out the $SiO_2$.

*Step 5 :* After etching $SiO_2$, the sample is transferred to milliQ water at room temperature. The sample floats on the top of water due to the surface tension and hydrophobic nature of PMMA.

*Step 6 :* Sample is taken out of the water and dried in the presence of inert gas.

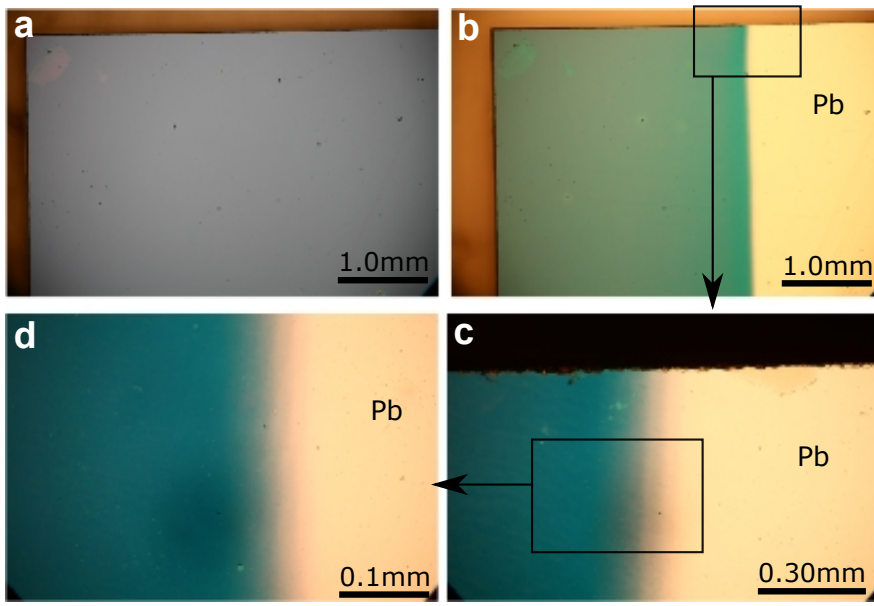


FIGURE 8.5: Figure shows (a) Graphene on $SiO_2$ after cleaning by sonication. (b)After evaporating Pb and coating with PMMA. (c) & (d) are 20X and 50X zoom in of sample. The black rectangle indicates the zoomed region.

The Figure 8.5 shows the optical image of the substrate during various stages of sample preparation. The Figure 8.5a shows the sample after the first step.Figure 8.5a shows the sample after step 3, i.e. after evaporating lead and coating with the PMMA. The zoom of this figure, on the boundary region (Pb/PMMA) is shown in the bottom figure. The zoom of the optical image shows that the border of Pb - PMMA region is very spread and not well defined. This obscure boundaries are spread over 0.05 mm wide region (see Figure 8.5d). It would be difficult to measure proximity in such vague boundaries. Hence, we did not proceed further with the procedure.

### 8.2.3 Preparation of Graphene/BN/Pb Samples

We tried the an alternative procedure to obtain a substrate with well-defined border between superconducting and non-superconducting region. We prepared a such sample using lead and Boron Nitride flakes. The Pb is a superconductor [197] and h-BN is well-known insulator [198]. The flakes of h-BN were deposited on graphene on Silicon-dioxide. BN is a layered material and cleave in perfect crystal planes with sharp boundaries. The lead is evaporated on top of this. Thus, the combination of BN and lead provides us with a sample that has well defined superconducting and non-superconducting regions as mentioned in Figure 8.3.

The Figure 8.6 shows the process involved in fabrication of the sample

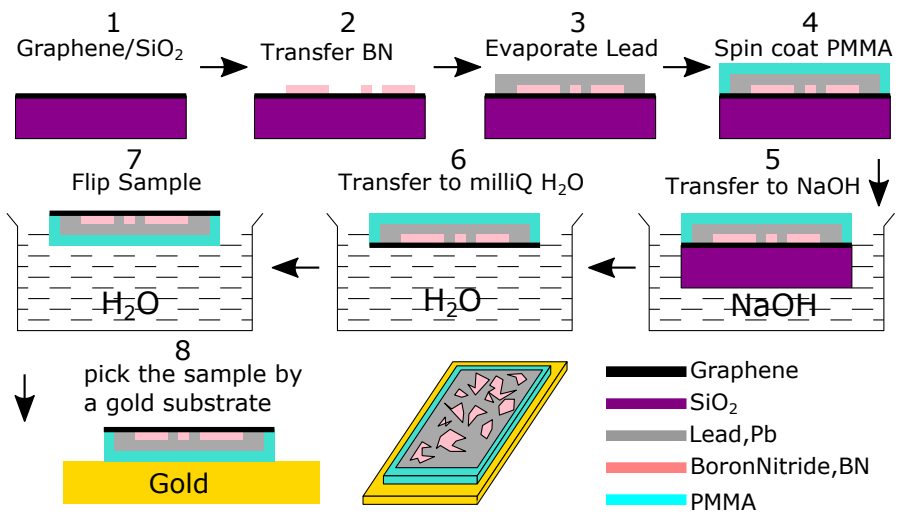


FIGURE 8.6: Scheme showing the device Fabrication of Graphene/BN/Pb samples

*Step 1 :* Graphene on $SiO_2$/Si (Doped Si wafers with a 300 nm thick layer) purchased from Graphena was used as the base substrate. 10 mm $\times$ 10 mm sized wafers were cut and cleaned by sonication in isopropanol for 5 minute.

*Step 2 :* The hexagonal boron nitride (h -BN) flakes are deposited on silicon dioxide substrate by mechanical exfoliation methods by using viscoelastic polydimethylsiloxane (PDMS) stamps.

*Step 3 :* Lead was deposited on this sample by thermal evaporation method. 300-500 nm thick lead was deposited on the sample. The base pressure of the evaporation chamber was kept around$5 \times 10^{-6}$ mbar.

*Step 4 :* Spin-coat the substrate with Polymethyl methacrylate (PMMA) for 1 min @ 5000 rpm. The sample was dried overnight.

*Step 5 :* Then the sample is partially dipped into a beaker of 1 molar aqueous solution of NaOH at $100^0$ C. This process will etch out the $SiO_2$.

*Step 6 :* After etching $SiO_2$, the sample is transferred to milliQ water at room temperature. The sample floats on the top of water due to the surface tension and hydrophobic nature of PMMA.

*Step 7 :* The sample is again transferred to the milliQ water. This time, the sample is flipped so that the graphene part lies on top.

*Step 8 :* The sample is slowly lifted from the water using gold on quartz. The Gold on Quartz was flammed annealed using butane flame and cooled to room temperature prior to this process.

The Figure 8.7a shows the optical image of after spin coating PMMA on top of lead deposited. The colour difference seen on top of the PMMA in Pb is due to the different thickness of PMMA. The Figure 8.7b shows the optical image substrate after the final process. One can directly observe the inverted pattern of the Pb region. The Figure 8.7c & d shows the zoom of the b 20X and 50X respectively. These images show BN flakes spread around the whole area. This large density of BN flakes on the surface makes it is easy to find a flake (non-superconducting region) while scanning with STM at low temperature.

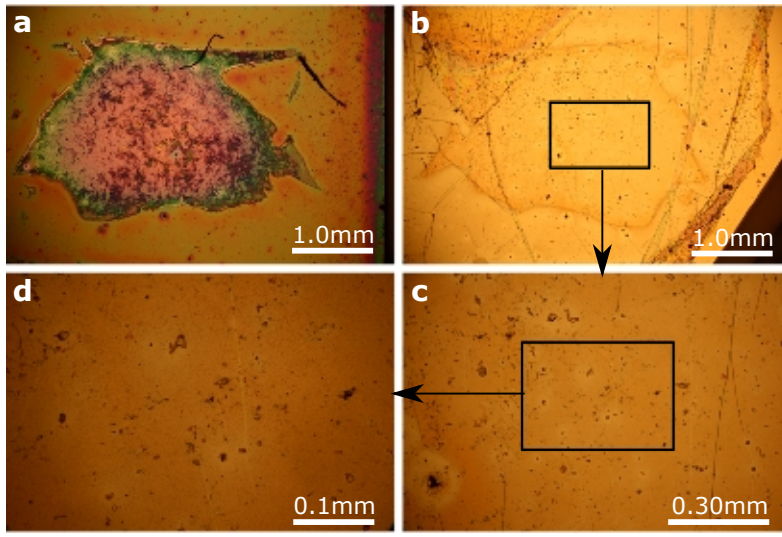


FIGURE 8.7: Optical Microscope image of various sample preparation stage (a) Image taken after step 4 i.e after spin coating PMMA (b) After step 8, transferring the sample to gold on quartz. (c) and (d) are zoom in of the image (b). The small dark spots appearing on the image (d) are BN flakes lying beneath the graphene.

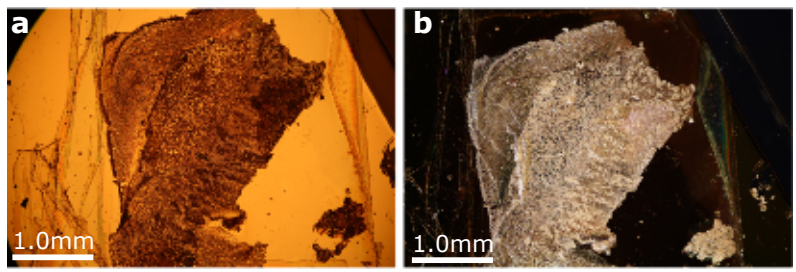


FIGURE 8.8: Optical Microscope image of another Graphene/BN/Pb sample. (a)Bright field image (b) dark field image

It was observed that in most of the samples are affected by the NaOH. NaOH solution is highly reactive and reacts with the Pb underneath the Graphene. This causes etching of Pb in many areas. The Figure 8.8a shows the optical image of a substrate etched by the NaOH. Figure 8.8b is the dark field image of the same area that clearly distinguishes between Pb (silver coloured) and etched areas (dark). Some area might have got oxidised as well. However,

some part of the sample is preserved, and we decided to cool down the sample for STM measurements.

## 8.3 STM and AFM Measurements

The sample was cooled down to cryogenic temperature and STM measurement were carried out. However, due to a leak in the inner vacuum chamber we could not achieve the base temperature of 350mK. Instead, measurement were performed at 4.2 K. Due to the leak; the helium bath was in good thermal contact with the STM, and this prevented us from conducting temperature dependent measurements

The substrate arrangement is similar to the to the set-up described in the Figure 8.3. Another Pb sample was kept side by side to the sample. This Pb sample was used to as reference sample to calibrate superconducting scanning tunnelling spectroscopy. Also, this sample was used to clean the superconducting tip by mechanical indentation.

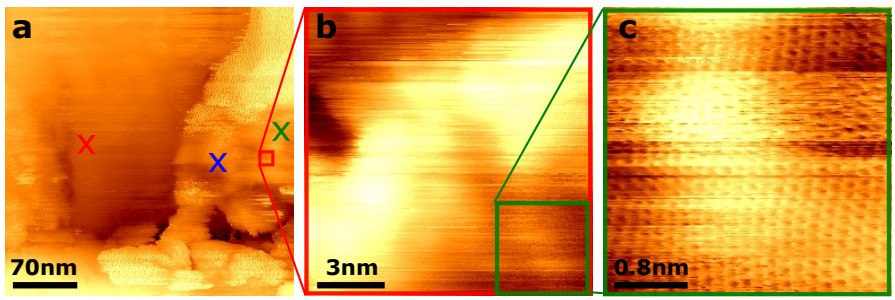


FIGURE 8.9: (a)STM image of Graphene on top of Lead region ($V_b$ = 50 mV, $I_t$ = 1.1 nA). (b) & (c) are zoom in of the region indicated by red and green square respectively

After cooling the sample, the tip is cleaned by repeated crash in the pure Pb till a stable STS of Pb-Pb gap was achieved. Then the tip is moved to Graphene sample using the horizontal piezo actuators. Figure 8.9 shows the STM image taken on the Graphene region. The Figure 8.9 b & c displays the

zoom in scans of the Figure 8.9a. The large areas STM image indicates that the surface follows the corrugation of $SiO_2$. The STS taken on different areas of the Figure 8.9 is shown in Figure 8.10. The STS shows an superconducting gap indicating that the Graphene is lying on top of Pb region.

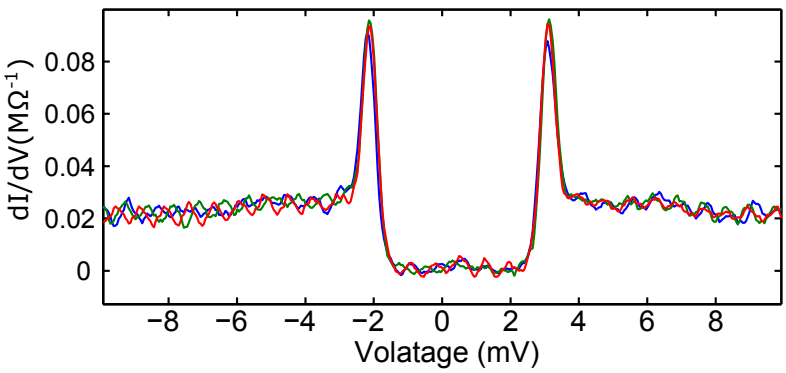


FIGURE 8.10: STS taken on Graphene on Pb at different area indicated by (x) mark on Figure 8.9.

The STS taken on Graphene on Pb region (blue coloured curve) is compared with the STS taken on bare Pb (black coloured line) in the Figure 8.11. In both region STS was taken at same conductance (0.02 $MOhm^{-1}$). The spectra taken on both region appears identical. The curves were fitted using the Bardeen-Cooper-Schrieffer (BCS) model [199]. The red curve in Figure 8.11 shows the BCS fit at the temperate 4.3 K and is in well agreement with the measured curves. The superconducting gaps obtained from the fit is $\Delta_{tip} = 1.30$ mV and $\Delta_{substarte} = 1.29$ mV. This shows that the gap observed on Graphene is almost same as the underlying metal. The width of the superconducting gap induced by proximity effect in Normal metal in contact depends on the interface barrier height between Normal - Super region. When the barrier height is negligibly small, i.e. A normal metal is in good contact with the superconductor; the induced gap will be same as that of the superconductor. This result is analogous to the recent experimental results observed in Graphene grown on Rhenium [187].

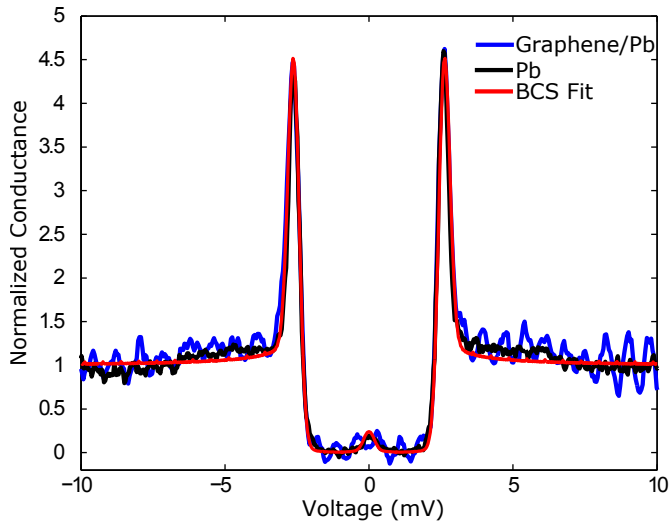


FIGURE 8.11: STS taken on (a)Pb (black colour), (b) Graphene on Pb (blue colour) & (c) BCS Fit (red colour) , $G_N = 0.02$ MOhm$^{-1}$.

In our case, the induced superconductivity was not observed in not all the regions. Only a few areas in the substrate were observed to show superconductivity. The absence superconducting regions could be due to the etching of Pb by NaOH. In some areas, reduced superconducting gap was also seen. This reduced gap could be either due to the small size Pb islands formed due to etching or oxidation of Pb during sample preparation. It is hard to determine the size effect and oxidation by STM technique alone. Next we tried the experiment is to observe the proximity in the Super-Normal region in the Boron- Nitride(BN) border. Hence, we searched for an area with graphene on top of BN flake. The optical image shows that the flakes are micron sized and spread around in a large area. The STM scan area is only few hundred nanometer at low temperature. Also, the movement of the slider is limited in on direction. These factors made finding BN flakes a hard task. The STM image of one such flake is shown below.

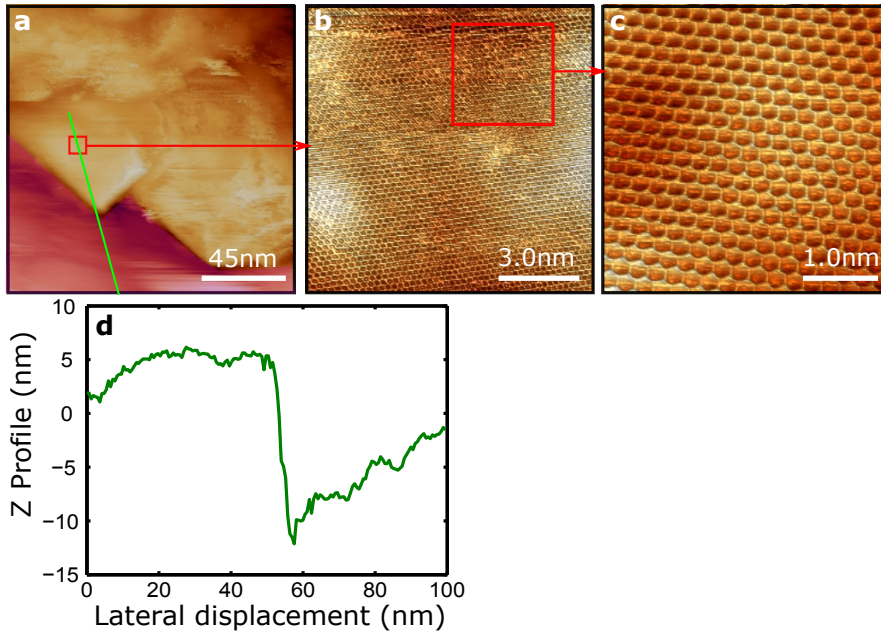


FIGURE 8.12: (a)STM scan of Graphene/BN area ($V_b = 0.3$ V, $I_t = 0.9$ nA). Area outside BN flake is coloured violet, (b) & (c) are the zoom in of the regions marked in red squares. (d) z profile along the green line shown in sub-figure (a).

The Figure 8.12a shows a border region with Graphene on top BN flake. The Graphene on non-BN part is highlighted in the figure. The high-resolution scans of the area in (a) are shown in b & c. The Figure 8.12c shows the honeycomb lattice of Graphene. The STS taken on the region showed that the Graphene on top of the BN flake is not superconducting. More over no superconducting part is observed outside the flake as well. The profile take on flake shows that the flake boundaries are not flat, and they are very steep. This indicates that the Pb near the flake is removed during the sample preparation. Most of the flakes observed showed abrupt boundary near BN edge.

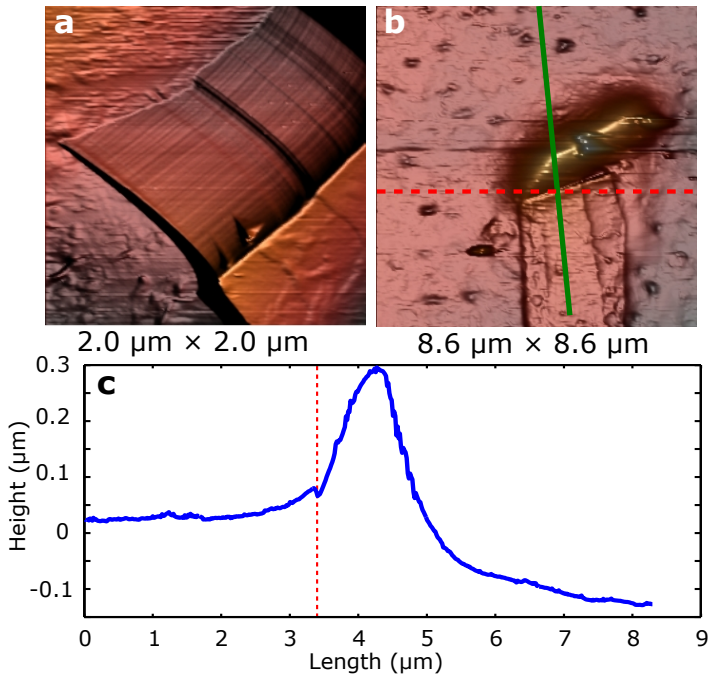


FIGURE 8.13: (a)AFM image of a Graphene on top of BN flake (b) AFM of another flake (c) height profile along the green line drawn on (b). The red line indicated the boundary between the flake and the island.

To further verify the substrate, we measured the sample using AFM after warming up the system. The AFM images on two different flakes are shown in Figure 8.13 a & b. In both the pictures, the Graphene on BN is visible, and the flakes have well-defined sharp edges. These edges are supposed to flat and covered with the Pb. However, the AFM shows that the Pb is absent. In the Figure 8.13 b, a small hilly region is observed near the flake. This hill-like structure could be the Pb remaining after the etching. The AFM height profile taken over the island shows that the flake is slanting over the island. This indicates that the flake was lying on to Pb and most of the Pb beneath it got etched out during the NaOH processing. Hence, the BN flake slanted over the remaining part of Pb.

Even though the optical image shows that some areas with Pb are conserved, close examination with the AFM shows that the Pb near most of the BN flakes

is removed. This could be due the holes and scratches is in Graphene sheet. NaOH, which is a strong reactant, enter through these holes in graphene and react with Pb. However, in some regions Pb is well preserved. STM image shown in the section 8.9 corresponds to one of such region. In those regions, Graphene is well attached to the Pb and shows superconductivity as demonstrated by the STS. This shows that graphene can be made superconducting by proximity effect. However to characterise the coherence length and other properties is difficult.

## 8.4 Conclusion and future work

Here we show a method to obtain superconductivity by inducing proximity effect. STM and STS investigation show that Graphene in close contact to a superconductor, lead, displays superconducting gap features. BCS fit analysis shows that the superconducting gap measured on graphene on top of Pb is same as that of the bulk Pb showing that the Graphene becomes a BCS superconductor. We did not succeed in measuring the lateral proximity effect due ot the difficulties in sample preparation. However, the results indicate that the graphene of Pb turns superconductor and hence these materials can serve as the substrate for depositing functional molecules. This also extends the possibility of deposition at ambient sample preparation conditions. However, we need to develop further a method avoiding strong reactants such as NaOH to avoid the etching of superconducting materials.

# Part V

# General Conclusions

# Chapter 9

# General Conclusions

In this thesis, we investigated the rectification effect and magnetism of single molecules. The main results of this thesis are

- A compact Low-Temperature Scanning Tunnelling Microscope (LT-STM) operating at 350mK with a long range sample stage was constructed. A heater and thermal sensors were attached to the sample holder. The superconducting magnet and temperature measurements setup was automated.

- A deposition technique was developed for depositing molecule on substrates. A stable deposition of single molecules onto a substrate is a prerequisite for STM studies. This is a challenging task, especially when dealing with molecules that cannot be deposited by thermal evaporation. In our case, the molecule DyW30 is a water-soluble molecule that restricted us from adopting many wet deposition methods as well. The spray deposition method developed enable us to deposit single molecules on Au(111) surface in a controlled way at ambient conditions. The STM and XPS results demonstrate that molecules stay intact after deposition. The samples prepared by wet deposition methods has a higher possibility

of contamination. A clean cooling down procedure was also developed to ensure the cleanliness of samples for low-temperature measurements.

- We investigated the rectification of a polyoxometalate molecule in single molecule junctions. We obtained large rectification ratios ( $> 100$) for a DyW30; that is one of the highest experimentally recorded values. The molecule also sustains high current densities ($> 10^5$ A/cm$^2$). In contrast with previously reported molecular rectifiers, we could show unambiguously that the rectification in these molecules is due to the asymmetric coupling of the electrodes with the molecular level. This was measured by conducting controlled IZ- IV measurements on individual molecules and interpreted using a single level model. The model was further verified by conducting the experiment on $C_{60}$ molecule. These results give insight into the mechanism of rectification, the oldest problem in molecular electronic.

- We also investigated the magnetic properties of the molecule by conducting spin IETS at low temperature. The results show that the DyW30 molecule preserves magnetic behaviours on deposition on a metal surface. The inelastic spin jump values obtained were modelled using simple single ion in crystal field model and we could infer the change associated with a spin of a single molecule compared to the bulk. The emergence of Kondo effect on pressing the molecule with tip shows that the electrode coupling affects the magnetism of the molecule.

- We also investigated the possibility of developing superconducting Graphene substrates for depositing single molecule magnets. We deposited Graphene on top of Pb, and could confirm that Graphene becomes a proximity-induced superconductor in contact with lead by using scanning tunnelling spectroscopy.

To conclude, we investigated rectification and magnetism in single molecule junctions using a Scanning Tunnelling Microscope operating at ambient and low temperature. The results show experimental observation of both the

process in a polyoxometalate-based molecule. These findings combined with the theoretical analysis throw light on the origin of rectification and magnetism in single molecule junctions. The proximity-induced superconductivity in Graphene was also investigated.

# Chapter 10

# Conclusiones Generales

En esta tesis, hemos investigado el efecto de rectificación y el magnetismo de moléculas individuales. Los principales resultados de esta tesis son:

- Se ha construido un Microscopio de Efecto Túnel de Bajas Temperaturas (LT-STM) que opera a 350 mK y que tiene una plataforma para la muestra con un gran rango de movimiento. Se han añadido un calentador y sensores térmicos al soporte de la muestra y se han automatizado el imán superconductor y las medidas de temperatura.

- Se ha desarrollado una técnica de deposición de moléculas en sustratos. La deposición estable de moléculas individuales sobre un sustrato es un requisito para estudios con STM. Éste es un reto importante, especialmente cuando se trata de moléculas que no se pueden depositar mediante evaporación térmica. En nuestro caso, la molécula DyW30 es una molécula soluble en agua, lo que nos limitó también el uso de muchos métodos de deposición desde disolución. El método de deposición con espray desarrollado nos permite depositar moléculas individuales sobre una superficie de Au(111) de una forma controlada en condiciones ambiente. Los resultados de STM y XPS demuestran que las moléculas permanecen intactas después de la deposición. Las muestras preparadas con

métodos de deposición desde disolución tienen una probabilidad mayor de contaminación. También se ha desarrollado un procedimiento de refrigeración limpio para asegurar la limpieza de las muestras para las medidas a baja temperatura.

- Investigamos la rectificación de un polioxometalato en uniones moleculares individuales. Obtuvimos grandes ratios de rectificación ($> 100$) para el DyW30, uno de los valores más elevados medidos experimentalmente hasta el momento. La molécula soporta también altas densidades de corriente ($> 10^5 \mathrm{A/cm}^2$). Al contrario que otros rectificadores moleculares publicados previamente, pudimos mostrar inequívocamente que la rectificación de estas moléculas es debida al acoplamiento asimétrico de los electrodos con el nivel molecular. Ésto fue medido realizando IZ-IV controladas en moléculas individuales y se interpretó utilizando un modelo de un único nivel. El modelo, además, fue verificado realizando el experimento en moléculas de $C_{60}$. Estos resultados ofrecen una mejor comprensión del mecanismo de rectificación, el problema más antiguo de la electrónica molecular.

- También investigamos las propiedades magnéticas de la molécula mediante espectroscopía inelástica de espín (spin IETS) a bajas temperaturas. Los resultados muestran que la molécula DyW30 conserva comportamientos magnéticos al depositarla sobre una superficie metálica. Los valores del salto inelástico de espín obtenidos fueron modelizados utilizando un modelo sencillo de un ión en presencia de un campo cristalino y pudimos deducir la carga asociada al espín de una única molécula comparada con el valor de volumen. La aparición de efecto Kondo al presionar la molécula con la punta muestra que el acoplamiento con el electrodo afecta al magnetismo de la molécula.

- Además, investigamos la posibilidad de desarrollar sustratos de grafeno superconductor para depositar imanes moleculares individuales. Depositamos grafeno sobre Pb y pudimos confirmar que el grafeno se vuelve

superconductor por proximidad en contacto con el plomo, utilizando para ello espectroscopía de efecto túnel.

En conclusión, hemos investigado rectificación y magnetismo en uniones moleculares individuales utilizando un Microscopio de Efecto Túnel que opera a temperatura ambiente y a bajas temperaturas. Los resultados demuestran la observación experimental de ambos procesos en una molécula de polioxometalato. Estos hallazgos combinados con análisis teóricos ofrcen una mejor comprensión del origen de la rectificación y el magnetismo de uniones moleculares individuales. También se ha investigado la superconductividad inducida por proximidad en grafeno.

# Publications

- **Siya Sherif**, G. Rubio-Bollinger, E. Pinilla-Cienfuegos, E. Coronado, and N. Agraït. Magnetism of Lanthanide based Single Molecule Magnet deposited on Au(111) ( in preparation)
- **Siya Sherif**, L Terracciano, Y Duan, E Leary, M. Teresa Gonzalez, R Otero, G Rubio-Bollinger, E Coronado and N Agraït. An easy and reliable spray method to deposit isolated polyoxometalate molecules on surfaces: Application to lanthanide-based single-molecule magnets. (Submitted to Langmuir)
- **Siya Sherif**, G. Rubio-Bollinger, E. Pinilla-Cienfuegos, E. Coronado, J. C. Cuevas and N. Agrait. Current rectification in a single molecule diode: the role of electrode coupling. Nanotechnology 26 (2015) 291001 (highlighted in LabTalk, IoP)

**Previous to this thesis**

- Swati Pandya, **Siya Sherif**, L.S. Sharath Chandra and V. Ganesan: "Magneto-transport studies of $FeSe_{0.9-x}Mx$(M = Si, Sb)", Supercond. Sci. Technol. 24 (2011) 045011
- Swati Pandya, L. S. Chandra, **Siya Sherif**, and V. Ganesan. "2D Lowest Landau Level Scaling in $FeTe_{0.5}Se_{0.5}$." American Insti. of Phy. Conf. Series, 1349 (2011) 885.

- Swati Pandya, **Siya Sherif**, LS Sharath Chandra, and V. Ganesan. "Resistive broadening in sulfur doped FeTe." Supercond. Sci. Technol 23, no. 7 (2010): 075015.

# Appendix A

# AppendixA Piezo Calibration

The piezo electric tube (PZT) used in the STM needs to be calibrated before carrying out the experiments. We calibrate the piezo tube by imaging a known surface. We calibrate the Z with the monotonic steps of Au(111).

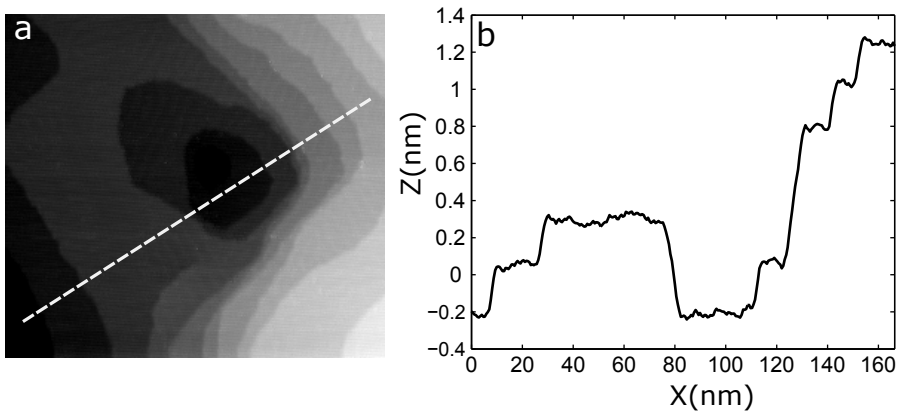


FIGURE A.1: (a) STM image of a Au(111). The planes are separated by mono-atomic steps taken at room temperature (b) Line profile taken alone dotted white line on image (a)

The mono-atomic steps of the Au(111) are separated by 0.24 nm. The Figure A.1 shows the STM image of Au(111) surface and a line profile taken along the surface using smaller tube. Many such line profiles were taken and averaged

to obtain mean value for piezo constant $K_z$. The value is $K_z = 3.7$ nm/V at room temperature. The displacement ($\Delta z$) of PZT for an applied voltage, $V_z$ ,can be estimated using the formula [200]

$$\Delta z = \frac{d_{31} V_z l}{t} \tag{A.1}$$

where $l$ is the length, $t$ is the wall thickness and $d_{31}$is the piezoelectric coefficient of the piezoelectric tube. For the PZT used for making STM, $l$ = 11.0mm, $t$ = 0.55 mm and $d_{31} = 1.73 \times 10^{-10}$ m/V.Hence we get a $K_z = 3.46 nm/V$ which is close to the experimentally observed value. However, this value will change at low temperature. Figure A.2 shows that STM image taken at 350 mK. We obtain a $K_z = 0.56$ nm/V at 350 mK.

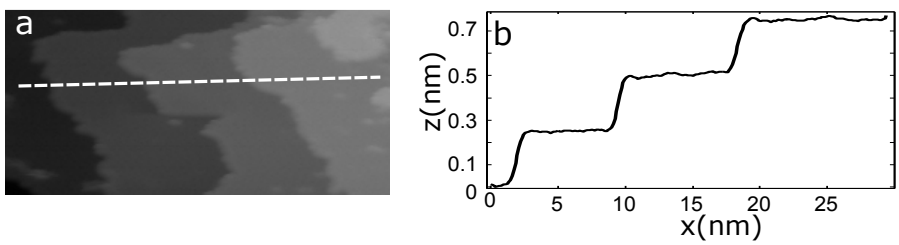


FIGURE A.2: (a) STM image of a Au(111). The planes are separated by mono-atomic steps taken at 350mK (b) Line profile taken alone dotted white line on image (a)

The deflection of PZT in x, and y on applying voltage $V_{x,y}$ in opposite quadrant (see fig 1.5) can be estimated using the equation [200].

$$\Delta x, y = \frac{2\sqrt{2} d_{31} V_{x,y} l^2}{\pi D t} \tag{A.2}$$

where, D is the inner diameter of the tube. Thus the value obtained for $K_{x,y} = 3.64$ nm/V. Graphene on Copper foil was images at low temperature to calibrate x,y piezo constants (see figureA.3). The spacing of the hexagonal lattice of carbon is 0.246 nm [178] . This can be used to calibrate the value of piezo constant for x,y and we obtain $K_{x,y} = 0.95$ nm/V.

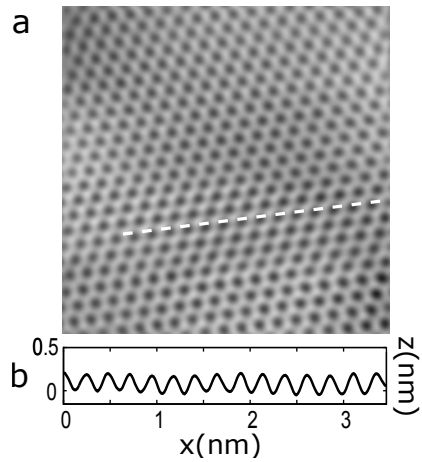


FIGURE A.3: (a) STM image of Graphene on Copper foil taken at 350mK (b) Line profile taken alone dotted white line on image (a)

# Appendix B

# Appendix B STM Tip Preparation

One of the main component determining the quality of the STM/STS is the tip. Hence, preparation of stable STM tip is a perquisite for performing STM investigation [193, 201]. We used two types of materials for tip gold (Au) and lead (Pb) for making tip. Au was prepared from mechanically cutting a 0.25 mm wire. Meanwhile, Pb tip was prepares from metallic pieces. The Pb pieces were sharpened mechanically. The tips thus prepare were soldered to the STM tip holder. This process is carried out just before closing the vacuum chamber to reduce the contamination. However, some contamination may occur due to the exposure of air. In order to obtain a clean tip at low temperature we follow the mechanical annealing process [193, 194].

The sample holder of the STM contain two samples. One of the sample will be the same material use as tip (Au or Pb). The sample stage moved to position the tip on top of this material. Then we perform several indentation cycles with STM tip on this sample. The Conductance - displacement (G-z) is also recorded during this process. One such curve taken in the case of Au tip showed in the Figure B.1. Conductance versus distance curves shows

well defined steps at $G_0 = 2e^2/h$ for Au. This figure also shows atomic re-engagements during this process. The conductance at the breaking step is at $G_0$ and indicates that only a single atom is present in the apex if tip. Since most of the tunnelling process occur through the last atom, the apex atom determine the quality of STM and STS. This process is repeated when ever tip is contaminated.

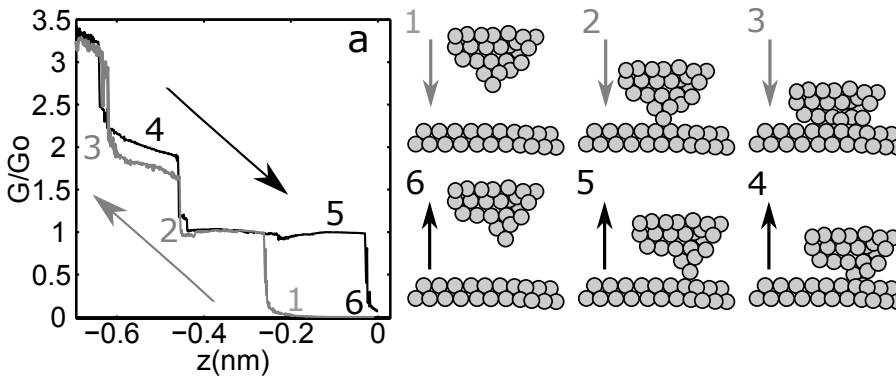


FIGURE B.1: Image on left shows the conductance - tip displacement when approaching (grey) and retracting (black) the few-atom point contact regime. Possible atomic arrangements are shown schematically at the right of the figure.

# Bibliography


[1] Gordon E Moore et al. Progress in digital integrated electronics. *IEDM Tech. Digest*, 11, 1975.

[2] Juan Carlos Cuevas and Elke Scheer. *Molecular electronics: an introduction to theory and experiment*, volume 1. World Scientific, 2010.

[3] Arieh Aviram and Mark A Ratner. Molecular rectifiers. *Chemical Physics Letters*, 29(2):277–283, 1974.

[4] S Cardona-Serra, JM Clemente-Juan, E Coronado, A Gaita-Ariño, A Camón, M Evangelisti, F Luis, MJ Martínez-Pérez, and J Sesé. Lanthanoid single-ion magnets based on polyoxometalates with a 5-fold symmetry: The series [lnp5w30o110] 12–(ln3+= tb, dy, ho, er, tm, and yb). *Journal of the American Chemical Society*, 134(36):14982–14990, 2012.

[5] Andrei Mourachkine. *Room-temperature superconductivity*. Cambridge Int Science Publishing, 2004.

[6] N Moussy, H Courtois, and B Pannetier. Local spectroscopy of a proximity superconductor at very low temperature. *EPL (Europhysics Letters)*, 55(6):861, 2001.

[7] V Cherkez, JC Cuevas, C Brun, T Cren, G Ménard, F Debontridder, VS Stolyarov, and D Roditchev. Proximity effect between two superconductors spatially resolved by scanning tunneling spectroscopy. *Physical Review X*, 4(1):011033, 2014.

[8] Jean-Noël Fuchs and Mark Oliver GOERBIG. Introduction to the physical properties of graphene. *Lecture Notes*, 2008.

[9] John MD Coey. *Magnetism and magnetic materials*. Cambridge University Press, 2010.

[10] José J Baldoví, Salvador Cardona-Serra, Juan M Clemente-Juan, Eugenio Coronado, Alejandro Gaita-Ariño, and Andrew Palii. Simpre: A software package to calculate crystal field parameters, energy levels, and magnetic properties on mononuclear lanthanoid complexes based on charge distributions. *Journal of computational chemistry*, 34(22): 1961–1967, 2013.

[11] Gerd Binnig and Heinrich Rohrer. Scanning tunneling microscopy—from birth to adolescence. *Reviews of Modern Physics*, 59(3):615–625, 1987.

[12] Gerd Binnig, Heinrich Rohrer, Ch Gerber, and Eddie Weibel. Tunneling through a controllable vacuum gap. *Applied Physics Letters*, 40(2):178–180, 1982.

[13] Gerd Binnig, Heinrich Rohrer, Ch Gerber, and E Weibel. Surface studies by scanning tunneling microscopy. *Physical review letters*, 49(1):57, 1982.

[14] Herbert B Michaelson. The work function of the elements and its periodicity. *Journal of Applied Physics*, 48(11):4729–4733, 1977.

[15] Roland Wiesendanger. *Scanning probe microscopy and spectroscopy: methods and applications*. Cambridge University Press, 1994.

[16] J. Bardeen. Tunnelling from a many-particle point of view. *Phys. Rev. Lett.*, 6:57–59, Jan 1961. doi: 10.1103/PhysRevLett.6.57. URL http://link.aps.org/doi/10.1103/PhysRevLett.6.57.

[17] J Tersoff and DR Hamann. Theory and application for the scanning tunneling microscope. *Physical review letters*, 50(25):1998, 1983.

[18] J Tersoff and DR Hamann. Theory of the scanning tunneling microscope. In *Scanning Tunneling Microscopy*, pages 59–67. Springer, 1993.

[19] John Lambe and RC Jaklevic. Molecular vibration spectra by inelastic electron tunneling. *Physical Review*, 165(3):821, 1968.

[20] Nicolás Agraït, Carlos Untiedt, Gabino Rubio-Bollinger, and Sebastián Vieira. Onset of energy dissipation in ballistic atomic wires. *Physical review letters*, 88(21):216803, 2002.

[21] Carlos R. Arroyo, Thomas Frederiksen, Gabino Rubio-Bollinger, Marisela Vélez, Andrés Arnau, Daniel Sánchez-Portal, and Nicolás Agra¨. Characterization of single-molecule pentanedithiol junctions by inelastic electron tunneling spectroscopy and first-principles calculations. *Phys. Rev. B*, 81:075405, Feb 2010. doi: 10.1103/PhysRevB.81.075405. URL http://link.aps.org/doi/10.1103/PhysRevB.81.075405.

[22] Mark A Reed. Inelastic electron tunneling spectroscopy. *Materials today*, 11(11):46–50, 2008.

[23] SH Pan, EW Hudson, and JC Davis. 3he refrigerator based very low temperature scanning tunneling microscope. *Review of scientific instruments*, 70(2):1459–1463, 1999.

[24] C. Arroyo. *Electron transport and phonons in atomic wires and single molecule junctions*. PhD thesis, 2010.

[25] Jacques Curie and Pierre Curie. Development by pressure of polar electricity in hemihedral crystals with inclined faces. *Bull. soc. min. de France*, 3:90, 1880.

[26] Ch Joachim, JK Gimzewski, and A Aviram. Electronics using hybrid-molecular and mono-molecular devices. *Nature*, 408(6812):541–548, 2000.

[27] Mark Ratner. A brief history of molecular electronics. *Nature nanotechnology*, 8(6):378–381, 2013.

[28] Lapo Bogani and Wolfgang Wernsdorfer. Molecular spintronics using single-molecule magnets. *Nature materials*, 7(3):179–186, 2008.

[29] Guillem Aromí and Richard EP Winpenny. *Single-molecule magnets and related phenomena*. Springer New York, 2006.

[30] Moon-Ho Jo, Jacob E Grose, Kanhayalal Baheti, Mandar M Deshmukh, Jennifer J Sokol, Evan M Rumberger, David N Hendrickson, Jeffrey R Long, Hongkun Park, and DC Ralph. Signatures of molecular magnetism in single-molecule transport spectroscopy. *Nano letters*, 6(9):2014–2020, 2006.

[31] E Burzurí, AS Zyazin, A Cornia, and HSJ Van der Zant. Direct observation of magnetic anisotropy in an individual fe 4 single-molecule magnet. *Physical review letters*, 109(14):147203, 2012.

[32] Andrea Cornia and Matteo Mannini. *Single-molecule magnets on surfaces*. Springer, 2014.

[33] Steffen Kahle, Zhitao Deng, Nikola Malinowski, Charlene Tonnoir, Alicia Forment Aliaga, Nicha Thontasen, Gordon Rinke, Duy Le, Volodymyr Turkowski, and Talat S Rahman. The quantum magnetism of individual manganese-12-acetate molecular magnets anchored at surfaces. *Nano letters*, 12(1):518–521, 2011.

[34] Dimitris E Katsoulis. A survey of applications of polyoxometalates. *Chemical Reviews*, 98(1):359–388, 1998.

[35] Murad A AlDamen, Juan M Clemente-Juan, Eugenio Coronado, Carlos Martí-Gastaldo, and Alejandro Gaita-Arino. Mononuclear lanthanide single-molecule magnets based on polyoxometalates. *Journal of the American Chemical Society*, 130(28):8874–8875, 2008.

[36] Ludovica Margheriti, Matteo Mannini, Lorenzo Sorace, Lapo Gorini, Dante Gatteschi, Andrea Caneschi, Daniele Chiappe, Riccardo Moroni, Francesco Buatier de Mongeot, Andrea Cornia, et al. Thermal deposition of intact tetrairon (iii) single-molecule magnets in high-vacuum conditions. *Small*, 5(12):1460–1466, 2009.

[37] Stephan Rauschenbach. Electrospray ion beam deposition and mass spectrometry of nonvolatile molecules and nanomaterials. 2008.

[38] Lucia Vitali, Stefano Fabris, Adriano Mosca Conte, Susan Brink, Mario Ruben, Stefano Baroni, and Klaus Kern. Electronic structure of surface-supported bis (phthalocyaninato) terbium (iii) single molecular magnets. *Nano letters*, 8(10):3364–3368, 2008.

[39] Jordi Gómez-Segura, Ismael Díez-Pérez, Naoto Ishikawa, Motohiro Nakano, Jaume Veciana, and Daniel Ruiz-Molina. 2-d self-assembly of the bis (phthalocyaninato) terbium (iii) single-molecule magnet studied by scanning tunnelling microscopy. *Chemical communications*, (27): 2866–2868, 2006.

[40] M Clemente-León, E Coronado, A Soriano-Portillo, Christophe Mingotaud, and JM Dominguez-Vera. Langmuir–blodgett films based on inorganic molecular complexes with magnetic or optical properties. *Advances in colloid and interface science*, 116(1):193–203, 2005.

[41] Dante Gatteschi, Andrea Cornia, Matteo Mannini, and Roberta Sessoli. Organizing and addressing magnetic molecules. *Inorganic chemistry*, 48 (8):3408–3419, 2009.

[42] Neus Domingo, E Bellido, and Daniel Ruiz-Molina. Advances on structuring, integration and magnetic characterization of molecular nanomagnets on surfaces and devices. *Chemical Society Reviews*, 41(1):258–302, 2012.

[43] Gonzalo Otero, Emi Evangelio, Celia Rogero, Luis Vazquez, Jordi Gomez Segura, Jose Angel Martin Gago, and Daniel Ruiz Molina. Morphological investigation of mn12 single-molecule magnets adsorbed on au (111). *Langmuir*, 25(17):10107–10115, 2009.

[44] Jordi Gómez-Segura, Olga Kazakova, Julia Davies, Patrick Josephs-Franks, Jaume Veciana, and Daniel Ruiz-Molina. Self-organization of mn12 single-molecule magnets into ring structures induced by breath-figures as templates. *Chem. Commun.*, (45):5615–5617, 2005.

[45] Eugenio Coronado, Alicia Forment-Aliaga, Francisco M Romero, Valdis Corradini, Roberto Biagi, Valentina De Renzi, Alessandro Gambardella, and Umberto del Pennino. Isolated mn12 single-molecule magnets grafted on gold surfaces via electrostatic interactions. *Inorganic chemistry*, 44(22):7693–7695, 2005.

[46] Inge Creaser, Mark C Heckel, R Jeffrey Neitz, and Michael T Pope. Rigid nonlabile polyoxometalate cryptates [zp5w30o110](15-n)-that exhibit unprecedented selectivity for certain lanthanide and other multivalent cations. *Inorganic Chemistry*, 32(9):1573–1578, 1993.

[47] J Červenka and CFJ Flipse. Fullerene monolayer formation by spray coating. *Nanotechnology*, 21(6):065302, 2010.

[48] A Nemati Kharat, Mansour Abedini, M Mohammadpour Amini, Phillip Pendleton, and Alexander Badalyan. Investigation of the preyssler phosphotungstate heteropolyanion,[nap5w30o110] 14-, properties with different counter ions. *Transition Metal Chemistry*, 28(3):339–344, 2003.

[49] C Day. Basics and applications of cryopumps. 2007.

[50] FD Natterer, F Patthey, and H Brune. Quantifying residual hydrogen adsorption in low-temperature stms. *Surface Science*, 615:80–87, 2013.

[51] S. Dushman and A. H. Young. Calibration of ionization gauge for different gases. *Phys. Rev.*, 68:278–278, Dec 1945. doi: 10.1103/PhysRev.68.278.2. URL http://link.aps.org/doi/10.1103/PhysRev.68.278.2.

[52] J.A. Fleming. Instrument for converting alternating electric currents into continuous currents, 1905. URL http://www.google.com/patents/US803684.

[53] Lee De Forest. Oscillation-responsive device., 1906.

[54] KARL Ferdinand Braun. Electrical oscillations and wireless telegraphy. *Nobel Lecture, December*, 11(1909):226–245, 1909.

[55] Probir K Bondyopadhyay. Sir jc bose diode detector received marconi's first transatlantic wireless signal of december 1901 (the "italian navy coherer" scandal revisited). *Proceedings of the IEEE*, 86(1):259–285, 1998.

[56] Tapan K Sarkar, Robert Mailloux, Arthur A Oliner, Magdalena Salazar-Palma, and Dipak L Sengupta. *History of wireless*, volume 177. John Wiley & Sons, 2006.

[57] Lars Grondahl and Paul H Geiger. A new electronic rectifier. *American Institute of Electrical Engineers, Transactions of the*, 46:357–366, 1927.

[58] MD Fagen, Amos E Joel, S Millman, and GE Schindler. *A History of Engineering and Science in the Bell System: Physical Sciences (1925-1980)*, volume 4. The Laboratories, 1983.

[59] J. Bardeen and W. H. Brattain. Physical principles involved in transistor action. *Phys. Rev.*, 75:1208–1225, Apr 1949. doi: 10.1103/PhysRev.75.1208. URL http://link.aps.org/doi/10.1103/PhysRev.75.1208.

[60] William Shockley. The theory of p-n junctions in semiconductors and p-n junction transistors. *Bell System Technical Journal*, 28(3):435–489, 1949.

[61] R Lloyd Carroll and Christopher B Gorman. The genesis of molecular electronics. *Angewandte Chemie International Edition*, 41(23):4378–4400, 2002.

[62] Mark Bohr and Kaizad Mistry. Intel's revolutionary 22 nm transistor technology. *Intel Corporation*, 1, 2011.

[63] Lanlan Sun, Yuri A Diaz-Fernandez, Tina A Gschneidtner, Fredrik Westerlund, Samuel Lara-Avila, and Kasper Moth-Poulsen. Single-molecule electronics: from chemical design to functional devices. *Chemical Society Reviews*, 43(21):7378–7411, 2014.

[64] Wei Lu and Charles M Lieber. Nanoelectronics from the bottom up. *Nature materials*, 6(11):841–850, 2007.

[65] Lidia Łukasiak and Andrzej Jakubowski. History of semiconductors. *Journal of Telecommunications and information technology*, pages 3–9, 2010.

[66] Ben G Streetman and Sanjay Banerjee. *Solid state electronic devices*, volume 4. Prentice Hall New Jersey, 2000.

[67] Richard P Feynman. There's plenty of room at the bottom. *Engineering and science*, 23(5):22–36, 1960.

[68] Robert M Metzger, Bo Chen, Ulf Höpfner, MV Lakshmikantham, Dominique Vuillaume, Tsuyoshi Kawai, Xiangli Wu, Hiroaki Tachibana, Terry V Hughes, Hiromi Sakurai, et al. Unimolecular electrical rectification in hexadecylquinolinium tricyanoquinodimethanide. *Journal of the American Chemical Society*, 119(43):10455–10466, 1997.

[69] PE Kornilovitch, AM Bratkovsky, and R Stanley Williams. Current rectification by molecules with asymmetric tunneling barriers. *Physical Review B*, 66(16):165436, 2002.

[70] Takeshi Mikayama, Masato Ara, Kaku Uehara, Akira Sugimoto, Kazuhiko Mizuno, and Naohisa Inoue. Nanometre-scale photoelectric characteristics of a molecular device monolayer. *Physical Chemistry Chemical Physics*, 3(16):3459–3462, 2001.

[71] Man-Kit Ng, Dong-Chan Lee, and Luping Yu. Molecular diodes based on conjugated diblock co-oligomers. *Journal of the American Chemical Society*, 124(40):11862–11863, 2002.

[72] Ping Jiang, Gustavo M Morales, Wei You, and Luping Yu. Synthesis of diode molecules and their sequential assembly to control electron transport. *Angewandte Chemie*, 116(34):4571–4575, 2004.

[73] J. G. Kushmerick, D. B. Holt, J. C. Yang, J. Naciri, M. H. Moore, and R. Shashidhar. Metal-molecule contacts and charge transport across monomolecular layers: Measurement and theory. *Phys. Rev. Lett.*, 89: 086802, Aug 2002. doi: 10.1103/PhysRevLett.89.086802. URL http://link.aps.org/doi/10.1103/PhysRevLett.89.086802.

[74] Mark Elbing, Rolf Ochs, Max Koentopp, Matthias Fischer, Carsten von Hänisch, Florian Weigend, Ferdinand Evers, Heiko B Weber, and Marcel Mayor. A single-molecule diode. *Proceedings of the National Academy of Sciences of the United States of America*, 102(25):8815–8820, 2005.

[75] Ismael Díez-Pérez, Joshua Hihath, Youngu Lee, Luping Yu, Lyudmyla Adamska, Mortko A Kozhushner, Ivan I Oleynik, and Nongjian Tao. Rectification and stability of a single molecular diode with controlled orientation. *Nature chemistry*, 1(8):635–641, 2009.

[76] Christian A Nijhuis, William F Reus, and George M Whitesides. Molecular rectification in metal- sam- metal oxide- metal junctions. *Journal of the American Chemical Society*, 131(49):17814–17827, 2009.

[77] Christian A Nijhuis, William F Reus, Jabulani R Barber, Michael D Dickey, and George M Whitesides. Charge transport and rectification in arrays of sam-based tunneling junctions. *Nano letters*, 10(9):3611–3619, 2010.

[78] Arunabh Batra, Pierre Darancet, Qishui Chen, Jeffrey S Meisner, Jonathan R Widawsky, Jeffrey B Neaton, Colin Nuckolls, and Latha

Venkataraman. Tuning rectification in single-molecular diodes. *Nano letters*, 13(12):6233–6237, 2013.

[79] Jason C Randel, Francis C Niestemski, Andrés R Botello-Mendez, Warren Mar, Georges Ndabashimiye, Sorin Melinte, Jeremy EP Dahl, Robert MK Carlson, Ekaterina D Butova, Andrey A Fokin, et al. Unconventional molecule-resolved current rectification in diamondoid–fullerene hybrids. *Nature communications*, 5, 2014.

[80] Michael T Pope and Achim Müller. Polyoxometalate chemistry: an old field with new dimensions in several disciplines. *Angewandte Chemie International Edition in English*, 30(1):34–48, 1991.

[81] B Larade and AM Bratkovsky. Current rectification by simple molecular quantum dots: An ab initio study. *Physical Review B*, 68(23):235305, 2003.

[82] Siya Sherif, Gabino Rubio-Bollinger, Elena Pinilla-Cienfuegos, Eugenio Coronado, Juan Carlos Cuevas, and Nicolás Agraït. Current rectification in a single molecule diode: the role of electrode coupling. *Nanotechnology*, 26(29):291001, 2015. URL http://stacks.iop.org/0957-4484/26/i=29/a=291001.

[83] Saw-Wai Hla. Scanning tunneling microscopy single atom/molecule manipulation and its application to nanoscience and technology. *Journal of Vacuum Science & Technology B*, 23(4):1351–1360, 2005.

[84] Charalambos Evangeli, Katalin Gillemot, Edmund Leary, M Teresa Gonzalez, Gabino Rubio-Bollinger, Colin J Lambert, and Nicolas Agrait. Engineering the thermopower of c60 molecular junctions. *Nano letters*, 13(5):2141–2145, 2013.

[85] Jorge A Fernández, Xavier López, Carles Bo, Coen de Graaf, Evert J Baerends, and Josep M Poblet. Polyoxometalates with internal cavities: Redox activity, basicity, and cation encapsulation in [x n+ p5w30o110](15-n)-preyssler complexes, with x= na+, ca2+, y3+, la3+,

ce3+, and th4+. *Journal of the American Chemical Society*, 129(40): 12244–12253, 2007.

[86] Jin Zhao, Changgan Zeng, Xin Cheng, Kedong Wang, Guanwu Wang, Jinlong Yang, J. G. Hou, and Qingshi Zhu. Single $c_{59}N$ molecule as a molecular rectifier. *Phys. Rev. Lett.*, 95:045502, Jul 2005. doi: 10.1103/PhysRevLett.95.045502. URL http://link.aps.org/doi/10.1103/PhysRevLett.95.045502.

[87] Yu-qing Yang. Magnetic materials in china. In *Proceedings of the 3rd International Conference on Physics of Magnetic Materials, Szczyrk-Biła (Poland), September 9-14, 1986*, page 4. World Scientific Publishing Company Incorporated, 1987.

[88] Daniel C Mattis. *Theory of Magnetism Made Simple*. World, 2004.

[89] William Gilbert. *De magnete*. Courier Corporation, 1958.

[90] J J Thomson. Carriers of negative electricity. *Les prix Nobel*, 1906.

[91] George E Uhlenbeck and Samuel Goudsmit. Spinning electrons and the structure of spectra. *Nature*, 117:264–265, 1926.

[92] James M Tour. Molecular electronics. synthesis and testing of components. *Accounts of Chemical Research*, 33(11):791–804, 2000.

[93] SA Wolf, DD Awschalom, RA Buhrman, JM Daughton, S Von Molnar, ML Roukes, A Yu Chtchelkanova, and DM Treger. Spintronics: a spin-based electronics vision for the future. *Science*, 294(5546):1488–1495, 2001.

[94] ShangDa Jiang, Karin Goß, Christian Cervetti, and Lapo Bogani. An introduction to molecular spintronics. *Science China Chemistry*, 55(6): 867–882, 2012.

[95] Louis Néel. Théorie du traînage magnétique des substances massives dans le domaine de rayleigh. *J. phys. radium*, 11(2):49–61, 1950.

[96] Dante Gatteschi, Roberta Sessoli, and Jacques Villain. *Molecular nanomagnets*. Oxford University Press, 2006.

[97] Roberta Sessoli, Dante Gatteschi, Andrea Caneschi, and MA Novak. Magnetic bistability in a metal-ion cluster. 1993.

[98] Roberta Sessoli, Hui Lien Tsai, Ann R Schake, Sheyi Wang, John B Vincent, Kirsten Folting, Dante Gatteschi, George Christou, and David N Hendrickson. High-spin molecules:[mn12o12 (o2cr) 16 (h2o) 4]. *Journal of the American Chemical Society*, 115(5):1804–1816, 1993.

[99] George Christou, Dante Gatteschi, David N Hendrickson, and Roberta Sessoli. Single-molecule magnets. *Mrs Bulletin*, 25(11):66–71, 2000.

[100] Eufemio Moreno Pineda. *New f-Block and Mixed d,f-Block Molecular Nanomagnets*. PhD thesis, 2014.

[101] Jonathan R Friedman, MP Sarachik, J Tejada, and R Ziolo. Macroscopic measurement of resonant magnetization tunneling in high-spin molecules. *Physical review letters*, 76(20):3830, 1996.

[102] Naoto Ishikawa, Miki Sugita, Tadahiko Ishikawa, Shin-ya Koshihara, and Youkoh Kaizu. Lanthanide double-decker complexes functioning as magnets at the single-molecular level. *Journal of the American Chemical Society*, 125(29):8694–8695, 2003.

[103] Jean-Claude G Bünzli and Svetlana V Eliseeva. Basics of lanthanide photophysics. In *Lanthanide Luminescence*, pages 1–45. Springer, 2011.

[104] Heiko Lueken. Course of lectures on magnetism of lanthanide ions under varying ligand and magnetic fields. *Institute of Inorganic Chemistry, RWTH Aachen*, 3, 2008.

[105] Jeffrey D Rinehart and Jeffrey R Long. Exploiting single-ion anisotropy in the design of f-element single-molecule magnets. *Chemical Science*, 2 (11):2078–2085, 2011.

[106] Humphrey LC Feltham and Sally Brooker. Review of purely 4f and mixed-metal nd-4f single-molecule magnets containing only one lanthanide ion. *Coordination Chemistry Reviews*, 276:1–33, 2014.

[107] Jonathan R Friedman and Myriam P Sarachik. Single-molecule nanomagnets. *arXiv preprint arXiv:1001.4194*, 2010.

[108] Gavin A Craig and Mark Murrie. 3d single-ion magnets. *Chemical Society Reviews*, 2015.

[109] Song Gao. Molecular nanomagnets and related phenomena, 2015.

[110] AJ Heinrich, JA Gupta, CP Lutz, and DM Eigler. Single-atom spin-flip spectroscopy. *Science*, 306(5695):466–469, 2004.

[111] Charles D Ruggiero, Taeyoung Choi, and Jay A Gupta. Tunneling spectroscopy of ultrathin insulating films: Cun on cu (100). *Applied Physics Letters*, 91(25):253106, 2007.

[112] Cyrus F Hirjibehedin, Christopher P Lutz, and Andreas J Heinrich. Spin coupling in engineered atomic structures. *Science*, 312(5776):1021–1024, 2006.

[113] AF Otte, M Ternes, S Loth, CP Lutz, CF Hirjibehedin, and AJ Heinrich. Spin excitations of a kondo-screened atom coupled to a second magnetic atom. *Physical review letters*, 103(10):107203, 2009.

[114] T Balashov, T Schuh, AF Takács, A Ernst, S Ostanin, J Henk, I Mertig, P Bruno, T Miyamachi, S Suga, et al. Magnetic anisotropy and magnetization dynamics of individual atoms and clusters of fe and co on pt (111). *Physical review letters*, 102(25):257203, 2009.

[115] Alexander Ako Khajetoorians, Samir Lounis, Bruno Chilian, Antonio T Costa, Lihui Zhou, Douglas L Mills, Jens Wiebe, and Roland Wiesendanger. Itinerant nature of atom-magnetization excitation by tunneling electrons. *Physical review letters*, 106(3):037205, 2011.

[116] Leo Kouwenhoven and Leonid Glazman. Revival of the kondo effect. *Physics world*, 14(1):33–38, 2001.

[117] WJ De Haas, J De Boer, and GJ Van den Berg. The electrical resistance of gold, copper and lead at low temperatures. *Physica*, 1(7):1115–1124, 1934.

[118] Alexander Cyril Hewson. *The Kondo problem to heavy fermions*. Number 2. Cambridge university press, 1997.

[119] Jun Kondo. Resistance minimum in dilute magnetic alloys. *Progress of theoretical physics*, 32(1):37–49, 1964.

[120] Kenneth G Wilson. The renormalization group: Critical phenomena and the kondo problem. *Reviews of Modern Physics*, 47(4):773, 1975.

[121] Stephen Gregory. Experimental observation of scattering of tunneling electrons by a single magnetic moment. *Physical review letters*, 68(13): 2070, 1992.

[122] David Goldhaber-Gordon, Hadas Shtrikman, D Mahalu, David Abusch-Magder, U Meirav, and MA Kastner. Kondo effect in a single-electron transistor. *Nature*, 391(6663):156–159, 1998.

[123] V Madhavan, W Chen, T Jamneala, MF Crommie, and NS Wingreen. Tunneling into a single magnetic atom: spectroscopic evidence of the kondo resonance. *Science*, 280(5363):567–569, 1998.

[124] Jiutao Li, Wolf-Dieter Schneider, Richard Berndt, and Bernard Delley. Kondo scattering observed at a single magnetic impurity. *Physical Review Letters*, 80(13):2893, 1998.

[125] Gavin David Scott and Douglas Natelson. Kondo resonances in molecular devices. *Acs Nano*, 4(7):3560–3579, 2010.

[126] Michael Pustilnik and Leonid Glazman. Kondo effect in quantum dots. *Journal of Physics: Condensed Matter*, 16(16):R513, 2004.

[127] Michael Pustilnik, Yshai Avishai, and Konstantin Kikoin. Quantum dots with even number of electrons: Kondo effect in a finite magnetic field. *Physical review letters*, 84(8):1756, 2000.

[128] F Delgado, Cyrus F Hirjibehedin, and Joaquín Fernández-Rossier. Consequences of kondo exchange on quantum spins. *Surface Science*, 630: 337–342, 2014.

[129] Jean-Pierre Gauyacq, Nicolás Lorente, and Frederico Dutilh Novaes. Excitation of local magnetic moments by tunneling electrons. *Progress in Surface Science*, 87(5):63–107, 2012.

[130] Markus Ternes, Andreas J Heinrich, and Wolf-Dieter Schneider. Spectroscopic manifestations of the kondo effect on single adatoms. *Journal of Physics: Condensed Matter*, 21(5):053001, 2009.

[131] M Reyes Calvo, David Jacob, and Carlos Untiedt. Analysis of the kondo effect in ferromagnetic atomic-sized contacts. *Physical Review B*, 86(7): 075447, 2012.

[132] Jiwoong Park, Abhay N Pasupathy, Jonas I Goldsmith, Connie Chang, Yuval Yaish, Jason R Petta, Marie Rinkoski, James P Sethna, Héctor D Abruña, Paul L McEuen, et al. Coulomb blockade and the kondo effect in single-atom transistors. *Nature*, 417(6890):722–725, 2002.

[133] Aidi Zhao, Qunxiang Li, Lan Chen, Hongjun Xiang, Weihua Wang, Shuan Pan, Bing Wang, Xudong Xiao, Jinlong Yang, JG Hou, et al. Controlling the kondo effect of an adsorbed magnetic ion through its chemical bonding. *Science*, 309(5740):1542–1544, 2005.

[134] Tadahiro Komeda, Hironari Isshiki, Jie Liu, Yan-Feng Zhang, Nicolás Lorente, Keiichi Katoh, Brian K Breedlove, and Masahiro Yamashita. Observation and electric current control of a local spin in a single-molecule magnet. *Nature communications*, 2:217, 2011.

[135] C Romeike, MR Wegewijs, W Hofstetter, and H Schoeller. Quantum-tunneling-induced kondo effect in single molecular magnets. *Physical review letters*, 96(19):196601, 2006.

[136] C Romeike, MR Wegewijs, W Hofstetter, and H Schoeller. Kondo-transport spectroscopy of single molecule magnets. *Physical review letters*, 97(20):206601, 2006.

[137] Michael N Leuenberger and Eduardo R Mucciolo. Berry-phase oscillations of the kondo effect in single-molecule magnets. *Physical review letters*, 97(12):126601, 2006.

[138] Igor Žutić, Jaroslav Fabian, and S Das Sarma. Spintronics: Fundamentals and applications. *Reviews of modern physics*, 76(2):323, 2004.

[139] Wolfgang Wernsdorfer. Molecular nanomagnets: towards molecular spintronics. *International Journal of Nanotechnology*, 7(4-8):497–522, 2010.

[140] Matteo Mannini, Philippe Sainctavit, Roberta Sessoli, Christophe Cartier dit Moulin, Francesco Pineider, Marie-Anne Arrio, Andrea Cornia, and Dante Gatteschi. Xas and xmcd investigation of mn12 monolayers on gold. *Chemistry-A European Journal*, 14(25):7530–7535, 2008.

[141] Hongkun Park, Andrew KL Lim, A Paul Alivisatos, Jiwoong Park, and Paul L McEuen. Fabrication of metallic electrodes with nanometer separation by electromigration. *Applied Physics Letters*, 75(2):301–303, 1999.

[142] Christian A Martin, Dapeng Ding, Herre SJ van der Zant, and Jan M van Ruitenbeek. Lithographic mechanical break junctions for single-molecule measurements in vacuum: possibilities and limitations. *New Journal of Physics*, 10(6):065008, 2008.

[143] Alexander S Zyazin, Johan WG van den Berg, Edgar A Osorio, Herre SJ van der Zant, Nikolaos P Konstantinidis, Martin Leijnse, Maarten R Wegewijs, Falk May, Walter Hofstetter, Chiara Danieli, et al. Electric

field controlled magnetic anisotropy in a single molecule. *Nano letters*, 10(9):3307–3311, 2010.

[144] Ferry Prins, Amelia Barreiro, Justus W Ruitenberg, Johannes S Seldenthuis, Núria Aliaga-Alcalde, Lieven MK Vandersypen, and Herre SJ van der Zant. Room-temperature gating of molecular junctions using few-layer graphene nanogap electrodes. *Nano letters*, 11(11):4607–4611, 2011.

[145] Matias Urdampilleta, Svetlana Klyatskaya, Jean-Pierre Cleuziou, Mario Ruben, and Wolfgang Wernsdorfer. Supramolecular spin valves. *Nature materials*, 10(7):502–506, 2011.

[146] Matias Urdampilleta, Svetlana Klyatskaya, Mario Ruben, and Wolfgang Wernsdorfer. Magnetic interaction between a radical spin and a single-molecule magnet in a molecular spin-valve. *ACS nano*, 2015.

[147] Marc Ganzhorn, Svetlana Klyatskaya, Mario Ruben, and Wolfgang Wernsdorfer. Carbon nanotube nanoelectromechanical systems as magnetometers for single-molecule magnets. *ACS nano*, 7(7):6225–6236, 2013.

[148] Marc Ganzhorn, Svetlana Klyatskaya, Mario Ruben, and Wolfgang Wernsdorfer. Strong spin-phonon coupling between a single-molecule magnet and a carbon nanotube nanoelectromechanical system. *Nature nanotechnology*, 8(3):165–169, 2013.

[149] Andrea Candini, Svetlana Klyatskaya, Mario Ruben, Wolfgang Wernsdorfer, and Marco Affronte. Graphene spintronic devices with molecular nanomagnets. *Nano letters*, 11(7):2634–2639, 2011.

[150] E Burzurí, R Gaudenzi, and HSJ van der Zant. Observing magnetic anisotropy in electronic transport through individual single-molecule magnets. *Journal of Physics: Condensed Matter*, 27(11):113202, 2015.

[151] Michael Pope et al. *Polyoxometalates: From Platonic Solids to Anti-Retroviral Activity: From Platonic Solids to Anti-Retroviral Activity*, volume 10. Springer Science & Business Media, 1994.

[152] Naoto Ishikawa, Miki Sugita, Tadahiko Ishikawa, Shin-ya Koshihara, and Youkoh Kaizu. Mononuclear lanthanide complexes with a long magnetization relaxation time at high temperatures: A new category of magnets at the single-molecular level. *The Journal of Physical Chemistry B*, 108 (31):11265–11271, 2004.

[153] Naoto Ishikawa, Miki Sugita, Tomoko Okubo, Naohiro Tanaka, Tomochika Iino, and Youkoh Kaizu. Determination of ligand-field parameters and f-electronic structures of double-decker bis (phthalocyaninato) lanthanide complexes. *Inorganic chemistry*, 42(7):2440–2446, 2003.

[154] Stefan Stoll and Arthur Schweiger. Easyspin, a comprehensive software package for spectral simulation and analysis in epr. *Journal of Magnetic Resonance*, 178(1):42–55, 2006.

[155] Stefan Stoll and R David Britt. General and efficient simulation of pulse epr spectra. *Physical Chemistry Chemical Physics*, 11(31):6614–6625, 2009.

[156] KW Hipps and Ursula Mazur. Inelastic electron tunneling: an alternative molecular spectroscopy. *The Journal of Physical Chemistry*, 97(30): 7803–7814, 1993.

[157] O Újsághy, J Kroha, L Szunyogh, and A Zawadowski. Theory of the fano resonance in the stm tunneling density of states due to a single kondo impurity. *Physical review letters*, 85(12):2557, 2000.

[158] BenWarner. Engineering the properties of magnetic molecules through the interaction with the surface.

[159] Jenny C Oberg, M Reyes Calvo, Fernando Delgado, María Moro-Lagares, David Serrate, David Jacob, Joaquín Fernández-Rossier, and

Cyrus F Hirjibehedin. Control of single-spin magnetic anisotropy by exchange coupling. *Nature nanotechnology*, 9(1):64–68, 2014.

[160] H Kamerlingh Onnes. The resistance of pure mercury at helium temperatures. *Commun. Phys. Lab. Univ. Leiden*, 12(120):1, 1911.

[161] HEIKE Kamerlingh Onnes. Investigations into the properties of substances at low temperatures, which have led, amongst other things, to the preparation of liquid helium. *Nobel lecture*, 306, 1913.

[162] Dirk Van Delft and Peter Kes. The discovery of superconductivity. *Physics Today*, 63(9):38–43, 2010.

[163] Walther Meissner and Robert Ochsenfeld. Ein neuer effekt bei eintritt der supraleitfähigkeit. *Naturwissenschaften*, 21(44):787–788, 1933.

[164] C Jo Gorter and HBG Casimir. The thermodynamics of the superconducting state. *Z. tech. phys*, 15:539–42, 1934.

[165] Fritz London and Heinz London. The electromagnetic equations of the supraconductor. In *Proceedings of the Royal Society of London A: Mathematical, Physical and Engineering Sciences*, volume 149, pages 71–88. The Royal Society, 1935.

[166] L Shubnikov and I Nakhutin. Electrical conductivity of a superconducting sphere in the intermediate state. *Nature*, 139:589–590, 1937.

[167] Lev Davidovich Landau and VL Ginzburg. On the theory of superconductivity. *Zh. Eksp. Teor. Fiz.*, 20:1064, 1950.

[168] Herbert Fröhlich. Theory of the superconducting state. i. the ground state at the absolute zero of temperature. *Physical Review*, 79(5):845, 1950.

[169] Leon N Cooper. Bound electron pairs in a degenerate fermi gas. *Physical Review*, 104(4):1189, 1956.

[170] Charles K Poole, Horacio A Farach, and Richard J Creswick. *Handbook of superconductivity*. Academic Press, 1999.

[171] Stig Lundqvist. *Physics 1971-1980*, volume 5. World scientific, 1992.

[172] J George Bednorz and K Alex Müller. Possible hight c superconductivity in the ba- la- cu- o system. *Zeitschrift für Physik B Condensed Matter*, 64(2):189–193, 1986.

[173] Yoichi Kamihara, Takumi Watanabe, Masahiro Hirano, and Hideo Hosono. Iron-based layered superconductor la [o1-x f x] feas (x= 0.05-0.12) with t c= 26 k. *Journal of the American Chemical Society*, 130 (11):3296–3297, 2008.

[174] AF Andreev. Thermal conductivity of the intermediate state of superconductors. *Zh. Eksperim. i Teor. Fiz.*, 46, 1964.

[175] H Courtois, P Charlat, Ph Gandit, D Mailly, and B Pannetier. The spectral conductance of a proximity superconductor and the reentrance effect. *Journal of low temperature physics*, 116(3-4):187–213, 1999.

[176] Jungdae Kim, Victor Chua, Gregory A Fiete, Hyoungdo Nam, Allan H MacDonald, and Chih-Kang Shih. Visualization of geometric influences on proximity effects in heterogeneous superconductor thin films. *Nature Physics*, 8(6):464–469, 2012.

[177] L Serrier-Garcia, JC Cuevas, T Cren, C Brun, V Cherkez, F Debontridder, D Fokin, FS Bergeret, and D Roditchev. Scanning tunneling spectroscopy study of the proximity effect in a disordered two-dimensional metal. *Physical review letters*, 110(15):157003, 2013.

[178] Andre K Geim and Konstantin S Novoselov. The rise of graphene. *Nature materials*, 6(3):183–191, 2007.

[179] Y Hancock. The 2010 nobel prize in physics—ground-breaking experiments on graphene. *Journal of Physics D: Applied Physics*, 44(47): 473001, 2011.

[180] Sheneve Z Butler, Shawna M Hollen, Linyou Cao, Yi Cui, Jay A Gupta, Humberto R Gutierrez, Tony F Heinz, Seung Sae Hong, Jiaxing Huang, Ariel F Ismach, et al. Progress, challenges, and opportunities in two-dimensional materials beyond graphene. *ACS nano*, 7(4):2898–2926, 2013.

[181] Philip Richard Wallace. The band theory of graphite. *Physical Review*, 71(9):622, 1947.

[182] KSA Novoselov, Andre K Geim, SVb Morozov, Da Jiang, MIc Katsnelson, IVa Grigorieva, SVb Dubonos, and AAb Firsov. Two-dimensional gas of massless dirac fermions in graphene. *nature*, 438(7065):197–200, 2005.

[183] N. B. Hannay, T. H. Geballe, B. T. Matthias, K. Andres, P. Schmidt, and D. MacNair. Superconductivity in graphitic compounds. *Phys. Rev. Lett.*, 14:225–226, Feb 1965. doi: 10.1103/PhysRevLett.14.225. URL http://link.aps.org/doi/10.1103/PhysRevLett.14.225.

[184] Z-H Pan, J Camacho, MH Upton, AV Fedorov, CA Howard, M Ellerby, and T Valla. Electronic structure of superconducting kc 8 and non-superconducting lic 6 graphite intercalation compounds: evidence for a graphene-sheet-driven superconducting state. *Physical review letters*, 106(18):187002, 2011.

[185] T Valla, J Camacho, Z-H Pan, AV Fedorov, AC Walters, CA Howard, and M Ellerby. Anisotropic electron-phonon coupling and dynamical nesting on the graphene sheets in superconducting cac 6 using angle-resolved photoemission spectroscopy. *Physical review letters*, 102(10): 107007, 2009.

[186] Hubert B Heersche, Pablo Jarillo-Herrero, Jeroen B Oostinga, Lieven MK Vandersypen, and Alberto F Morpurgo. Bipolar supercurrent in graphene. *Nature*, 446(7131):56–59, 2007.

[187] Charlène Tonnoir, Amina Kimouche, Johann Coraux, Laurence Magaud, Benjamin Delsol, Bruno Gilles, and Claude Chapelier. Induced superconductivity in graphene grown on rhenium. *Physical review letters*, 111 (24):246805, 2013.

[188] Xu Du, Ivan Skachko, and Eva Y Andrei. Josephson current and multiple andreev reflections in graphene sns junctions. *Physical Review B*, 77(18): 184507, 2008.

[189] Dmitri K Efetov. *Towards inducing superconductivity into graphene*. PhD thesis, COLUMBIA UNIVERSITY, 2014.

[190] Jacob Linder and Jason WA Robinson. Superconducting spintronics. *Nature Physics*, 11(4):307–315, 2015.

[191] CWJ Beenakker. Specular andreev reflection in graphene. *Physical review letters*, 97(6):067007, 2006.

[192] Stefan Schmaus, Alexei Bagrets, Yasmine Nahas, Toyo K Yamada, Annika Bork, Martin Bowen, Eric Beaurepaire, Ferdinand Evers, and Wulf Wulfhekel. Giant magnetoresistance through a single molecule. *Nature nanotechnology*, 6(3):185–189, 2011.

[193] Andres Castellanos-Gomez, Gabino Rubio-Bollinger, Manuela Garnica, Sara Barja, Amadeo L Vázquez de Parga, Rodolfo Miranda, and Nicolás Agraït. Highly reproducible low temperature scanning tunneling microscopy and spectroscopy with in situ prepared tips. *Ultramicroscopy*, 122:1–5, 2012.

[194] JG Rodrigo, H Suderow, and S Vieira. On the use of stm superconducting tips at very low temperatures. *The European Physical Journal B-Condensed Matter and Complex Systems*, 40(4):483–488.

[195] Sangita Bose, Pratap Raychaudhuri, Rajarshi Banerjee, Parinda Vasa, and Pushan Ayyub. Mechanism of the size dependence of the superconducting transition of nanostructured nb. *Physical review letters*, 95(14): 147003, 2005.

[196] Sangita Bose, Antonio M García-García, Miguel M Ugeda, Juan D Urbina, Christian H Michaelis, Ivan Brihuega, and Klaus Kern. Observation of shell effects in superconducting nanoparticles of sn. *Nature materials*, 9(7):550–554, 2010.

[197] Neil W Ashcroft and N David Mermin. Solid state phys. *Saunders, Philadelphia*, page 293, 1976.

[198] CR Dean, AF Young, I Meric, C Lee, L Wang, S Sorgenfrei, K Watanabe, T Taniguchi, P Kim, KL Shepard, et al. Boron nitride substrates for high-quality graphene electronics. *Nature nanotechnology*, 5(10):722–726, 2010.

[199] RC Dynes, V Narayanamurti, and J Pm Garno. Direct measurement of quasiparticle-lifetime broadening in a strong-coupled superconductor. *Physical Review Letters*, 41(21):1509, 1978.

[200] C Julian Chen. Electromechanical deflections of piezoelectric tubes with quartered electrodes. *Applied Physics Letters*, 60(1):132–134, 1992.

[201] Stefan Ernst. Optimisation of the preparation process for tips used in scanning tunneling microscopy. *Technische Universitat Dresden*, 2006.